POLITECNICO DI TORINO

Master of Science in Energy and Nuclear Engineering

Master Thesis

Modelica dynamic modelling of a supercritical CO_2 loop for solar and nuclear applications

In collaboration with Universitat Politècnica de Catalunya, Barcelona

Supervisors
Prof. Laura Savoldi (PoliTo)
Prof. Lluis Batet Miracle (UPC)

Candidate
Simone Ferrero

Academic Year 2019/2020

Acknowledgments

I would like to thank firstly my family and my friends for all the emotional, technical and economical support that I have constantly received from them, not only in the past months abroad, but during all my university years; they've always been on my side in every choice I have taken and without them many things would haven't been possible.

Right after, I would like to thank Prof. Savoldi for accepting to be my supervisor and to have guided me in this thesis work. I have always admired her as person and teacher, she has always supported and given me all the help I needed. Her knowledge, decision and insights were some of the main driving forces in my work. It was an honour working with her and I honestly hope there will be occasion for future collaborations.

Similar thoughts go to Prof. Batet, whom I would like to thank for his constant presence and availability in these five months at UPC. From the first day he always followed my work, giving the necessary suggestions and never making me feel alone. It was a pleasure to have the opportunity to work with him and all the staff of the UPC nuclear department, I sincerely hope to keep in contact with them and work together again.

Finally, I would like to warmly thank Dr. Bonifetto and Dr. Froio for all their patience and help they provided me in these months, for guiding me from afar, always finding time to dedicate me. Without them I honestly doubt I would have been able to reach the same conclusions.

Abstract

Supercritical CO2 power cycles have gained growing interest in the last years, thanks to the particular properties of the carbon dioxide when kept above its critical point, i.e., intermediate between the ones of fluids and those of gases. Thanks to this, sCO2 Brayton loops lead to relevant improvements with respect to the well-known Rankine steam cycles, both in terms of efficiency and size. Their possible applications are numerous, such as concentrated solar power, nuclear secondary circuits, waste-to-energy, and high temperature fuel cells. The interest of this thesis is more centred on the first application. The present work, developed in collaboration with Universitat Politècnica de Catalunya (Barcelona, Spain), focuses on the dynamic modelling of a regenerative sCO2 Brayton cycle using the Modelica language, well known in the field of modelling of complex physical systems, involving, for instance, mechanical, electronics, hydraulic and thermal aspects, with controls. The specific sCO2 cycle, adopted as reference, was designed by a team at the Comillas Pontificial University (Madrid, Spain), using the Engineering Equation Solver, within the framework of the EUROfusion Programme (Euratom Horizon 2020). Two Modelica models have been developed in this thesis, and benchmarked against the reference cycle, to have a proof of reliability of the results: the layout of the first model is simply identical to the reference loop; the second one is a more realistic version, including pipes, manifolds and collectors in addition to the turbo-machines and heat exchangers. Three PI controllers were introduced in the second model, to perform dynamic simulations aimed at the development of suitable controls. Finally, two possible strategies of part-load operation have been developed and tested, simulating a 20% decrease of plant operation. The first based on the control of molten salt mass flow rate and, consequently, turbine inlet temperature, while the second regulates the aperture of a valve, in order to add an additional pressure drop and to modulate the CO_2 mass flow in the loop. According to the results obtained in both cases, the most convenient part-load operation strategy will be suggested.

Contents

1 Introduction

Since the pre-industrial period, the Earth has undergone important climate changes, mainly witnessed by global warming, carrying with it serious environmental consequences such as changes in the precipitations and consequently more frequent periods of drought, bushfires and poles melting. The global average temperature has been rising constantly in the last 50 years, peaking 1.1 °C in 2019 (Figure 1).

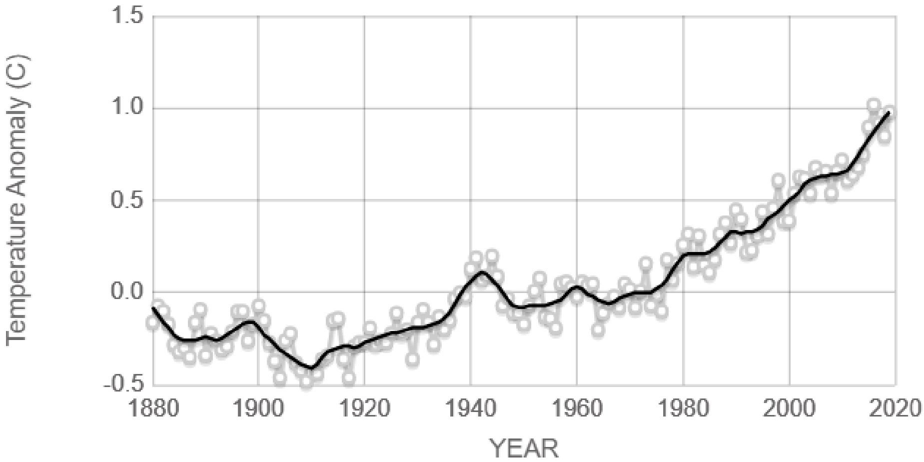

Figure 1 Global surface temperature anomaly referred to average values of 1951-1980 (NASA Climate, 2019)

The emission of greenhouse gases, such as carbon dioxide and nitrous oxide, has been one of the main human contributions to the intensification of the problem, which has been under evaluated for a long time (Stocker et al., 2013). Luckily, in the last years the common awareness has been increasing, leading to many actions, both popular and political. In particular, a huge step has been taken in this direction in 2015 during the COP21 with the Paris Agreement. Signing it, the countries with the highest emissions decided to establish a universal framework, in order to act united to compensate for the effects of global warming. The Paris Agreement was of crucial importance because it was the first legal global action against climate changes, formally recognizing their existence and threats connected to it. The agreement aims to limit the global temperature increase well below 2°C, setting the limit to 1.5°C, with respect to the pre industrial values, to avoid catastrophic consequences (European Commission, 2015).

Although, recently, in December 2019, the global action against climate changes have slowed down: during the COP25 held in Madrid, the parties could not find an agreement on article 6 of the "Katowice rulebook", regarding the international carbon market. This event shows that, even though numerous steps have been taken in the past decades, the environmental protection is not the priority yet and a bigger effort will be required to compensate for global warming before reaching the point of no return.

Moreover, the actual scenarios forecast an increment in the world population over 10 billion by 2100, connected with a corresponding increase of energy demand, especially in the developing countries where it will be almost doubled by 2050 (Figure 2), also due to the growing standard of lives (U.S. Energy Information Administration, 2019).

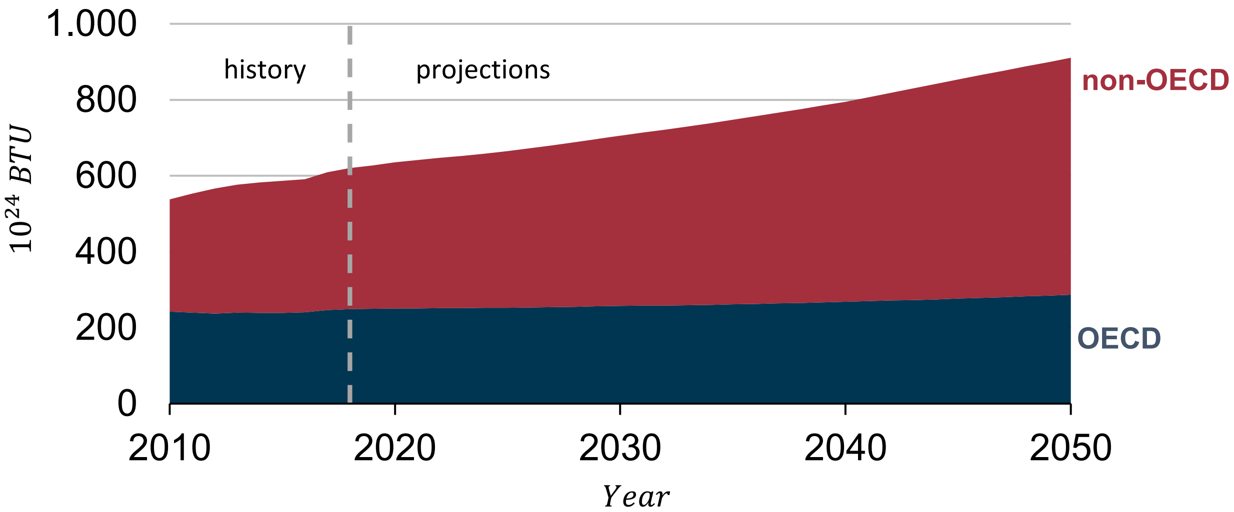

Figure 2 Energy demand forecast in quadrillion BTU (EIA, 2019)

Undoubtedly, it is not feasible to expect limiting fossil fuels and CO_2 emissions, while covering the raising energy demand with fossil fuels. The goals imposed by the Paris Agreement are ambitious, especially in a context of development as the one expected, therefore it is necessary that all the efforts to limit use of fossil fuels should be made. It will be requested to both pay more attention each one of our daily lifestyles, and to reduce the carbon emissions of the energy sector, introducing increased renewables' share in the energy production. To respect the targets, CO2 emissions derived from electricity production should be reduced almost to zero by 2050 (IAEA, 2019). Fossil fuels technologies generate around 150 and 1100 g CO2/kWh produced, while renewables emit between 1 and 170 g CO2 every kWh (Benjamín Monge Brenes, 2014). In recent years, the share of renewables has considerably increased, but these still have an enormous potential of expansion and together with nuclear, both fission and fusion, will play a vital role in the future decades to contain the greenhouse gases emissions and promote the energy transition (TheWorldBank, 2019).

Initially, the bottleneck of the renewables' diffusion was their immature technology, leading to prohibitive costs, but in the last two decades, their development helped considerably in decreasing the costs and enhancing their diffusion. Solar technologies took the lead in this trend, with the most consistent drop of LCOE and installation costs (IRENA 2019); this can be seen from Figure 3, which shows the average LCOE evolution of different renewable technologies at utility scale from 2010 to 2018.

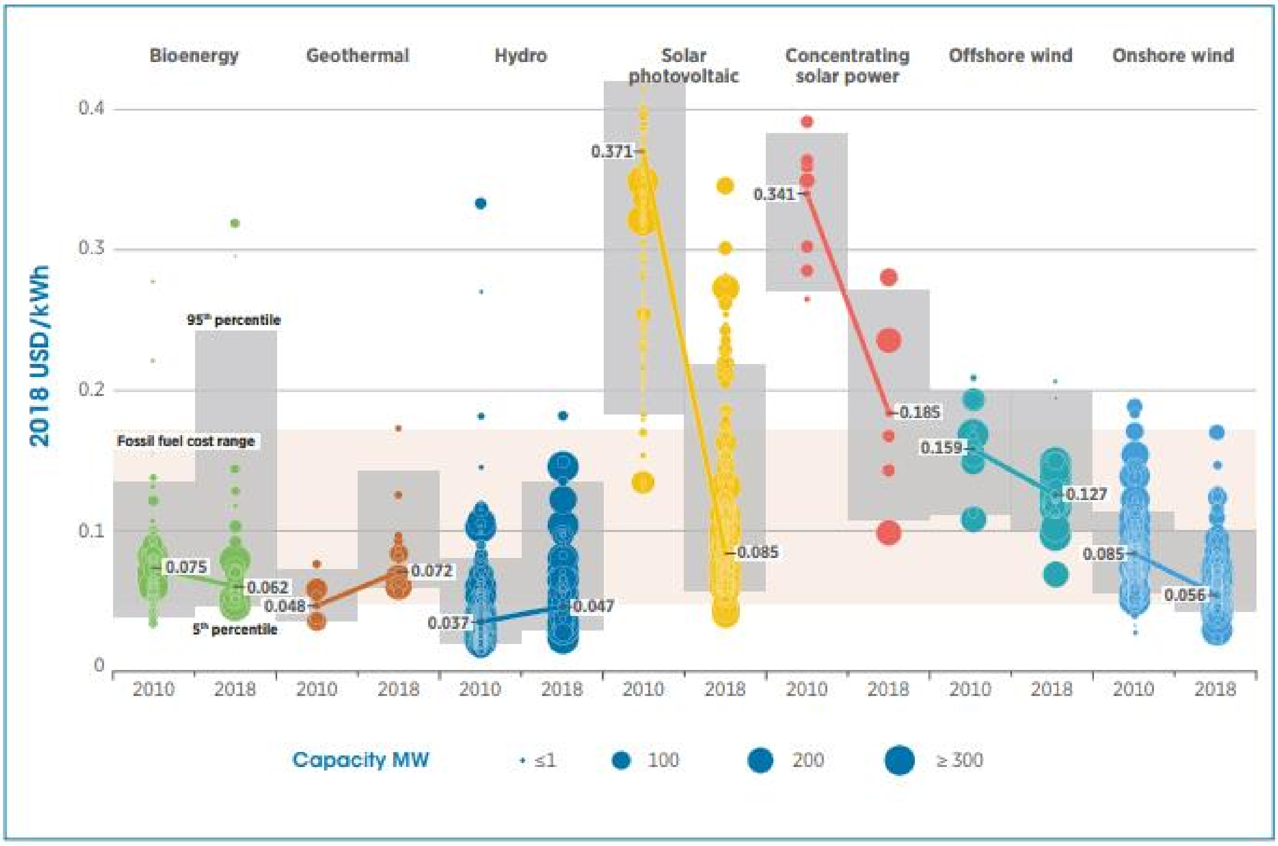

Figure 3 Global LCOE of utility scale renewable power generation technologies 2010-2018 (IRENA, 2019). The diameter of the circle represents the size of the project. The thick lines are the global weighted-average LCOE value for plants commissioned each year. Real weighted average cost of capital (WACC) is 7.5% for OECD countries and China and 10% for the rest of the world. The single band represents the fossil fuel-fired power generation cost range, while the bands for each technology and year represent the 5th and 95th percentile bands for renewable projects

Solar power is one of the most promising technologies, with the largest potential: every year 4 million EJ reaches the Earth's surface, of which 5000 EJ is considered easily harvestable *(Ehsanul Kabir et al., 2018)*, while the global yearly energy consumption in 2018 was c.a. 581 EJ *(BP Statistical Review of World Energy, 2019)*. In particular, Concentrated Solar Power (CSP) is still one of the renewable technologies with the lowest installed capacity, around 5.5 GW in 2018 according to IRENA, and for this reason, one of the most interesting, with many plants currently under construction all over the world. One more reason for its appeal is the possibility of storage. Indeed, one drawback of renewables is the energy storage at low cost, making them directly dependent on weather conditions. In this context, the strength point of CSP is the possibility to store energy in cheaper thermal storage technologies, working with different Heat Transfer Fluids (HTF), such as synthetic oil or molten nitrate salt, and different sizes, depending on the project. This allows to decouple the power production directly from the solar source and obtain a stable production also during periods of low solar irradiation, reflecting this effect on the possibility to reach low LCOEs, which dropped by 46% between 2010-18 and 26% just from 2017-18 *(IRENA, 2019)*, competitive with other renewables and also with fossil fuels.

Forecasting an increase of renewables' share in the next decades, it will be fundamental to provide a stable energy source that will integrate their variable productions (IAEA, 2018). Indeed, the future energy scenario is expected to be a mix of different sources, where a stable carbon-free baseload will be requested. Within the decarbonization context, nuclear will play a key-role as a stable and reliable baseload, essential in the energy production, actually entrusted with fossil sources. Nuclear power is considered a low-carbon energy source, also including the whole life cycle assessment, comprehensive of the waste handling, as represented in Figure 4.

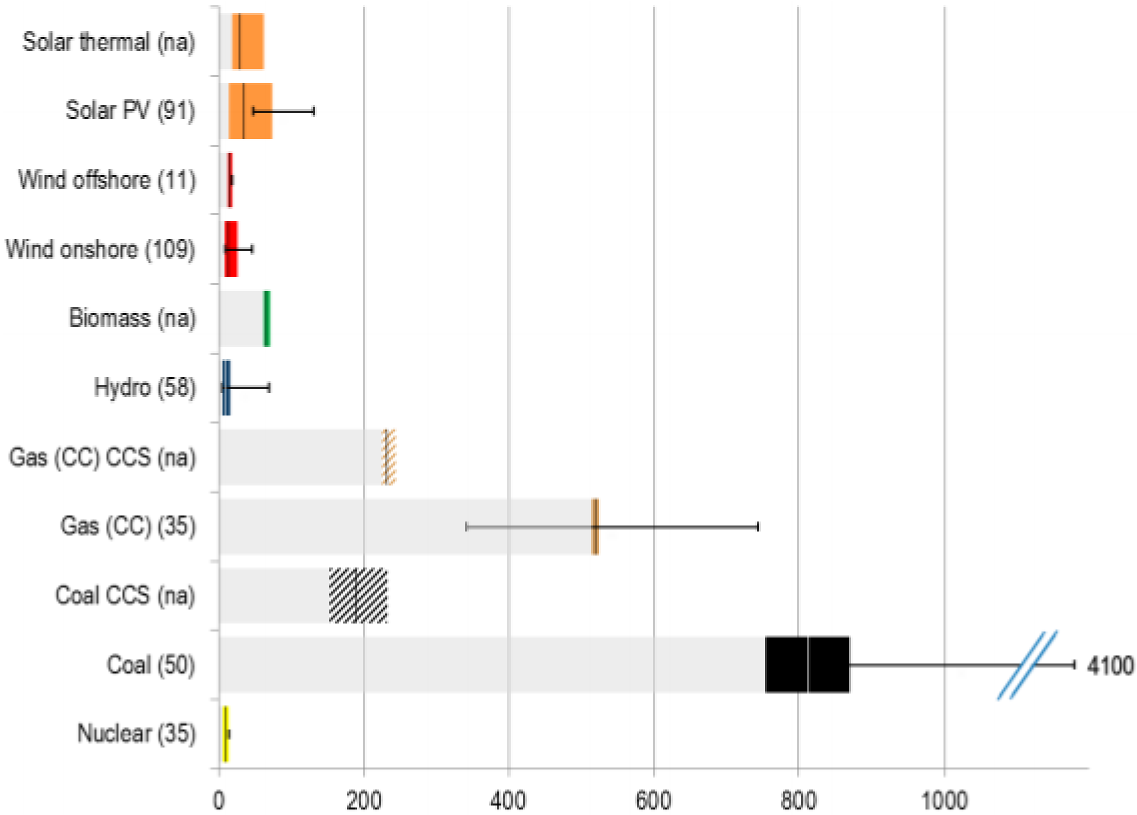

Figure 4 Life cycle greenhouse gas emissions per kilowatt-hour (g CO2-equivalent/kW-h) (IAEA, 2018). Note: Coloured ranges show regional low, average and high estimates for recently (2010) available representative technologies. Error bars indicate variation across a sample of existing power plants (based on the number of plants indicated in parentheses). CC: combined cycle, CCS: carbon dioxide capture and storage, na – not available (no data)

According to IEA, nuclear is expected to grow significantly in the future energy scenario, to witness its consistent possible contribution in the climate changes mitigation (Energy Technology Perspectives 2017). However, nuclear fission will have to face several challenges, mainly regarding safety and popular awareness; accidents in the past have modified the perception of nuclear, moving the attention more on its risks than potentials.

On the other hand, nuclear fusion is the most promising energy sources, that could guarantee a large scale, carbon-free and almost inexhaustible form of energy. Its appeal is due to several factors (ITER, 2019):

- Wide fuel availability, with high-density energy content.
- Almost null carbon dioxide emission since the physical process is totally CO2-free.
- Absence of long-term radioactive waste. Activated materials can be recycled and reused in 100 years maximum.
- No risk of meltdown, since every disturbance would cool down the plasma, shutting off the plant.
- No proliferation risk, thanks to the absence of fissile material.

However, due to the great level of complexity of the physical process and the extremely high temperatures that should be guaranteed to start the reaction (over 100M °C), it is not possible to obtain the conditions needed. Indeed, this energy technology is not available yet and still under research; the whole world is working jointly to develop it, but fusion energy is not forecasted to be commercialized in the short-term. The European Community founded in 2014 EUROfusion, a scientific program aiming at the realization of fusion, in the context of Euratom Horizon 2020 (EUROfusion, 2019).

Nowadays, the international community is focusing on the construction of ITER, an experimental reactor with the goal of producing 500 MWth, in Cadarache (France). It was planned to realize the first experiments in 2018, but the project has undergone several delays, with the first plasma reaction expected by 2035. ITER will not produce electricity, but it will be helpful in filling the knowledge gaps about fusion, essential for the construction of DEMO, a 2GW demonstration power plant, that should prove the feasibility of large-scale energy production from nuclear fusion, to further start the commercialization of this energy technology. Also in this case, the plant construction has already been delayed, originally expected to be started in 2024, now postponed to after 2040 (WorldNuclear, 2019). Therefore, nuclear fusion is not likely to be present in the energy share in the short-term, and until then, the world shall face the growing energy demand with other sources.

1.1 Supercritical Carbon Dioxide

Increasing the temperature range of operation of a power plant, has a key role in obtaining efficiency improvements. In an ideal Carnot cycle, the efficiency depends on the ratio of temperature. Therefore, decreasing the low temperature or increasing the higher, will lead to an enhancement in the system's performances. Since the low temperature is generally limited by the environmental conditions, the plant design should focus on increasing the high-level temperature to improve the efficiency of the system.

So far, the power conversion system for high temperature energy source, as CSP and nuclear, has been entrusted to Rankine steam power cycles. This type of cycle cannot be easily brought to such high temperatures, which are reflected in high pressures also. Recently, researchers focused their attention on a different type of cycle, the supercritical CO_2 Brayton cycle (SCBC), thanks to its greater inclination to work at these high temperatures (Carstens, 2004).

Brayton cycles are a well proven technology widely present on the market for their application with gas turbines. The sCO_2 power plant relies on closed, high-pressurised Brayton cycle, operating the compression near the critical point. The supercritical carbon dioxide is a fluid state of CO_2, when the fluid is maintained above the critical values of temperature and pressure, 31°C and 7.4 MPa (Figure 5). At critical conditions, the CO_2 properties become non ideal, with high density values, initially close to liquids, which confer the particular advantages of using carbon dioxide as operative fluid (Figure 6).

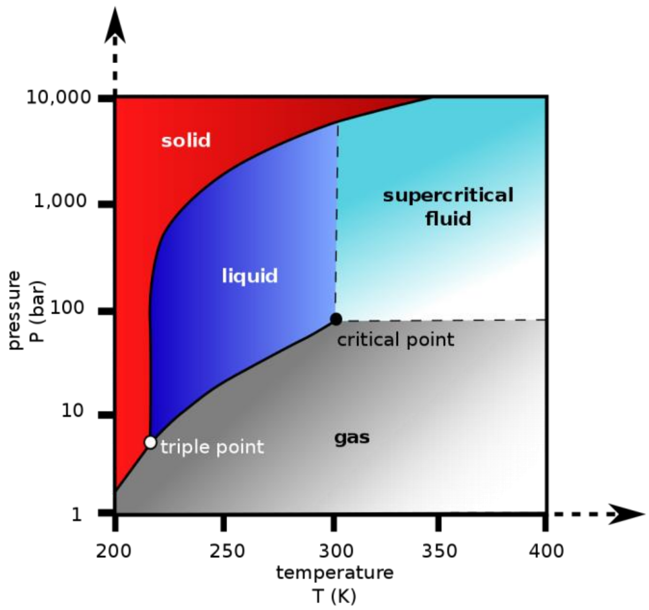

Figure 5 CO2 phase diagram (Finney and Jacobs, 2010)

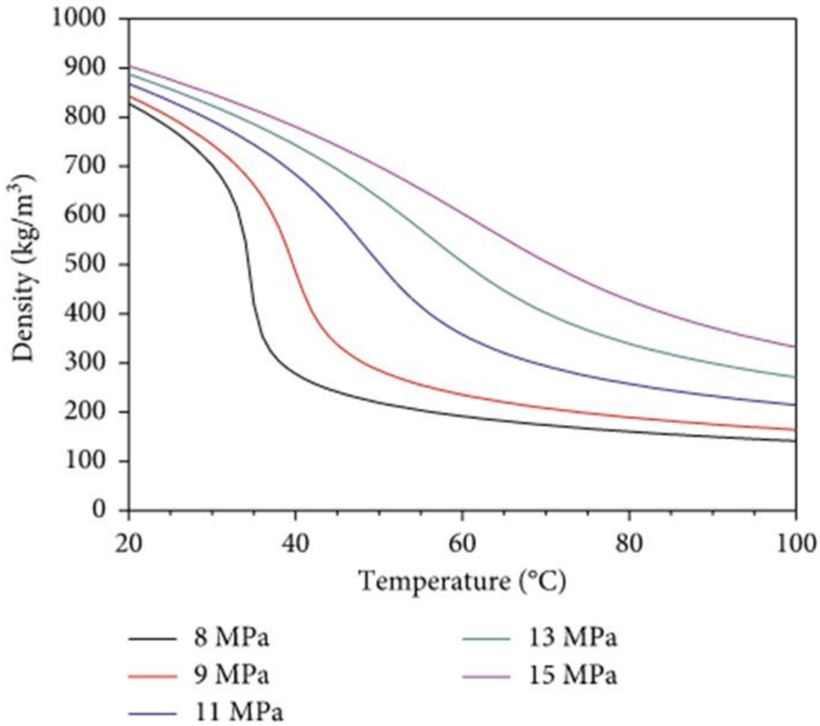

Figure 6 CO2 density as function of temperature, under supercritical pressures (Wu et al., 2020)

Therefore, operating close to the critical point, it is possible to reduce the pumping power considerably, and enhance the efficiency of conversion thermal-mechanical energy, avoiding the phase change, which is a very high energy demand and complex process. Furthermore, in the same way, it is possible to avoid the pinch problem, resulting in a better match with the heat source (Figure 7).

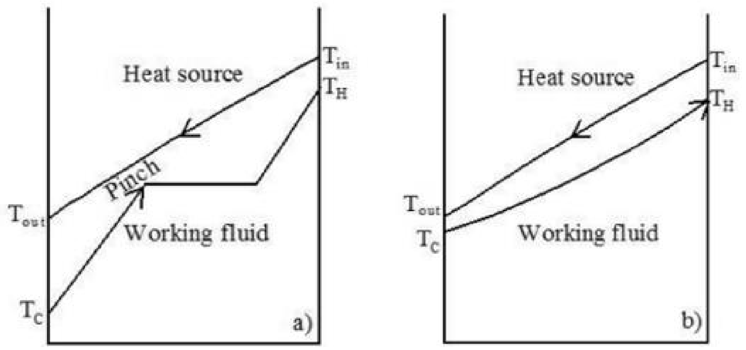

Figure 7 Temperature profiles of heat source with (a) pure fluid, (b) supercritical fluid (Andrea Baronci et al., 2015)

This type of power cycle could lead to many benefits compared to Rankine cycle:

- More compact power block size, with turbomachinery up to 10 times smaller.
- Higher conversion efficiency, theoretically 45-55% achievable (Figure 8).

- Potential reduction of LCOE and CAPEX, consequent to the previous two points.
- Reduced greenhouse gas emissions.
- Lower water consumption.
- Possible dry cooling, due to its low critical temperature.

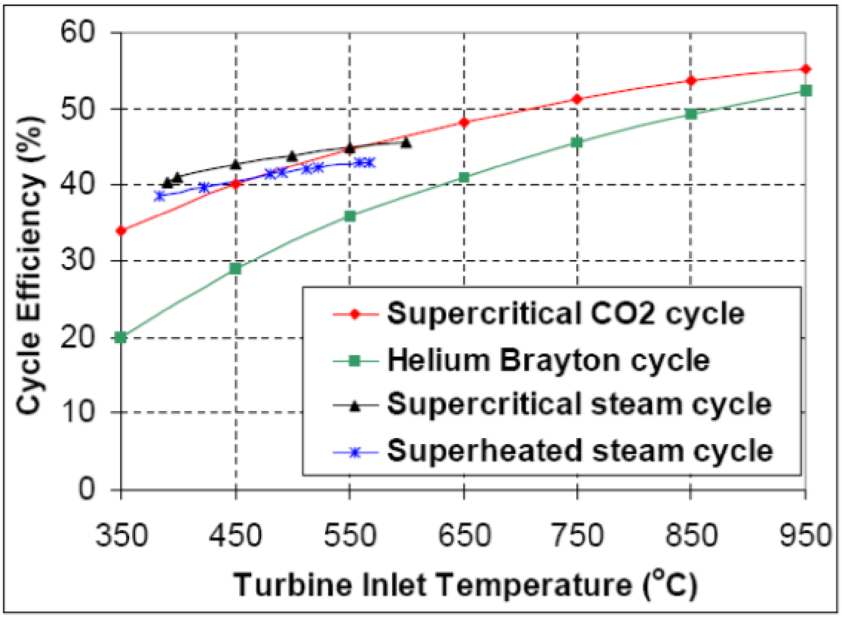

Figure 8 Theoretical efficiencies of advanced power cycles (V. Dostal et al., 2004)

The carbon dioxide's critical pressure is just 1/3 of water's, thus it allows the system to operate at relatively low pressures. Moreover, it is a low cost (1/10 of helium and 1/70 R134a), non-toxic and low corrosivity fluid, thermally stable in the temperature ranges of the CSP, and flexible to the heat source, with possible applications in CSP, nuclear, high-temperature fuel cells and waste-to-power plants (SNL, 2015; Ty Neises, NREL, 2013). However, sCO_2 cycles are not new: they were designed at the end of 60' but abandoned for a long time, and recently restudied by the US (Angelino, 1968; Steven et al., 2008). Research in sCO_2 has been very active in the past years; Liu et al., published a review of the state of the art for SCBC in 2019 (Liu et al., 2019).

The so-called Brayton cycle, or also known as-Joule cycle, is one example of thermodynamic cycle, a series of thermodynamic transformations applied to an operating fluid, at the end of which it will return to its initial conditions. In particular, the Brayton cycle is part of the power cycles, so called since their purpose is the conversion of thermal energy into mechanical. The Brayton cycle was firstly depicting a gas turbine engine operation, designed in 1872 by the American engineer George Bailey Brayton. The ideal cycle is composed of four processes: 2 isentropic and 2 isobaric (Figure 9 - Figure 10).

1-2 Isentropic compression with no heat exchange. The pressure level is increased thanks to the compressor operation and energy expense.

2-3 Isobaric heating. The fluid's temperature, and consequently enthalpy, is here increased by the heat source, maintaining the pressure constant.

3-4 Isentropic expansion with no heat exchange. Fluid is forced to pass through a turbine to a lower pressure level, where it induces the rotation of the rotor, releasing part of his energy. In this transformation, mechanical power is generated.

4-1 Isobaric cooling. The thermodynamic conditions return as the ones of the first reaction, releasing heat from the fluid to a heat sink. If the cycle is opened, the cooling consists pf releasing the exhaust gasses to the environment, while in the case that it is a closed cycle, the transformation happens inside a cooler.

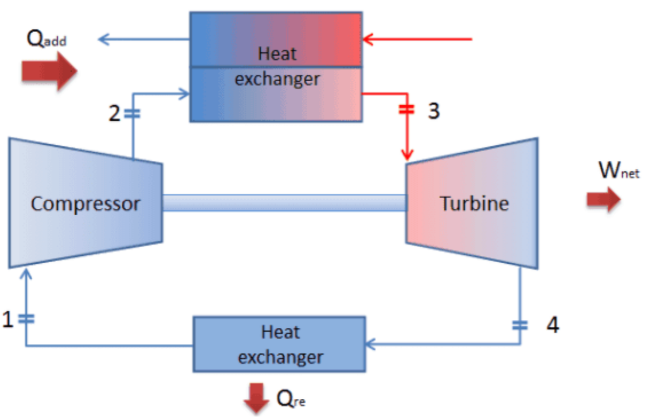

Figure 9 Brayton cycle scheme

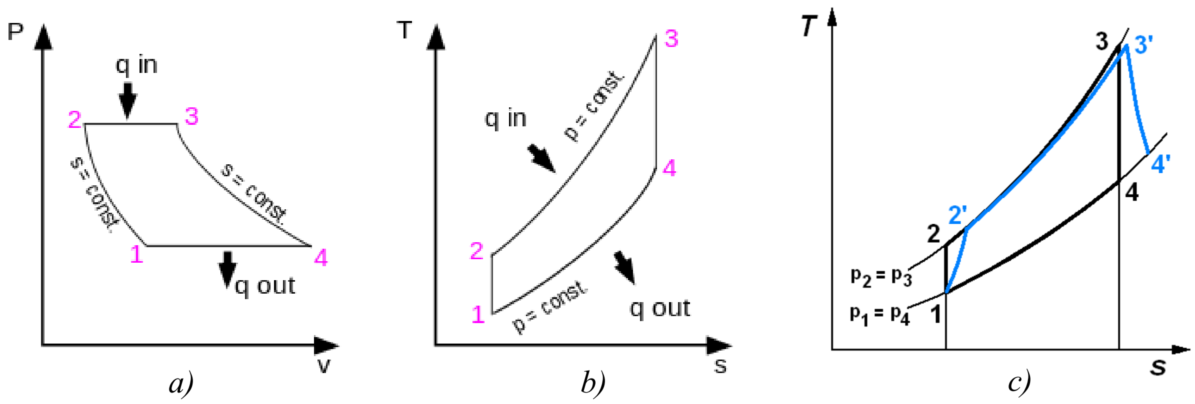

Figure 10 Brayton cycle thermodynamic diagrams: P-V ideal a), T-s ideal b) and T-s real c) (NASA, 2015)

In reality, it is not possible to avoid the generation of entropy in compression and expansion, as the heat exchange will also not be perfectly isobaric. Thus, turbomachinery components are characterized by an isentropic efficiency, which quantifies the deviation from the isentropic reaction. Regarding the compressor, the generation of entropy will imply a greater outlet enthalpy, so its isentropic efficiency is defined by Equation (1).

$$\eta_{iso,comp} = \frac{h_{out,iso} - h_{in}}{h_{out,real} - h_{in}} = \frac{h_2 - h_1}{h_{2'} - h_1} \tag{1}$$

While, for the turbine the situation is exactly the opposite, since the increment of entropy will limit the enthalpy difference possible, as can be seen in Equation (2).

$$\eta_{iso,turb} = \frac{h_{in} - h_{out,real}}{h_{in} - h_{out,iso}} = \frac{h_{3'} - h_{4'}}{h_{3'} - h_4} \tag{2}$$

Moreover, for power cycles, it is possible to define the thermal efficiency η_{th}, defined by Equation (3) as the percentage of heat provided to the fluid which is converted into mechanical work, and computed as the ratio between the net power output and the heat entering the system.

$$\eta_{th} = \frac{W_{net}}{Q_{in}} = \frac{W_{turb} - W_{comp}}{Q_{in}} \tag{3}$$

Compared to the basic layout, improved configuration can give better efficiencies. This is the case of the recuperative Brayton cycle (Figure 11). In it, a further heat exchanger is present, called recuperator, whose goal is to preheat the compressed fluid before the heater, with the gasses exiting the turbine. In this way, part of the heat that should be dissipated is conferred to the fluid, reducing the power needed from the heat source. Although, for temperature reasons, not all the heat available in the exhaust fluid can be exploited. Part of it will have to be released out of the cycle, to a heat source at a lower temperature.

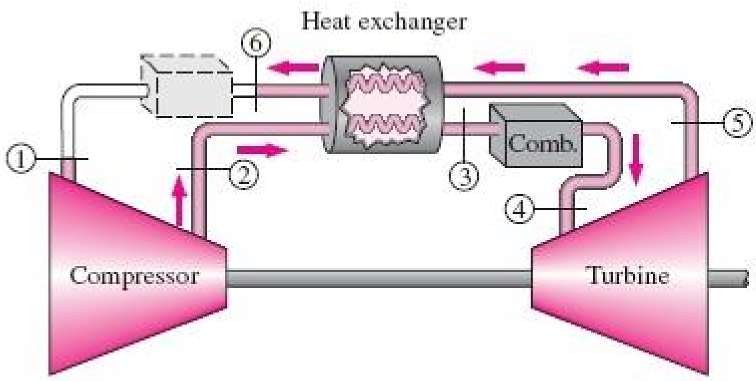

Figure 11 Recuperative Brayton cycle plant sketch

1.2 Background on sCO_2 Brayton cycle modelling

The recuperative layout is just one of the many suitable, with which it is possible to reach higher cycle efficiencies. Depending on the application the optimal layout could be different, therefore, a dynamic simulation of the system of interest is the key to find the optimal configuration and operation of the power cycle. In the last decade, many researchers focused on simulation of SCBC, motivated by the considerable improvements that this loop could bring. What appears from literature, is the growing interest in the control strategies for this type of power cycle, key to enhance its presence in the technological market.

In this context, it is important to take advantage of a flexible and powerful dynamic tool to simulate the system. Many of them are available and have been widely used in research.

Studies about SCBC coupled with nuclear plants have been done by Wu in two different articles: in the first, he developed an upgrade of SCTRAN code, originally created for safety analysis in SCWR, to simulate sCO_2 Brayton cycles. After the addition of thermal and mechanical components needed, he simulated a closed Brayton cycle, and validated the results again RELAP-5 and experimental data. In the second paper, he presented another solver, SASCOB, a steady thermodynamic analysis solver, used for the simulation and optimization of a SCBC connected to a lead fast reactor, testing different types of cooling. The results show the improvement in passing from a simple Brayton configuration to a recompression layout, validated against data obtained by MIT (Wu et al., 2020, 2018).

The thesis by Carstens brilliantly investigates the dynamic modelling of sCO_2 power cycles for IV generation nuclear reactors using GAS-PASS, a simulation code developed specifically for IV generation nuclear gas reactors, used for safety analysis and control (Carstens, 2004). In his work, Carstens modelled many part-load operations strategies, suggesting the most effective.

Also in solar energy the research about SCBC power cycles is very active. Here the control is even more challenging due to important and sharp perturbations, effect of the transitory nature of irradiation and weather conditions, leading to a strong nonlinear behaviour. Moreover, keeping the supercritical state at the compressor inlet, the closest part to the critical point, during transient periods is a complex task, that could cause damages to the component if not satisfied (Singh et al., 2013b). Iverson et al., investigated the response of a sCO_2 Brayton turbomachinery consequently to a rapid and sharp heat source variation, simulating fluctuations of solar radiation availability. The model has been validated against experimental data with good agreement, showing that, thanks to its mass, the loop is able to operate for short periods of heat source deficiency (Iverson et al., 2013).

Neises and Turchi focused their study on researching the optimal cycle configuration for solar purposes, between simple, recompression and partial cooling configurations, finding the best choice in the partial-cooling cycle, under both efficiency and economical aspects (Neises and Turchi, 2014). In addition, other configurations were analysed, including regenerative, pre-compression and split expansion, in combination with a solar tower power plant. In a study from Al-Sulaiman, the optimum was found with the recompression option, reaching 52% of cycle efficiency and 40% for the whole system (Al-Sulaiman and Atif, 2015). A dynamic model of recompression cycle was also developed by Casella in 2011 with Modelica, a simulation language with many environments available on the market, such as OpenModelica, CATIA Systems, MapleSim, and Dymola. The author tested an open Brayton cycle in order to show the potentials and flexibility features of Modelica, with a detailed explanation of the language (Casella and Colonna, 2011).

Moreover, Ma and Turchi investigated the possibility of using carbon dioxide also as HTF, in the so called directed-heated SCBC, allowing higher operation temperatures with greater efficiency, eliminating the freezing risk typical of the molten salt, and leading to a cost reduction by removing one of the heat exchangers. On the other hand, the high pressures that should be maintained in the whole solar field and the lack of experience in SCBC are the challenges that have to be faced (Ma and Turchi, 2011). Studies on this type of cycle have been carried out also by Singh at al., who proposed an extremum-seeking control to maximize the power output and manipulating the flow of carbon dioxide, depending on the available radiation and ambient temperature (Singh et al., 2013a). The same author simulated on Modelica different climate conditions and solar irradiation applied on a 1 MWe direct heated sCO_2 loop coupled with a trough solar plant, investigating the mass movements between hot and cold side of the loop, showing the effects of its fluctuations. Active control of the cycle and stabilization of the mass flow are required to guarantee the critical conditions of the fluid and the optimal turbomachinery operation (Singh et al., 2013b).

A directed Brayton loop was also the object of the study by Hakkarainen, who simulated with Apros two designs of CSP with central receiver, one direct and one using a double tank molten salt storage system, benchmarking the results. Clearly, the advantage resulting from having a TES system consisted of the possibility to guarantee a stability during the day, also without irradiation (Hakkarainen et al., 2016).

MATLAB also proved to be a useful solution for dynamic modelling of CSP plants with sCO_2 Brayton cycle as a power conversion system. With it, Osorio et al. examined the loop's behaviour with different seasonal weather conditions, highlighting the effect of design and operating parameters on its performances. Different plant configurations are presented, with their relative efficiencies (Osorio et al., 2016). MATLAB was also used to set an optimization strategy for a recompression SCBC, based on the split fraction and the recuperator effectiveness, showing their tight relation and finding the optimal value of split factor in 75% (Reyes-Belmonte et al., 2016). A start-up scheme for a similar plant was prosed, using Modelica. Moreover, the code has been useful to simulate a loss of charge event consequent to an incident as well, showing a high system's resistance to drops in density, being able to maintain the supercritical condition during almost the whole event (Luu et al., 2017).

1.3 Scope of the work and Thesis organization

The present thesis work is centred on developing a dynamic model of a supercritical CO_2 Brayton power cycle, aimed at the design of loop's control systems. The modelling has been performed with Modelica, an open-source, object-oriented, multi domain modelling language, with many simulation environments available. The one used here is Dymola, a commercial software released by Dassault Systemes. Different open-source libraries provided the components needed for this purpose: ThermoPower, ExternalMedia, and SolarTherm. Appendix A contains a detailed description of Modelica, Dymola and the libraries used.

This project has been developed in collaboration with the nuclear department of Universitat Politècnica de Catalunya, UPC (Barcelona, Spain). UPC currently partner with Comillas Pontificial University (Madrid, Spain), working for the company CIEMAT in the framework of nuclear fusion research, funded by the EUROfusion Programme (Euratom Horizon 2020) (Linares et al., 2018). The two universities have been working on modelling of sCO_2 cycles for nuclear applications for several years, Comillas using the Engineering Equation Solver (EES) and UPC working with RELAP-5. The results obtained in this thesis have contributed to the development of an internal report of Comillas University for CIEMAT.

Comillas University provided a reference steady state sCO_2 power cycle developed in 2017 with the EES, which has been used as guideline for this work. Firstly, a steady state model with the same layout has been created in Dymola and benchmarked with the reference, to prove the validity of the results. Secondly, the layout has been improved to be more adherent to reality, resulting in more reliable outputs, which have been further upgraded to perform dynamic simulations, aimed at the definition of control techniques. This resulted in the integration of three PI controllers and the proposal of two possible part-load operation strategies.

The first part of this document will initially illustrate the reference loop, followed by the step-by-step description of the Modelica cycle's construction, with a first general overview, then focusing on single components. Afterwards, the steady state of the two layouts, the one identical to the reference and the improved version, will be reported and benchmarked with the reference data. Lastly, the dynamic simulations results will be presented, from the insertion of the PIs to the partial load operation strategies, finally followed by the future work that could be done to further improve the model.

2 System Description

A recuperative 800MW supercritical sCO_2 Brayton cycle has been developed in Modelica using the Dymola environment, taking as reference an equivalent loop designed by Comillas University, through the Engineering Equation Solver (EES) environment.

In the past years remarkable work has been done by the Spanish University on finding the optimal design, leading to several different cycle configurations. The one presented here is the second version of 2017, although not the newest, it is the easiest to model and to be adapted to dynamic applications. The cycle is formed by one compressor (C), one turbine (T), and 3 sets of 3 heat exchangers, in order to contain their size: high temperature molten salt heat exchanger (HTS), high temperature recuperator (HTR) and pre cooler (PC). Figure 12 illustrates the plant scheme, while Figure 13 shows its 2D and 3D graphical representation.

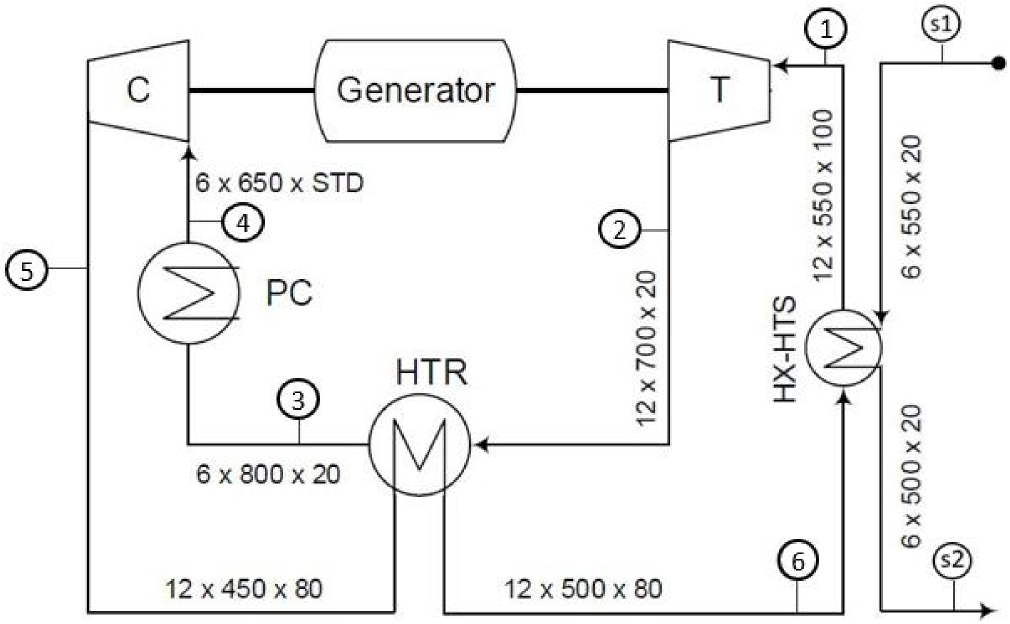

Figure 12 Scheme of the reference cycle. S1 and S2 are respectively the molten salt inflow and outflow

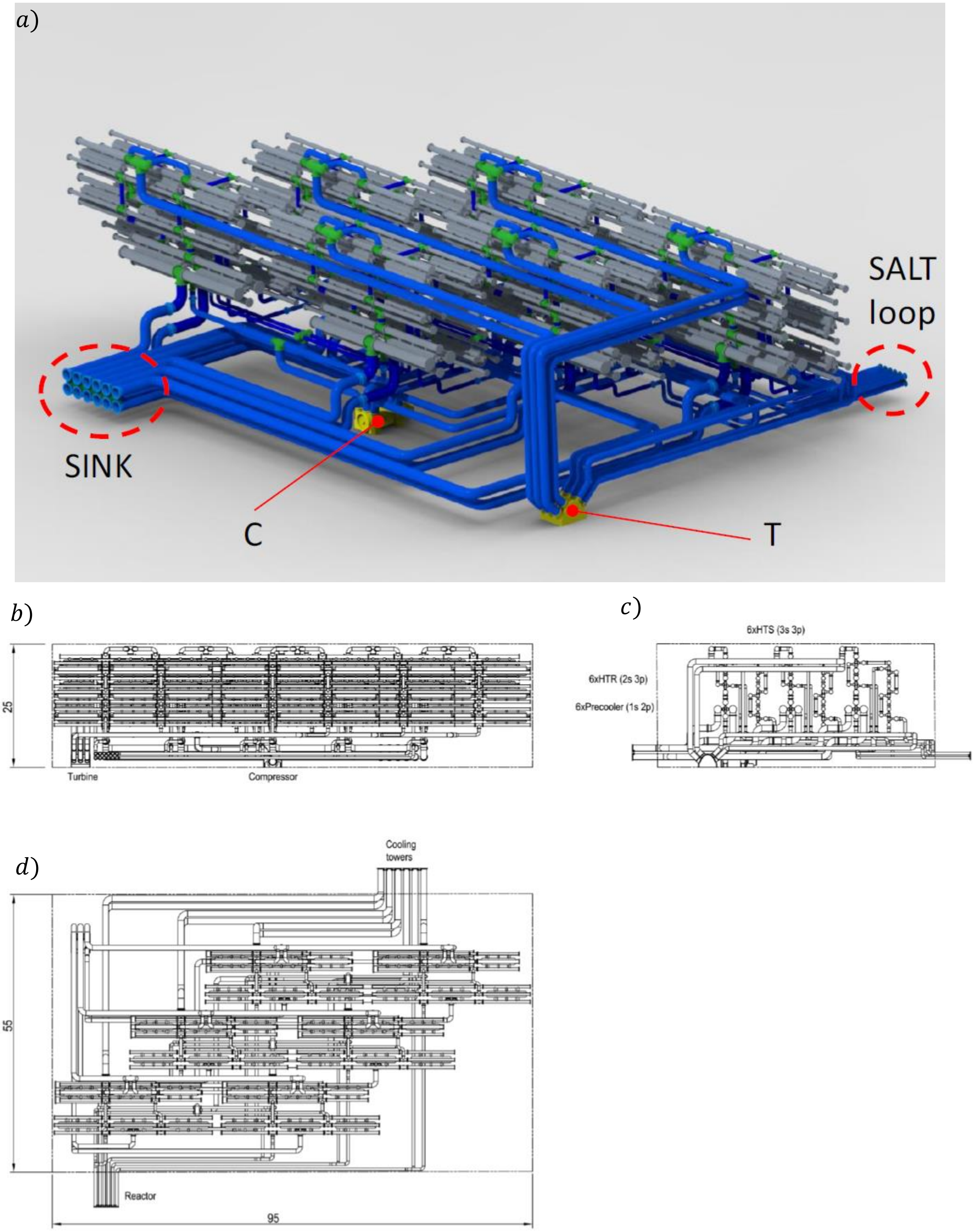

Figure 13 Power cycle a) 3D perspective and 2D CAD sketch of the b) front, c) side, d) aerial view with dimensions in meters

The EES which contains the definitions of some pure substances such CO_2, water and helium, while for the molten salt (HITEC) have been considered the parameters summarized in Table 1.

Table 1 HITEC molten salt properties considered by Comillas

$\boldsymbol{\rho\left[\frac{kg}{m^3}\right] = 2080 - 0.7324 \cdot T[°C]}$
$\boldsymbol{c\rho\left[\frac{kj}{kg\,K}\right] = 1.56}$
$\boldsymbol{h\left[\frac{kj}{kg}\right] = -276.12 + 1.56 \cdot T[°C] + \frac{P[kPa]}{\rho\left[\frac{kg}{m^3}\right]}}$
$\boldsymbol{\mu[Pa \cdot s] = 2.1554 \cdot 10^{-4} \cdot e^{\frac{1006.4131}{T[°C]+83.7755}}}$
$\boldsymbol{k\left[\frac{W}{m\,K}\right] = 0.4465 + 0.1788 \cdot 10^{-3} \cdot T[°C] - 1.1486 \cdot 10^{-6} \cdot (T[°C])^2}$

The plant's design power is 800 MW, with 6912 kg/s of CO_2 circulating, working in the pressure range between 85 and 300 bar, while the temperature varies from 35 °C to 490 °C. Fixed mass flow rates of molten salt and water were considered in the HXs, respectively 6184.6 kg/s and 29297 kg/s. Ideal assumptions were made on the turbomachinery due to lack of data, considering components with fixed efficiency, based on literature available (Bahamonde Noriega, 2012). It must be highlighted that, even though the pipes were sized and present in the sketches, in the model they were not considered, therefore the system does not yet result in a realistic configuration, with a smaller volume than the real one. The components description and their sizing strategy is presented here.

- Compressor: component with inlet conditions set at 35°C and 85 bar, whose efficiency was considered constant at 88%.
- Turbine: like the compressor, the turbine is operating with fixed efficiency set at 93%. Inlet design conditions are set at 490°C and 300 bar.
- Pipings: two criteria were used in order to establish the pipe size. Firstly, the maximum velocity criterion was used to obtain the minimum diameter, following the NORSOK P-001 standard (California Energy Commission, 2015; Standards Norway, 2006). Suitable materials were found in alloy Inconel 740H for CO_2, carbon steel A-106B for water pipes and high chromium stainless steel SS-347H for molten salt. Once the materials have been determined, minimum wall thickness was computed (ASME B31.1, 2007). Then, through an iterative process, normalized diameter and thickness were found. Finally, the maximum pressure loss criterion was used to check that the head losses were lower than the limits established by NORSOK standards. The computation of pressure drop was performed using the Darcy-

Weisbach and Colebrook equations. As already mentioned, pipes were sized but not yet included in the 2017 model.

- Heat exchangers: in the 2017 layout, all the heat exchangers were Printed Circuit Heat Exchangers (PCHE), because of their resistance to high pressure, compactness and possibility to reach small pinch points and high efficiency (Halimi and Suh, 2012), although in the future layouts, the molten salt heat exchanger will be a shell and tube type, due to reported problems of clogging and thawing. The real PCHE device designed by Heatric, was used as base reference for number of channels and module dimensions. Every module of the heat exchanger is formed by 96000 semi-circular microchannels, dedicated half to the hot fluid and the other half to the cold, formed by alternating layers of etched plates (Figure 15 andFigure 14). The frontal dimensions are 0.6, x 0.6m giving 0.36 m^2 each. Different channels dispositions are available in PCHEs (e.g. parallel straight, zig-zag), in this case, the exchanger was considered with straight and parallel semi-circular pipes.

  The sizing procedure of the computer model starts with their discretization in sub exchangers using the correlations proposed by Yang et al. (Yang et al., 2017). Through an iterative process, energy equation, pressure drops and heat transfer coefficients were computed, obtaining the heat exchanger's length using the Log Mean Temperature Difference (LMTD) method. The correlations used are Gnielinski (Gnielinski, 1976) for the heat transfer coefficient, while the procedure proposed by Dostal (V. Dostal et al., 2004) was used for the friction factor evaluation.

  The last step consists of the verification that the number of channels and length per-module don't exceed the real manufacturer capability, nominally 96000 channels and 1,5m of length.

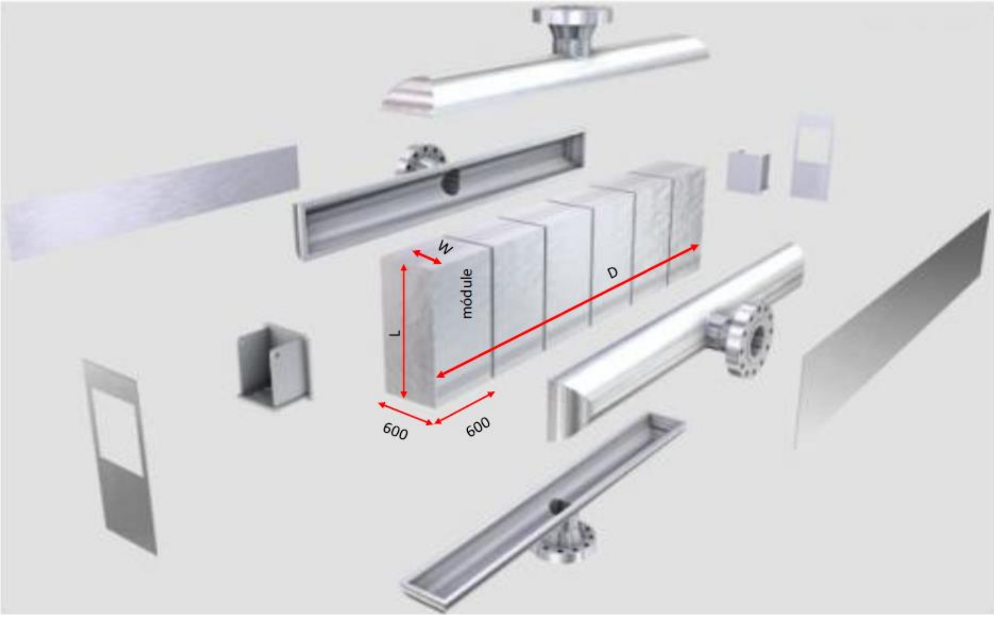

Figure 14 Schematics of a PCHE. L is the module's length, W the frontal dimension, D the width given by the number of modules in parallel

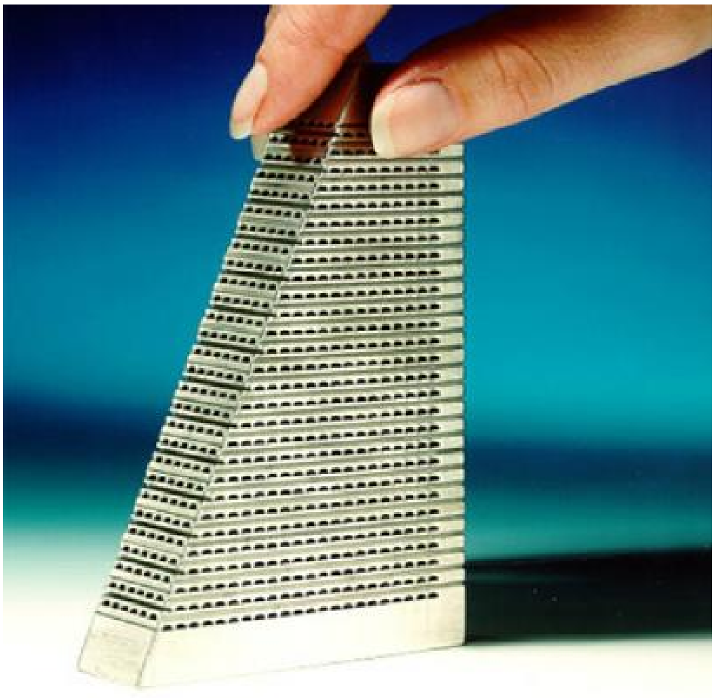

Figure 15 PCHE section showing the semi-circular microchannels

2.1 Modelica Cycle

The Modelica model have being built with large use of available libraries: ExternalMedia and SolarTherm contained the definition respectively of the carbon dioxide and molten salt as medium, while the ThermoPower library, provided all the mechanical and thermal components used in the loop, eventually adapted to the CO2 medium or upgraded for specific uses. Moreover, minor blocks, mainly logical, have been created from scratch for different purposes, especially in the dynamic section, in order to activate features in different moments.

The construction started with a deep study of the components available in the libraries, understanding their functioning and which one could have been used, eventually updating them for the applications of interest. At first, the loop was modelled open, adding one component per time and testing their correct operation, refining the initial conditions to better initialize the code. Once the open loop was working, the configuration has been upgraded to a closed loop.

Initially, the closed layout modelled was the same as Comillas, in which the pipes connecting the different elements were not taken into account, as well as the local pressure drops for flow expansion and contraction, occurring when the fluid enters or exits the connection elements of the heat exchangers. Once obtained a stable and working layout, the cycle has been further improved, including also pipings and local pressure losses. The configuration so obtained is clearly more realistic, and consequently, of greater interest, even though many simplifications are still present compared to a real cycle, especially regarding the turbomachinery which will be later fully explained.

Firstly, the two systems have been tested in steady state conditions to be compared with the reference cycle, then, the second configuration was used as base to be further tested in dynamic applications and design of control systems.

It is important to highlight that just the sCO_2 loop has been modelled, while heat source and sink have been simulated as fixed mass flow rates, respectively of molten salt and water. Therefore, those mass flows are considered boundary conditions of the system, better explained in the steady state operation section.

In this section the second case will be described, due to its greater completeness; the simplified loop will consist of the same components, excluding pipings and local pressure drops. In the following pages the description of single components will be presented, explaining how they have been built, which tools have been used, and emphasizing the differences between the loop introduced here and the reference one.

2.1.1 *Components*

2.1.1.1 Turbomachinery

Turbomachinery for SCBC is one of the main peculiarities of the sCO_2 Brayton cycle. Indeed, thanks to the particular physical characteristics of the CO_2, it is possible to obtain components very compact, with respect to the ordinary machinery of the same power used in classical power cycle, as Rankine or gas Brayton, resulting in advantages both in terms of space occupied and cost reduction. Choosing an operating point for the compressor close to the carbon dioxide's critical point, allows it to get high values of density, close to typical liquid values, while at turbine's exit it is possible to reach densities 10000 times higher than an ordinary condensing steam cycle and 100 times more than combustion gas turbine (*Fundamentals and applications of supercritical carbon dioxide (sco2) based power cycles*, 2017).

The turbomachinery block was imagined to be co-axial, where the turbine can drive both compressor and a synchronous generator, setting 3000 rpm as velocity for both the components. Compressor and turbine models are two of the main differences with the reference model; in it, ideal components with fixed efficiency have been used, while in this work, performance maps were used to run the devices to get a more realistic result but implying lower efficiencies than the reference.

2.1.1.1.1. Compressor

The compressor model resulted in being the most sensible and difficult-to-start component, since it is the driving force of the fluid in the whole cycle. Comillas University designed a model using specific software, from which it was possible to define machine type, diameter and number of stages, and finally, extract the performance tables, used to feed the Modelica model.

Some difficulties came up in this process, mainly due to the scarcity of experience in designing compressors of such dimensions, since markedly bigger than sCO2 compressors available on literature and on the market. Indeed, the component operation showed some imperfection in its design, resulting to be slightly oversized and not optimized for the nominal mass flow rate present in Comillas' cycle. Therefore, the inlet design values provided by Comillas have been modified in order to make the component operating with the same pressure ratio as the reference cycle with nominal conditions.

Performances maps

The methodology adopted by Comillas University was the Baljé method (Balje, 1981), which affirms that well-designed turbomachines show recurrent values for the a-dimensional parameters *specific speed* (N_s) and *specific diameter* (D_s) (Equations (4) and (5)).

$$N_s = \frac{\omega\sqrt{V_1}}{(gH_{ad})^{3/4}} \tag{4}$$

$$D_s = \frac{D\cdot(g\cdot H_{ad})^{1\backslash 4}}{\sqrt{V_1}} \tag{5}$$

Where ω is the rotational speed in [rad/s], V_1 the volumetric flow (compressor inlet or turbine outlet) in [m^3/s], g is the acceleration of gravity [m/s^2], H_{ad} the adiabatic head drop [m] and D is the diameter of the rotor [m].

Therefore, knowing the operating conditions, it is possible to obtain these a-dimensional values, and, in case they not lie in high-efficiency areas, the mass flow can be split in parallel components of several stages to obtain values in accordance with the guidelines provided by Fuller et al. (Fuller et al., 2012). Following le literature indications, axial type was preferred to radial, in order to guarantee high performances at off-design conditions (*Fundamentals and applications of supercritical carbon dioxide (sco2) based power cycles*, 2017). Once the configuration has been set, N_s can be computed, corresponding to a $D_s$value on the Baljé diagram. From it, is possible to derive the real diameter. As last step, using COMPAL™ it was possible to obtain the performances curves, in terms of a-dimensional parameters: relative mass flow rate (ν) and relative velocity (α), described by the equations (6) and (7).

$$\nu = \frac{\frac{\dot{m}}{\rho_{0,in}a_{0,in}}}{\left(\frac{\dot{m}}{\rho_{0,in}a_{0,in}}\right)_{rated}} \tag{6}$$

$$\alpha = \frac{\frac{\dot{N}}{a_{0,in}}}{\left(\frac{\dot{N}}{a_{0,in}}\right)_{rated}} \tag{7}$$

Where $\dot{m}$ is the mass flow [kg/s], ρ density [kg/m^3,] a the sound velocity [m/s]. As mentioned above, the original rated values have been modified in order to obtain the same pressure ratio as the reference when operating with its thermodynamic conditions; the path followed for their evaluation is reported in Appendix B. Table 2 resumes the final inlet rated parameters used.

Table 2 Modified compressor inlet rated parameters

New Inlet Design Conditions		
$\boldsymbol{\rho}$	612.12	[Kg/m3]
$\boldsymbol{a}$	235.06	[m/s]
N	3000.00	[rpm]
$\dot{\boldsymbol{m}}$	6764.30	[kg/s]

The compressor performances curves are shown below in Figure 16, while in appendix (Table C. 2) will be reported the numerical values. It must be highlighted that the compressor will not be able to operate with the same efficiency as the reference compressor, since the maximum value reachable is around 85%, against 88% of the ideal device.

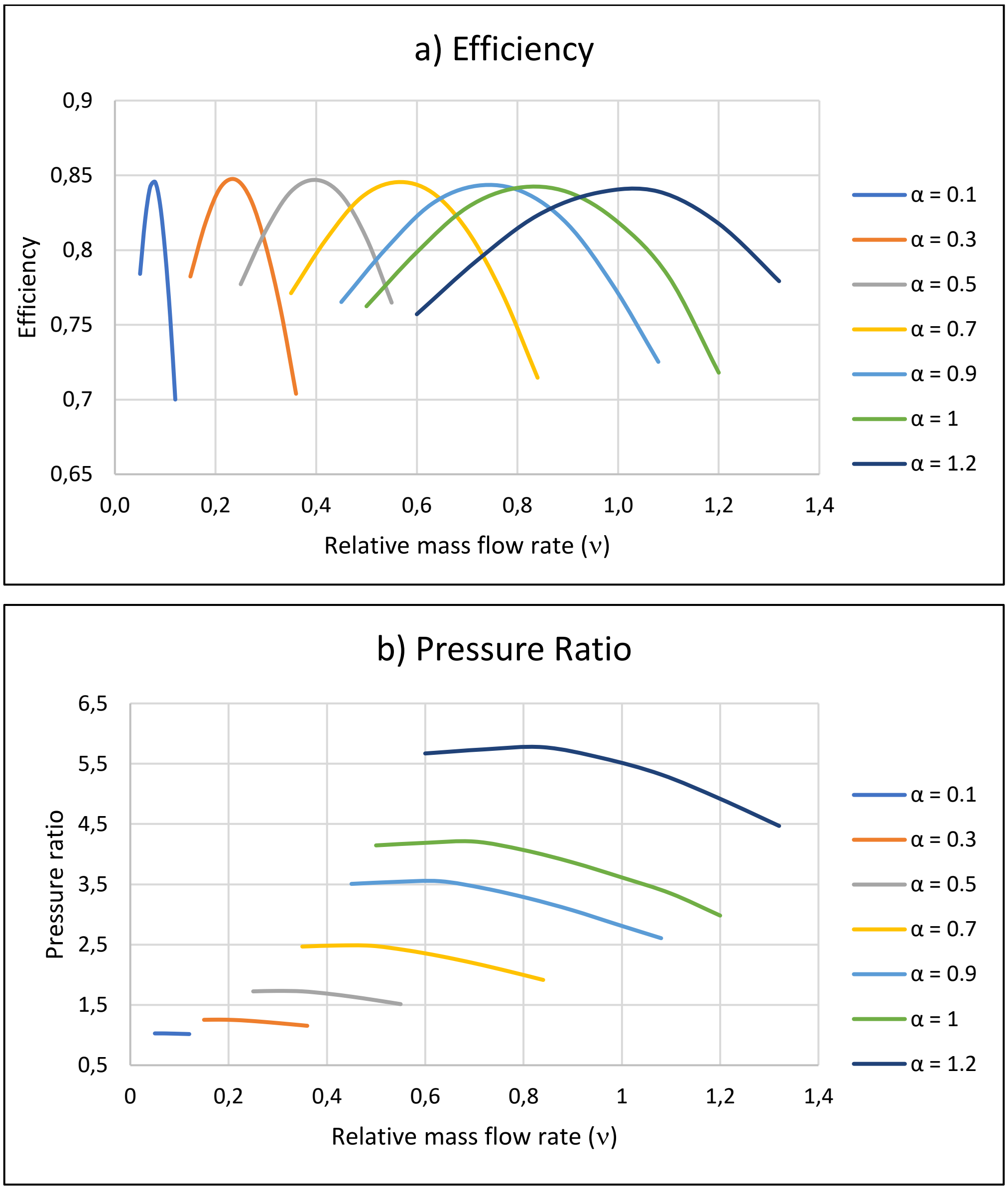

Figure 16 Compressor performances maps in terms of a) efficiency and b) pressure ratio

Component definition

The compressor model was constructed starting from the example available in the ThermoPower library (*'ThermoPower.Gas.Compressor'*). The device there present is considered without volume and inertia, working with a-dimensional performance maps, taking advantage of the beta-line method (Gonzalez Gonzalez, 2018), in which the performance characteristics equations are related with a further parameter *beta* to avoid singularities. The performance parameters used, nominally the flow number "*Phic*", isentropic efficiency "η", pressure ratio *"PR"*, are provided under the form of 2D tables, function of the referred speed *"*N_T*"* and *"beta"*. A more detailed explanation of flow number and referred speed is present in Appendix (Table C. 1). It is possible to provide the tables either explicitly as numbers in the code, or as a text file.

With the values of efficiency and pressure found, based on the fluid inlet conditions, the block computes the outlet values of pressure and enthalpy according to the compressor isentropic efficiency formula defined in equation (1). Finally, the power required by the compressor is calculated as reported in Equation (8).

$$Power = \dot{m}\,(h_{out} - h_{in}) = \tau \cdot \omega \cdot \eta_{mech} \tag{8}$$

Where τ is the torque acting on the compressor, ω the angular shaft velocity, and η_{mech} the mechanical efficiency of the device, assumed to be 0,98.

On this basis, the component was adapted in order to be fed by the performance tables provided by Comillas. Therefore, the definition of flow number *Phic* has been removed, as well as related parameters and the tables above mentioned, and substituted with the equations (6) and (7), defining the inlet design values (Table 2) as parameters and running the device with constant speed, 3000 rpm.

Then, Comillas' maps should be supplied. Therefore, two new 2D tables were built, one for efficiency and one for pressure ratio, as function or relative mass flow rate and relative velocity. To do that, the maps had to be extended for computational reasons, in order to have for each value of relative mass flow, a resulting value efficiency and pressure ratio for each velocity. The extension has been performed using a polynomial trendline, from which the algebraic equation was extracted. In case of values out of range, they have been manually limited to reasonable numbers: efficiencies below zero have been converted in 1E-5, slightly higher than zero for computational reasons, and PR below 1 have been restricted to 1.

The curves so obtained show good agreement with the originals, as shown in Figure 17.

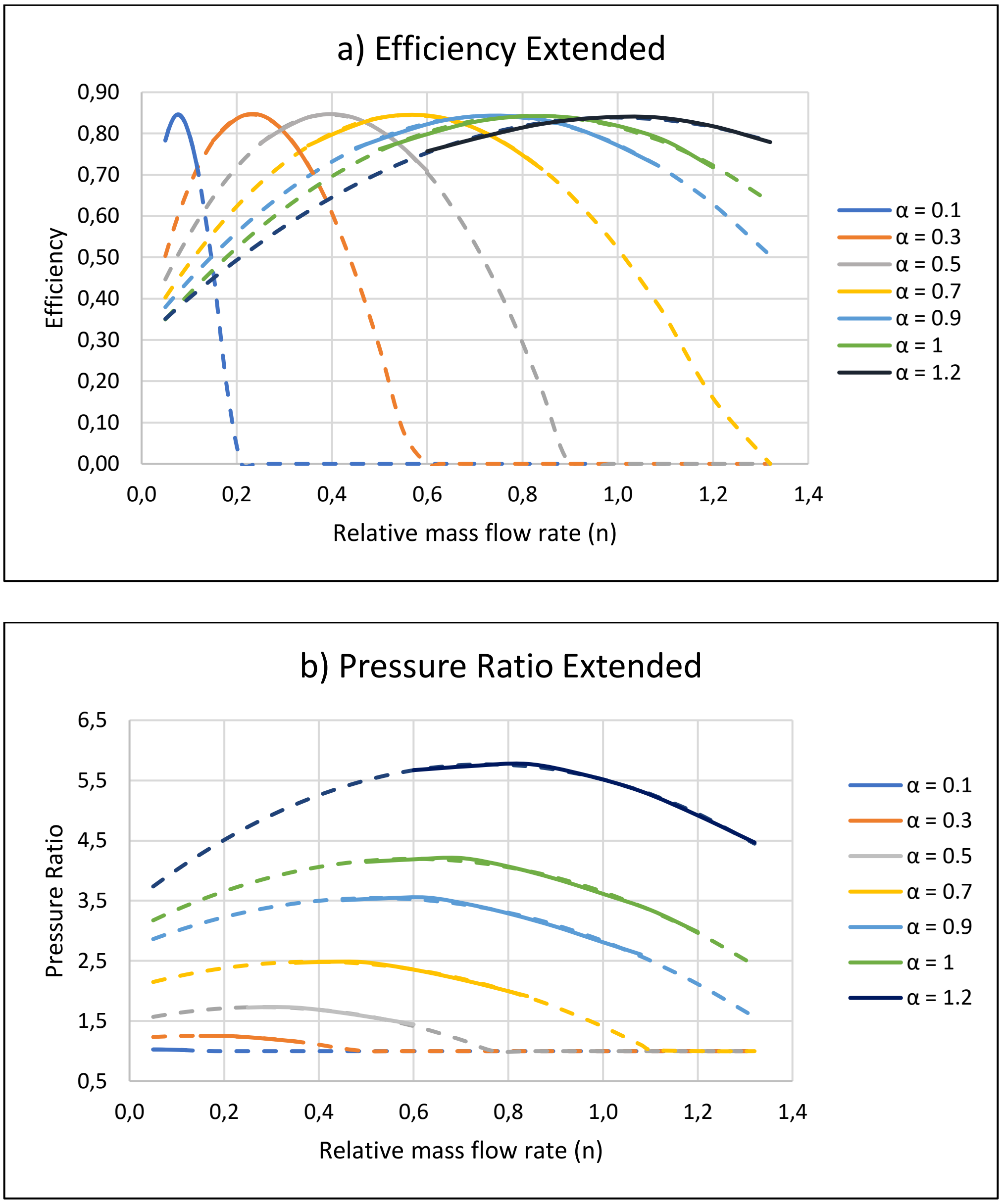

Figure 17 Extended compressor a) efficiency and b) pressure ratio curves

Modelica after the computation of the inlet thermodynamic properties, depending whether the system is supplied with mass flow rate or pressure head, is able to compute the one unknown, the efficiency and the outlet enthalpy. The component will compute the outlet isentropic enthalpy through the function *Medium.isentropicEnthalpy*, requiring the inlet entropy and outlet pressure as inputs.

2.1.1.1.2. Turbine

Comillas planned to use the same procedure mentioned in the compressor section for the turbine sizing, but, for the moment, this task has not been tackled yet; therefore, no indication was received regarding the turbine. To solve this inconvenient without using an ideal model with fixed efficiency, a new semi-realistic model has been built almost from scratch, with the aim to create a device operating similarly as the ideal turbine used by Comillas, but closer to reality.

Component definition

Also in this case, the starting point was a turbine example found in ThermoPower, in the Brayton power cycle example, working with air as medium.

The component, as the ThermoPower compressor, is avolumic and without inertia, working almost in the same way, just using the definitions proper of the turbine for pressure ratio and efficiency (2), again using a-dimensional performance maps, based on the beta-lines method.

This time, the component has been firstly kept with its own performance tables and equations, set with the inlet conditions of interest for the sCO_2 cycle taken from the reference: $N = 3000\ rpm$ and $T_{des,in} = 490\ °C$.

Afterwards, the component has been tested with different mass flow rates and velocities, keeping the outlet pressure fixed at 85.8 bar. Pressure ratio and efficiency values have been extracted to build performance maps, function of speed and mass flow rate. Surprisingly, the pressure ratio resulted to be independent of the speed and linearly proportional to the mass flow rate. This is a considerable approximation and could be considered a model weakness. Although, in absence of better alternatives, it was deemed an acceptable option, until Comillas University will design the real turbomachine.

In Figure 18 the efficiency and pressure ratio curves so obtained are reported, function of the mass flow [kg/s] and rotational speed [rad/s].

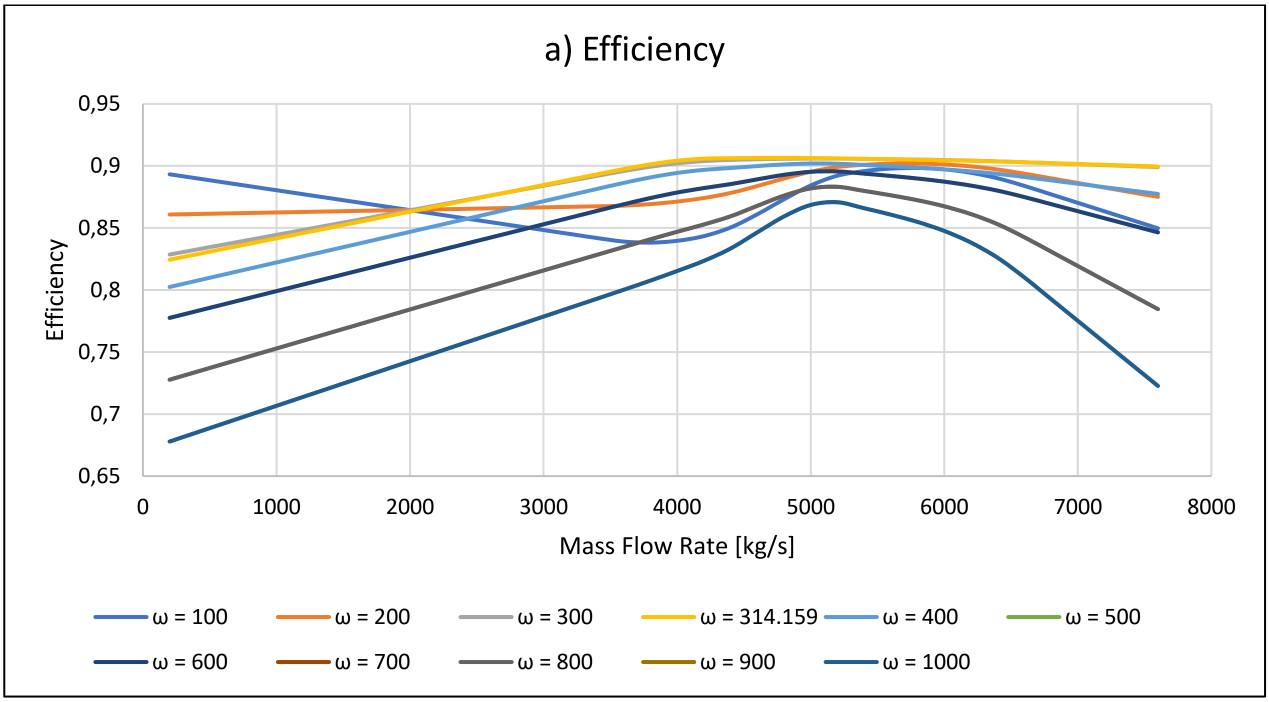

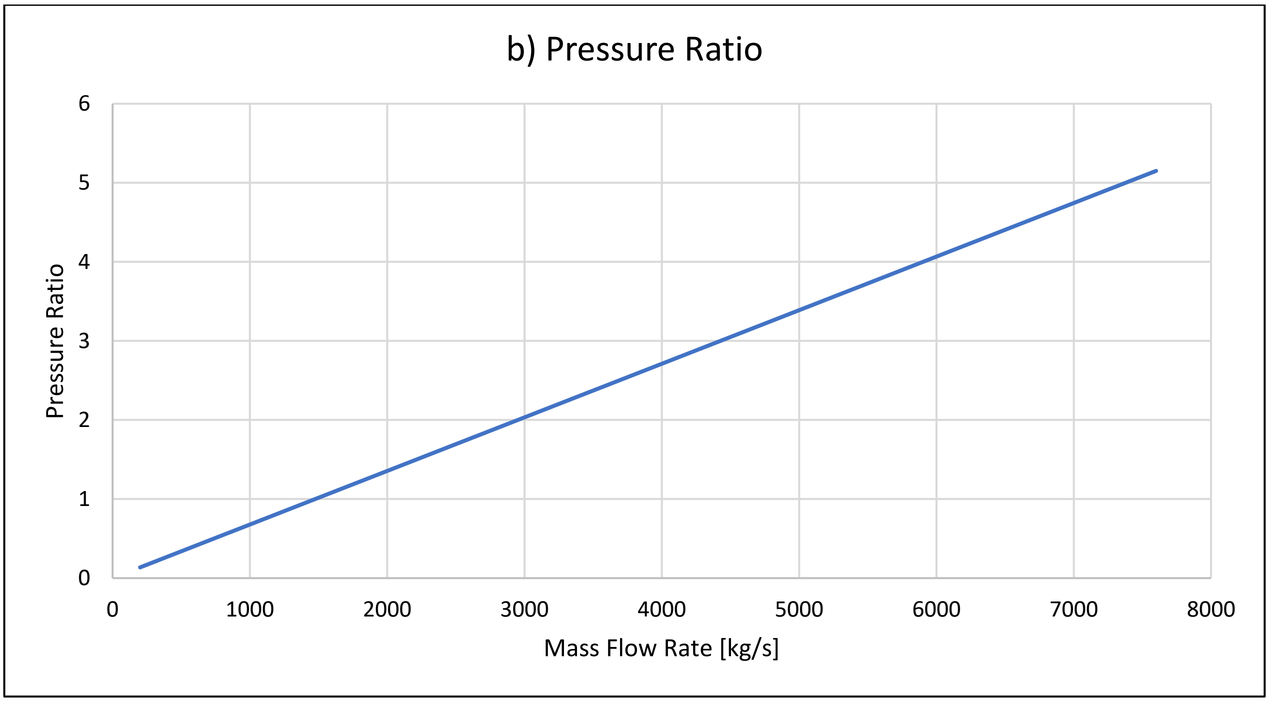

Figure 18 Turbine a) efficiency and b) pressure ratio curves of the ThermoPower turbine model tested with the reference inlet conditions

Since the goal is the design of a component operating similarly to the reference ideal turbine, this should have the same performances at the reference's conditions. In particular, the turbine should be able to provide $PR_d = \frac{300}{85.8} = 3.4965$ and to operate with efficiency $\eta_d = 93\%$, considering the following conditions:

- Inlet: $T = 490\ °C$ $P = 300\ bar$
- Outlet: $T = 343.8\ °C$ $P = 85.8\ bar$

While, it can be observed that, rotating at 3000 rpm (314.159 rad/s) with 6912 kg/s of CO_2 flowing, the turbomachine results in $PR = 4.6843$ and $\eta = 0.9061$. Clearly, the PR value is considerably greater than the one searched, while the efficiency is not high enough.

Hence, the solution to tackle the problem was found in the manipulation of the maps, to create a new component able to address the tasks required. Adapting the model to the sought conditions, it means certainly taking the distance from the reality, but anyway, the device will operate with a well-proven base. This, joined with the PR independency of the rotational speed, justifies the definition of the model as "semi-realistic".

After having been fed with the modified values of pressure ratio and efficiency, the device is now able to operate with the same performances as the reference at nominal conditions. Figure 19 shows the original and final PR curve, represented by Equation (9), which will be provided to the turbine model for the pressure ratio computation.

$$PR = 5.0586E - 4 \cdot \dot{m} \tag{9}$$

Figure 20 contains the final efficiency curves of the compressor. The manipulation strategy is reported in Appendix B, while the performances tables, containing the numeric values before and after the modifications, are available in Appendix C.

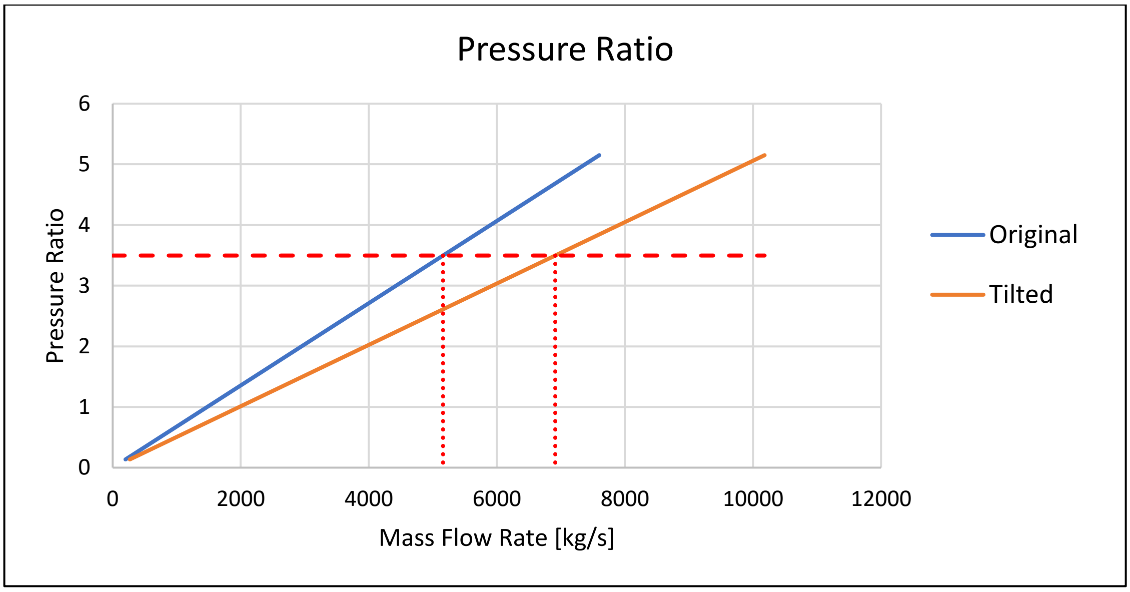

Figure 19 Modified turbine pressure ratio curve. Note: the red dashed line represents the wanted PR, while the red dotted lines indicate the mass flow rates values that provide that PR value before and after the manipulation

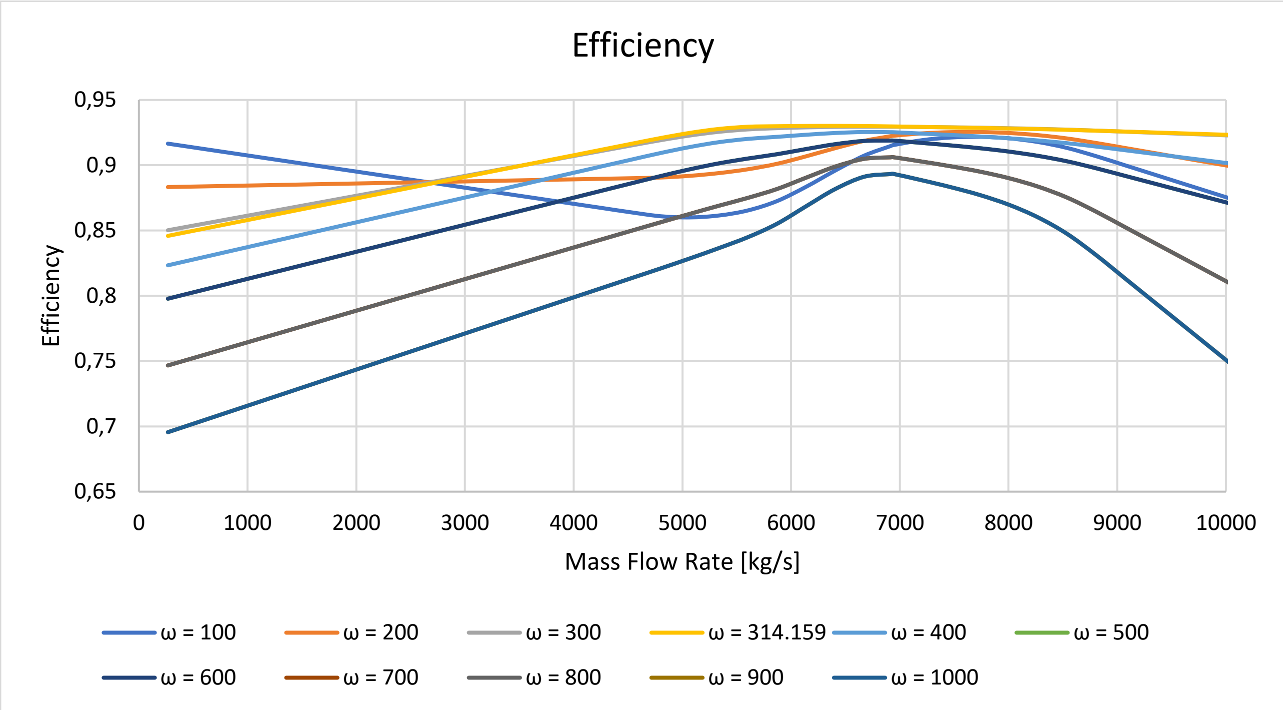

Figure 20 Modified turbine efficiency map

As expected, the turbine operates with the best performance when rotating at 314.159 rad/s, originally set as nominal speed. Moreover, from the graph it is possible to notice the almost flat efficiency behaviour from 5000 kg/s up to over 10000 kg/s, therefore it is predictable that the turbine will operate with almost constant and maximum efficiency for a wide range of mass flow rates in the loop, when running with the nominal speed.

Lastly, the turbine model code required an adaptation in order to read the efficiency and pressure ratio values obtained in the present procedure: the efficiency curves are organized in a 2D table, function of mass flow rate and rotational speed, while the pressure ratio is simply given as a linear equation function of the mass flow (9).Therefore, as done for the compressor, the flow number *Phic* definition and the original a-dimensional performance maps have been removed, with all the annexed variables, substituted by the linear equation for the pressure ratio and the 2D efficiency table, provided as text file. Depending on the given variables, whether mass flow or pressure head, the component will compute the other unknown through the PR equation, followed by the efficiency evaluation and the consequent outlet enthalpy estimation.

As the compressor does, the turbine computes the isentropic enthalpy by means of the function *Medium.isentropicEnthalpy*. Finally, the turbine power output is evaluated with Equation (10).

$$Power = \dot{m}\,(h_{out} - h_{in}) \cdot \eta_{mech} = \tau \cdot \omega \qquad (10)$$

Similarly to Equation (8), η_{mech} is the component's mechanical efficiency, assumed equal to 0.98.

2.1.1.2 Printed Circuit Heat Exchangers

PCHEs have been chosen to operate the thermal exchange, thanks to their applicability with high efficiencies at a wide range of temperatures and pressure. Each heat exchanger is composed of multiple parallel modules, with 96000 semi-circular micro channels organized in 0.6 m x 0.6 m frontal area and variable length.

Due to the presence of thousands parallel semi-circular channels, the 1D modelling of a PCHE is not trivial and requires some simplifications. In the following section the approach pursued, correlations used and the final layout of the three heat exchangers working in the loop will be presented.

2.1.1.2.1 Modelling strategy

Many types of PCHE are currently available on the market, distinguished by the layout and shape of channels, and consequently the type of flow, such as: parallel or cross flow, with straight or wavy channels. Since the reference cycle didn't give any specifications about the type of PCHE, the first assumption was the decision to consider them in the easiest layout, with straight channels and parallel counter flow, as represented in Figure 21.

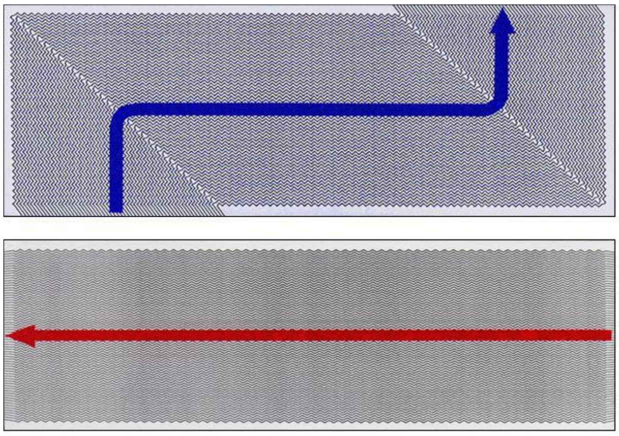

Figure 21 PCHE counterflow layout example with cross-flow inlet (Southall and Dewson, 2010)

Thus, the strategy was firstly aiming at the design of one single PCHE module, to be then multiplied by the number of modules in parallel in each exchanger. Considering parallel straight channels, it is possible to identify 48000 couples of cold-hot micro channels, surrounded by a certain portion of stainless steel. This can be considered a further sub-element of each module, since this layout is the same for each channel-couple, and core of the modelling strategy. Therefore, each heat exchanger will be simulated as a micro-channel couple, multiplied by 48000 and by the number of modules in parallel.

The size of this element was given by Comillas, reflecting the manufacturing technical data of Heatric. The frontal area is 2.5 mm x 3 mm, while the microchannel has a radius of 1 mm, as shown in Figure 22.

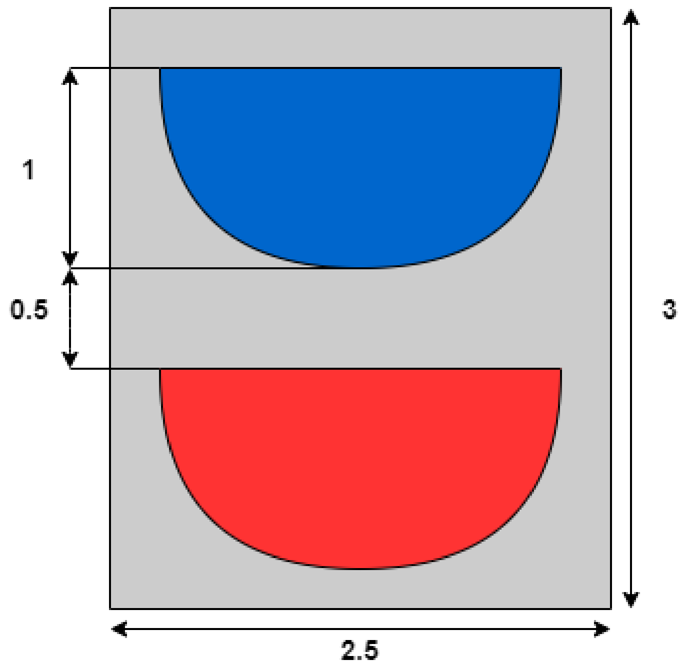

Figure 22 Heat exchanger element's geometric data with lengths in mm

Also here, the ThermoPower library gave a consistent contribute, since the heat exchanger element was fully built with its components, after having adapted them for the desired uses. The components used are:

- Two water pipes (Water bi-phase pipe *'ThermoPower.Water.Flow1DFV2ph'*, since the supercritical carbon dioxide is defined as bi-phase medium), designed with the same geometric characteristics of the microchannels and adapted for the CO_2 flow. The component includes the conservation equations of mass, momentum and energy, considering uniform pressure distribution along the pipe. The flowing fluid can exchange heat towards the radial direction, through a heat transfer model that regulates the thermal power exchanged with the tube wall, while the longitudinal diffusion of heat is neglected. Moreover, the velocity is considered uniform in the cross section. Regarding the computation of friction losses, several methods can be chosen, such as Darcy-Weisbach or Colebrook.

- One metal wall (‘*ThermoPower.Thermal.MetalWallFV’)*, to provide the heat conduction between one pipe to the other, through the Fourier law, and to simulate the thermal resistance, with the heat capacity lumped in the centre of the wall.
- One counter flow element (‘*ThermoPower.Thermal.CounterCurrentFV)*, which was used to simulate the counter flow of the hot and cold fluids, by simply putting the first node of a pipe in communication with the last of the other, and so on.

All these components are using the Finite Volume Method as discretization methodology, for the systems of partial differential equations they contain.

Starting from the micro channels design, since the ThermoPower pipes are circular, it has not been possible to perfectly reproduce the semi-circular shape, but the geometric parameters have been set in order to simulate that as well as possible, nominally the cross sectional area $A = \frac{\pi r^2}{2}$ and the perimeter $P = 2r + \pi r$, corresponding to the perimeter of the heat transfer, being the channel exchanging power in every direction.

Therefore, the hydraulic diameter of the micro channels was computed and attributed to the pipes: $D_{hyd} = \frac{4A}{P} = \frac{4 \cdot \left(\frac{\pi r^2}{2}\right)}{2r+\pi r} = \frac{2\pi r}{2+\pi} = 1.222\ mm.$

Every channel will exchange heat in the two cross directions, therefore the actual thermal interaction is not limited between a channel couple and influenced by the surrounding elements. But, since this condition is symmetric, shared by all the channels; to reproduce the heat exchange it can be assumed that each pipe is just transferring heat with its correspondent in the sub-element, therefore considering adiabatic boundary conditions around the channel-couple element. Now, all the metal present in the element will be involved in the heat conduction between the two channels only, working as thermal resistance.

Thus, it is possible to re-think the element to simulate the heat transfer: the pipes are opened and stretched in a flat surface without thickness, and in between them, the metal mass is condensed in a rectangular shape, with one dimension as big as a channel perimeter P, while its other dimension δ is computed based on the effective metal surface in the cross section (Figure 23). According to the provided dimensions, it is possible to obtain $A_{metal} = (2.5 * 3) - \frac{\pi r^2}{2} * 2 = 4.3584\ mm^2$ and $\delta = \frac{A_{metal}}{P} = 0.84767\ mm$. The three elements (two pipes and metal wall) share the same length.

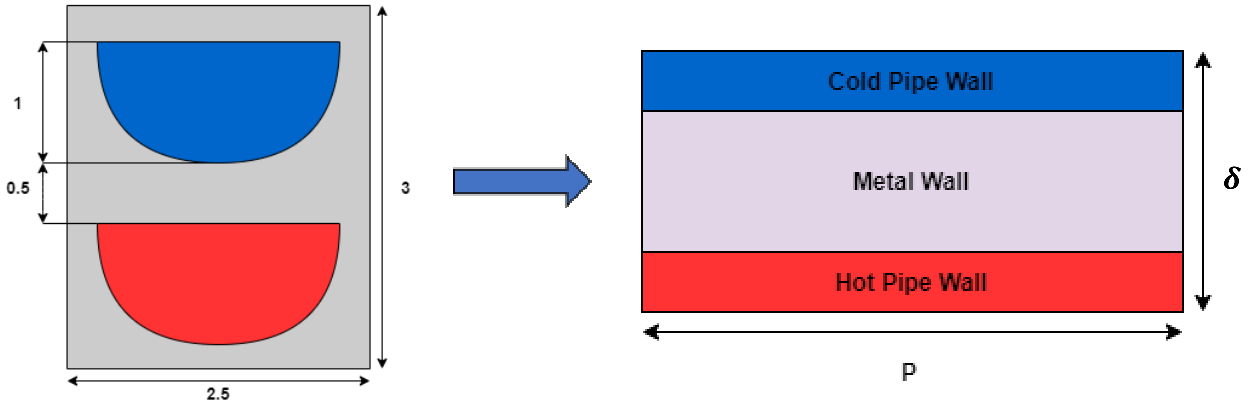

Figure 23 Re-arrangment of the microchannel couple element

Finally, the metal material should be decided in order to set its conductivity and specific heat capacity. From literature, it appears that the most common material used for PCHE is stainless steel of the series 300, in particular 316L, even though many materials are suitable for this purpose (Southall and Dewson, 2010). The material properties found (AZoM, 2004) are: $k = 16.3\frac{W}{mK}$ and $c = 0.5\frac{kj}{kgK}$, where k is the thermal conductivity and c is the specific heat. In reality, the thermal properties are not constant with the temperature, but for simplicity, here they have been considered fixed.

The metal wall component is now provided with all the data needed to characterize its thermal resistance and to compute the Fourier law. In Figure 24 the final configuration of the heat exchanger sub-element just described is shown.

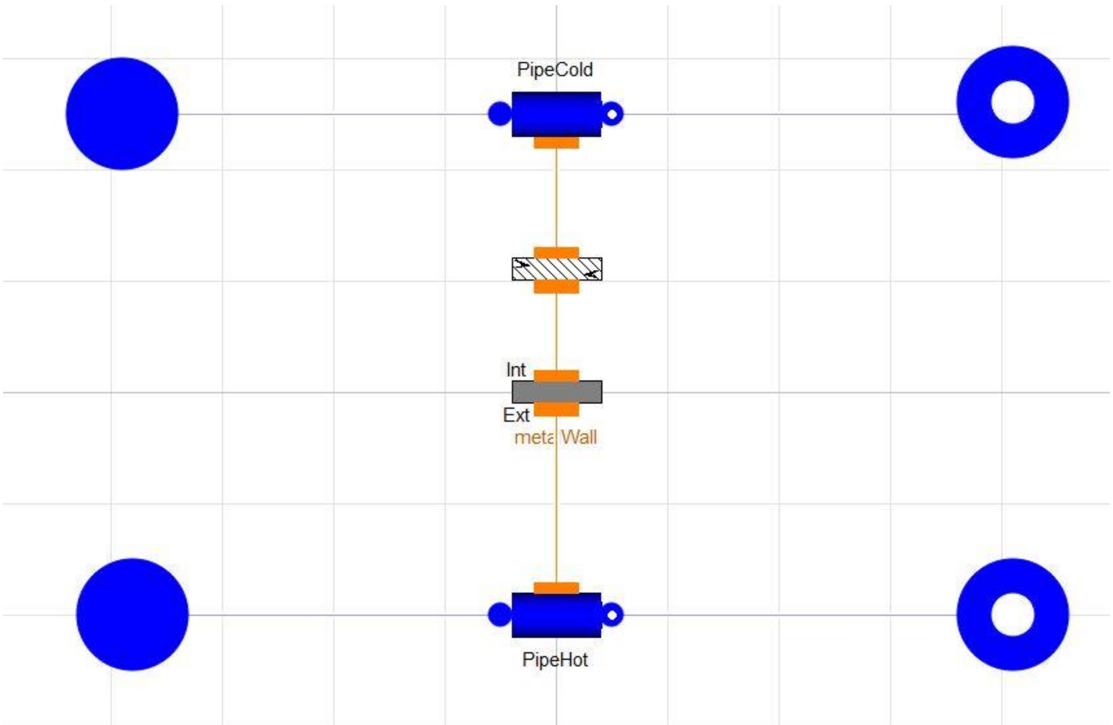

Figure 24 Heat exchanger sub-element configuration

The pipes’ code should be now modified in order to compute the heat transfer coefficients and friction factors, depending on the operative fluid they contain. Therefore, they have been upgraded and added with functions for the evaluation of the a-dimensional numbers typical of the thermo fluid dynamics (Re, Pr, Nu, f), that will be explained in detail in the following section.

Once obtained this configuration working, it is possible to provide Modelica with N_t, the number of pipes in parallel, and, therefore, simulate the heat exchanger module. In more detail, N_t will act on the mass flow, dividing the pipe inlet flow by N_t, while the actual number of pipes will remain as two. Multiplying N_t also by the number of modules in parallel, will simulate the entire heat exchanger.

The sizing procedure for PCHEs has already been explained and performed by Comillas University (Section 2), therefore the characteristics of each heat exchanger, in terms of length and number of modules in parallel and series are already given. It was mentioned that the layout was to be decided formed by 3 parallel sets of 3 the heat exchangers, for space reasons, but, thanks to the parallel configuration, just one exchanger for each type will be modelled, by simply multiplying the number of parallel modules present in the exchanger by three. Table 3 resumes their configuration:

Table 3 Heat exchangers' configuration

	HTR	HTS	PC
Length	0.955	1.391	0.662
Modules in parallel	216	216	144
Modules in series	2	3	1

These values have been used to set the pipes’ length and the number of sub-elements organized in parallel for each exchanger, following Equations (11) and (12).

$$Pipes' \ length = Length \ exchanger \cdot Modules \ in \ series \quad (11)$$

$$Number \ of \ parallel \ sub \ elements = 48000 \cdot Modules \ in \ parallel \quad (12)$$

2.1.1.2.2 Constitutive relations

Depending on the fluid flowing in the heat exchanger, empirical correlations should be used to predict the magnitude of heat transfer and pressure drop. Many studies on heat transfer and friction losses in PCHEs have been performed in the past years, motivated by the growing interest that these exchangers are stimulating. The heat transfer coefficient is generally obtained through the a-dimensional Nusselt number, Nu, being defined as (13).

$$Nu = \frac{h \cdot D_{hyd}}{k} \tag{13}$$

With D_{hyd} hydraulic diameter, *k* thermal conductivity and *h* heat transfer coefficient. The computation of *Nu* is conferred to empirical correlations, widely available in literature. On the other hand, the friction is evaluated with the Darcy-Weisbach formulation (14).

$$\Delta P = f_D \frac{\rho}{2} \frac{L}{D_{hyd}} v^2 \tag{14}$$

Where f_D is the Darcy friction factor, ρ density, L length of the pipe, and v^2 the square of the fluid velocity. Also in this case, through empirical correlations it is possible to compute the friction factor and obtain the pressure drop.

The considerations here reported are valid for turbulent conditions, while in case of laminar flow, fixed values of *f* and *Nu* (Incropera and DeWitt, 2002) are generally considered: $Nu = 4.36$ and $f = \frac{64}{Re}$. The correlations presented will be computed in the pipes through functions created ad hoc.

Carbon Dioxide

Regarding CO_2, different examples of proposed correlations have been found in literature, but the one from Chai and Tassou was taken as reference (Chai and Tassou, 2019). They investigated a 3D numerical model of a PCHE recuperator, with straight channels, located in a supercritical CO_2 Brayton cycle. The goal was the evaluation of its thermohydraulic performances to be compared with several empirical correlations. From the results it appears that Gnielinski (Gnielinski, 1976), Equation (15), is the equation that better fits the experimental results, giving errors lower than 20% for the cold side and 2% for the hot one.

$$Nu = \frac{\left(\frac{f}{8}\right)(Re - 1000) \cdot Pr}{1 + 12.7 * \left(\frac{f}{8}\right)^{\frac{1}{2}} \left(PR^{\frac{2}{3}} - 1\right)} \tag{15}$$

With *f* computed with Blasius formulation (16).

$$f = \frac{0.3164}{Re^{0.25}} \tag{16}$$

Where *Nu* is the Nusselt number, *Re* is the Reynolds number and *Pr* the Prandtl number, computed as (17) and (18).

$$Re = \frac{\rho\, D_{hyd} v}{\mu} \tag{17}$$

$$Pr = \frac{\mu\, c_p}{k} \tag{18}$$

With μ dynamic viscosity, ρ density, D_{hyd}hydraulic diameter, v the velocity, $c_p$specific heat and k thermal conductivity. The Nusselt number will be further used to calculate the convective heat transfer coefficient h (19).

$$h = \frac{Nu \cdot k}{D_{hyd}} \;\left[\frac{W}{m^2 K}\right] \tag{19}$$

The pressure drop model was decided to be different than the one used by Comillas, since another study has been found in literature, considered more precise (Chu et al., 2017); the authors performed an experimental investigation specifically on pressure drops of supercritical CO_2 in pipes, achieving a new formulation for the friction factor (20). Comparing it with the most used empirical correlations, it was proven to be the most precise formulation, with an average error around 2%.

$$\begin{cases} f = \dfrac{64}{Re} & Re < 2300 \\ f = 0.06539\, e^{\left(-\left(\frac{Re-3516}{1248}\right)^2\right)} & 2300 \le Re \le 3400 \\ \dfrac{1}{\sqrt{f}} = -2.34 \cdot \log\left(\dfrac{\epsilon}{1.72d} - \dfrac{9.26}{Re} \cdot \log\left(\left(\dfrac{\epsilon}{29.36 D_{hyd}}\right)^{0.95} + \left(\dfrac{18.35}{Re}\right)^{1.108}\right)\right) & Re > 3400 \end{cases} \tag{20}$$

ϵ is the pipe roughness, set to 1E-5, according to Comillas. Even if the correlation used is different from one used in the reference cycle, the results obtained are very similar, as it will be shown in the next chapters.

Water and Molten Salt

For the water side, the paper from Chu was used as guideline (Chu et al., 2017), where the authors proposed a new Nusselt number equation for water flowing in a PCHE with straight channels, as results of an experimental analysis.

Comparing their results with the well-known correlation from Gnielinski, they aimed to reach a new empirical formulation that could reduce the error: In particular, the equation proposed is a correction of the Dittus-Boelter equation (21).

$$Nu = 0.122\, Re^{0.56}\, Pr^{0.14} \tag{21}$$

With f defined by Equation (22).

$$f = (1.12 \ln(Re) + 0.85)^{-2} \quad (22)$$

Finally, regarding the molten salt, scarce material is available in literature, and it was decided to follow the documentation from Ariu (Ariu, 2014), where he used the Gnielinski correlation in PCHE with molten salt flowing.

It is important to highlight that regarding the pressure loss model for water and molten salt, a simplified strategy was followed: since the main interest of the study is the CO_2 loop, friction losses of the other two fluids have not been computed in detail inside the pipes, but lumped at the heat exchanger extreme, computed through a local pressure drop component taken from ThermoPower, which can operate with different options. The one chosen is the 'Operative point' friction type. With it, the block will compute the friction factor, based on the nominal operative point, given under form of pipe diameter, and nominal pressure drop, mass flow rate and density. Those values were taken from the reference cycle, assumed to be correct.

The reason of this choice was to lighten the computational cost, since the evaluation of pressure drop along the pipe is one of the most expensive steps in these terms and can be considered acceptable. However, the pipes from ThermoPower operate with uniform pressure, therefore the more detailed pressure drop evaluation in each node does not improve considerably the heat exchange anyway.

2.1.1.2.3 Local pressure drops

Until now, the heat exchanger model includes only the micro channels and the alloy in between them, but actually other components are participating: collectors, manifolds and distributions pipes. These elements are source of pressure losses; indeed, the expansion and contraction of flow, when passing across two elements with different sections, cause an ulterior pressure drop. Examining the heat exchanger's structure, it is possible to identify these components at inlet and outlet, and eventually also between the modules in series (for HTR and HTS). Comillas provided detailed layouts of HXs, with most of the technical information about these elements mentioned above, present in Appendix D (Figure D. 1). While for the missings, they were assumed in accordance with UPC. In Figure 25 it is shown an example of HTR configuration hot side:

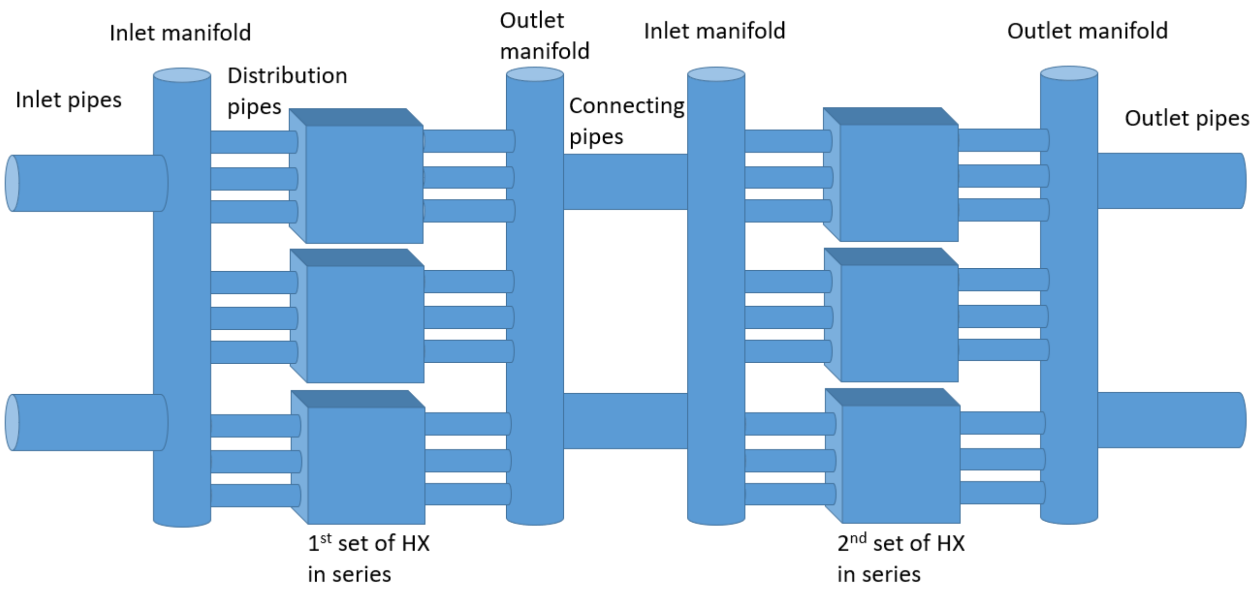

Figure 25 HTR hot side sketch

In Appendix D (Table D. 1) all the elements with their respective sizes for every heat exchanger will be summarized.

The pressure losses in these elements are mainly due to the flow in different pipes (inlet, distribution, connecting, outlet) and local flow expansions/contractions of the flow. To take them into account the following strategy was considered:

- According to the table in appendix, for each heat exchanger, an inlet, outlet, and eventually inter set of pipes, volumes and local pressure drops was built. Inlet and outlet pipes consist of half-length of the pipes connecting the exchanger with the previous/subsequent component of the loop, therefore, the pressure losses correlated to those long pipes will be evaluated here, and not in the actual pipes present in the loop. Above an inlet set example for the HTR hot side is shown in Figure 26.

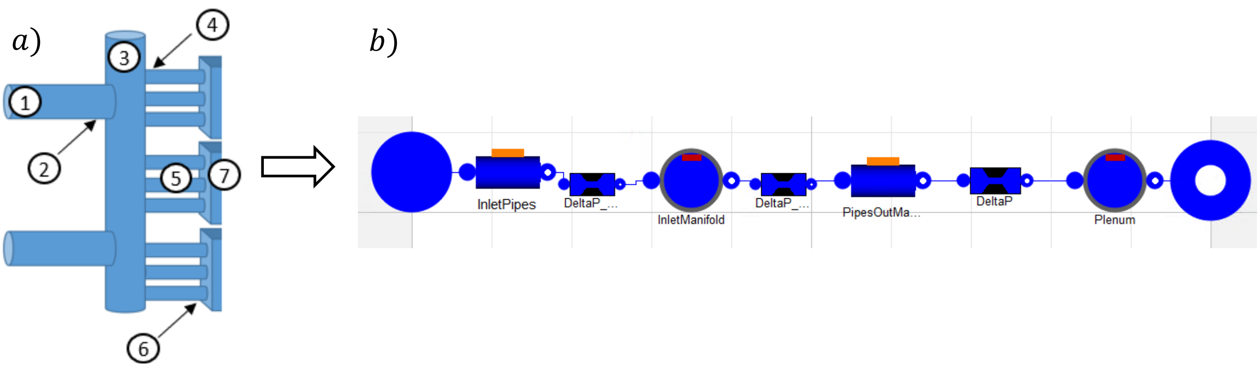

Figure 26 Inlet set for HTR hot side. a) graphical representation provided by Comillas and its b) Dymola model

In order:

1. Pipes at the HX inlet, connecting it with the previous component (considering half of its length).
2. Localized pressure drop to simulate the expansion in the following volume.
3. Manifold, modelled as a volume, from where the distribution pipes will carry the flow to the different PCHE's modules organized in parallel.
4. Localized pressure drop to simulate the contraction in the following pipe.
5. Distribution pipes.
6. Localized pressure drop, to simulate the expansion of the flow in the plenum just before the PCHE module.
7. Plenum, simulated as a volume, that will distribute the flow in the micro channels.

According to Çengel's book (Çengel and Cimbala, 2006), local pressure drops can be calculated with Equation (23).

$$\Delta P = \frac{1}{2}\, K\, \rho v^2 \qquad (23)$$

With K local friction coefficient, that can be approximated as $K = 0.5$ in contractions and $K = 1$ in expansions, with sharp edges for turbulent flow.

On the other hand, friction in pipes is computed using the Colebrook equation (24), with roughness $\epsilon = 1E - 5$, following the indications of Comillas University.

$$\frac{1}{\sqrt{f}} - 2\log\left[\frac{\epsilon}{3.7 D_{hyd}} + \frac{2.51}{Re\,\sqrt{f}}\right] \qquad (24)$$

- Initially, all these sets were included in the heat exchanger model but were causing convergence problems. Therefore, each set has been tested with nominal pressure and mass flow of Comillas' cycle, considering also the head losses consequent of the flow in the HX modules for the inter and outlet sets.
- Afterwards, each heat exchanger was provided with two pressure loss blocks at its inlet. Since these components require the value of diameter, because of the huge size difference between big pipes, it was decided to put two of them, as inlet, outlet and connecting pipes, and the distribution pipes. Therefore, one of the blocks will simulate the head loss in big pipes, while the second will account for the distribution pipes. They will be operating with the 'Operating

point' option, so it will compute the local friction factor based on the nominal operative point, setting as nominal pressure drop the sum of the relative pressure losses computed in the previous step, the diameter as average of pipes' diameter, 6912 kg/s nominal mass flow (having tested the sets with it) and nominal density computed at the prescribed conditions.

2.1.1.2.4 Heat exchanger complete module

Adding these last elements to the base HX, the final heat exchanger configuration is reached, shown in Figure 27. Even though more realistic than the initial version, the pressure loss model explained here is still an approximation of the reality that could be further improved in future models.

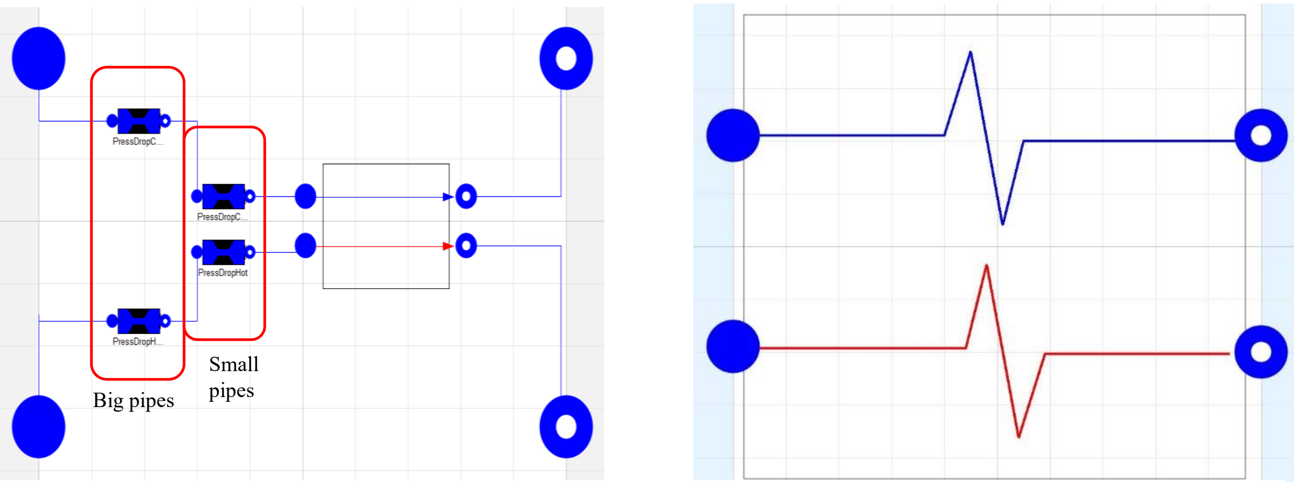

Figure 27 Internal (left) and external (right) view of the HTR final configuration

In the next sections a brief resume of the features for each HX will be summarized, presenting also the grid independence study performed for the determination of the minimum number of nodes required in each one of them.

2.1.1.2.5 High Temperature Recuperator

The HTR is the component that characterises the regenerative configuration, key to the improved loop's performance compared to the base non-regenerative layout. Indeed, it is the HX that exchange the biggest amount of power, pre-heating the compressed fluid with the one exiting the turbine, and, therefore, avoiding to claim that power from the heat source.

Composed by 2 modules in series 0.955m long and 216 modules in parallel, the recuperator operates with high-pressure low-temperature CO_2 one the cold side and low-pressure high-temperature CO_2 on the hot side.

For the determination of the minimum number of nodes needed, the component has been tested considering uniform pipes' temperature, set respectively as the inlet temperature of hot and cold side obtained by Comillas, with number of nodes varying from 20 to 30. In every case, the steady state was reached before 12.5 seconds.

The results on both cold and hot side at 12.5 seconds were collected for every number of nodes and benchmarked: the needed number of nodes was reached, when the relative difference between two subsequent values was smaller than the tolerance, set at 1E-4 (Figure 28). This procedure led to the choice of 26 nodes. Generally, the cold side was reaching the steady state earlier than the hot side, and could need a lower number of nodes, but to interact with the metal wall and the hot pipe, the same nodes number was required, therefore, it was given the value obtained by the hot side.

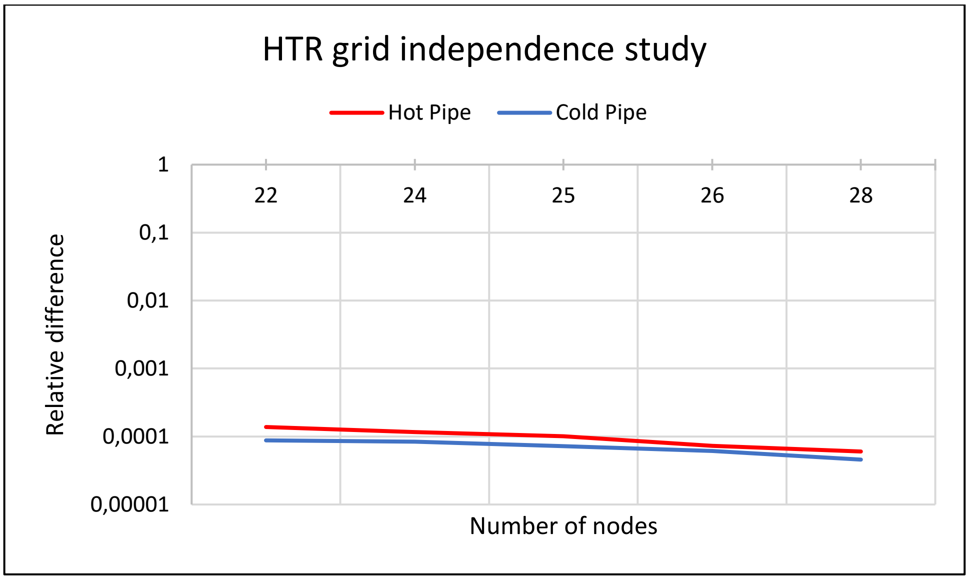

Figure 28 HTR grid independence study

2.1.1.2.6 High Temperature Salt Heat Exchanger

Heat source of the entire loop, this heat exchanger promotes the heat transfer between the pre-heated high-pressure carbon dioxide and the high-temperature molten. It is the biggest exchanger with 3 sets of modules in series 1.391m long, with 216 modules in parallel, and centre of the greatest pressure loss, due to its size and the high temperature of the CO_2.

Similarly to the HTR, a convergence study tested the number of nodes from 20 to 40, leading to 25 nodes as minimum value required (Figure 29). The steady state was reached always before 25 seconds, therefore, the temperature values have been taken and compared at that time step.

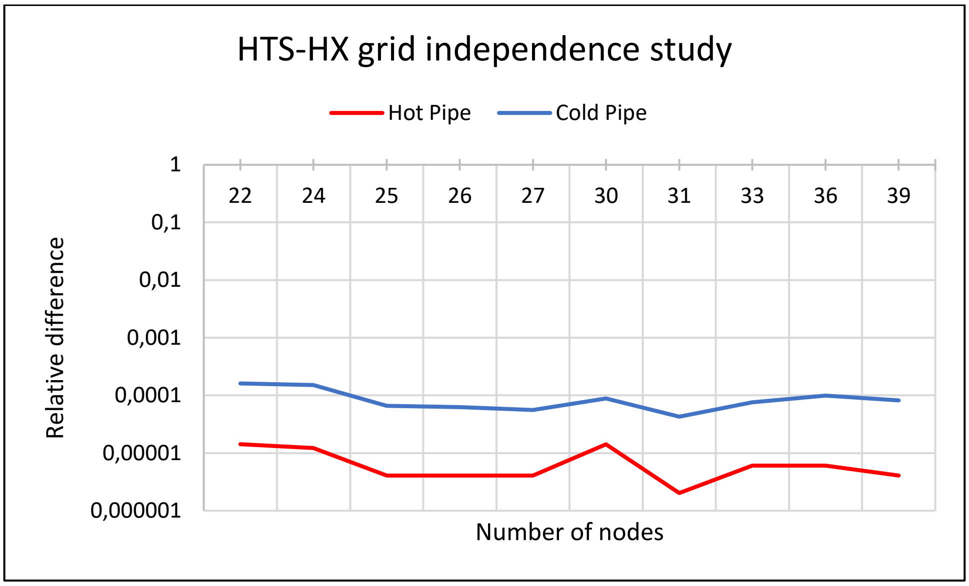

Figure 29 HTS-HX grid independence study

2.1.1.2.7 Pre-Cooler

This last heat exchanger is the heat sink of the cycle, where water at 25 °C and 8 bar refrigerates the carbon dioxide at high-pressure already partly cooled down in the recuperator, to restore the original condition of the fluid before the ingress in the compressor. The smallest between the HXs, just 0.662m long with 144 modules in parallel.

In it, nodes from 7 to 20 have been tested, reaching the steady state always in the first seconds due to the component's small dimensions. The temperature values have been collected at 10 seconds. The convergence study showed that, in spite of the small dimensions, 20 nodes were required to stay under the tolerance (Figure 30).

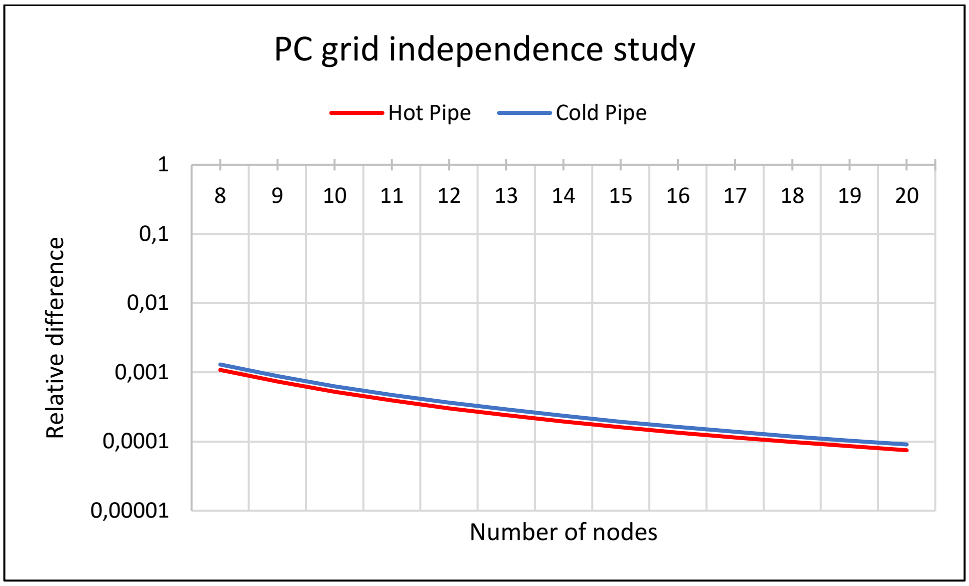

Figure 30 PC grid independence study

To sum up, Table 4 reports the final configuration of the three heat exchangers, comprehensive of the number of nodes.

Table 4 Summary of the heat exchangers' configuration

	HTR	HTS	PC
Length	0.955	1.391	0.662
Modules in parallel	216	216	144
Modules in series	2	3	1
Nodes	28	25	20

2.1.1.3 Minor components

In the following section the components of minor interest, but still present in the loop, presenting their functioning for completeness of the chapter will be described. All the components are already present in the ThermoPower library, re-declaring the fluid which they are working with.

2.1.1.3.1 Mass flow source and pressure sink

Basic components to establish a constant flow at prescribed mass flow rate, temperature and pressure.

The mass flow source imposes a fluid flow at prescribed temperature or enthalpy, while it is kept free to vary in pressure. Moreover, it is possible to provide the values of mass flow rate, temperature (or enthalpy), by an external input, useful to simulate dynamic conditions.

The pressure sink works similarly to the previous item but imposing the pressure, while it doesn't fix temperature and flow values, although it is possible to set a value for temperature or enthalpy. As the previous case, pressure, temperature (or enthalpy) can be supplied by external inputs.

The pair source of mass flow and pressure sink is present in the cycle both on the water and molten salt side, to simulate the respective loops.

2.1.1.3.2 Expansion tank

The expansion tank simulates an ideal expansion vessel, with infinite capacity of releasing or collecting fluid flow, in order to impose a fixed pressure in the point of its location. Therefore, it acts as both a source and a sink of pressure, depending on the pressure conditions at its extremes, so whether it should inject or absorb mass flow. Here it has been used to fix the inlet pressure at 85 bar, filling the system with the correct mass of CO_2 required to have the desired pressure.

2.1.1.3.3 Pipes

As mentioned in the introduction of this chapter, the pipes connecting the different loop's components were initially not accounted for by Comillas, and consequently also in the first ideal case presented here, although they have been sized. Checking the loop scheme (Figure 12), it is possible to see over each line linking two components, three numbers representing: number of parallel pipes x diameter $[mm]$ x length $[m]$. Afterwards, they have been added in the real case, giving the system higher volume and consequent greater inertia and stability against perturbations. As explained in the heat exchanger section (2.1.1.2.3) they are considered without friction, since their pressure losses are already accounted for in the heat exchangers. Moreover, no information was available regarding bends and thickness, therefore they have been considered straight and without thermal inertia.

3 Steady State Operation

As introduced previously, two cases have been developed and tested: the first with the same layout as the reference, to have a first benchmark against Comillas' data and prove the results' validity; this version is not inclusive of connection pipes, supposing every cycle's element connected directly to the next one, hence defined as "Ideal Case". The second keeps the same layout, but comprehensive also of pipes and local pressure losses due to flow expansion or contraction in the HXs elements, resulting in a bigger volume and greater pressure drops than the previous case. The presence of these elements confers bigger reliability to the cycle, therefore defined "Real Case".

Both the cases have been tested with the same boundary conditions of reference:

- Molten salt and water flows are set with fixed conditions, in terms of mass flow rate, and inlet temperature and pressure, summarized in Table 5. Moreover, it has been imposed the same reference pressure drop to the two fluids.

Table 5 Water and molten salt boundary conditions

	Molten Salt	**Water**
$\dot{m}\left[\frac{kg}{s}\right]$	6184.6	29297
$P_{in}\ [°C]$	1.6	8
$T_{in}\ [°C]$	495	25
$\Delta P\ [bar]$	0.6	1

- Compressor and turbine are rotating at the same fixed velocity, even though not co-axial (thus the effect of one would not influence the other), running at grid frequency of 50Hz so with a velocity $N = 3000\ rpm = 314.195\ \frac{rad}{s}$.
- The expansion vessel fixes the pressure at the compressor inlet, in order to have one point of the two cycles with the same pressure $P_{in,comp} = 85\ bar$, ensuring more reliability to the results.

The reference cycle's results will be briefly summarized, followed by the presentation of the two Modelica models' outputs and comparing them with the reference. In Appendix E are provided the thermodynamic values of all the loop sections.

3.1 Reference cycle results

Run with the conditions mentioned above, the power cycle designed by Comillas is able to produce about 800 MW, with a thermal efficiency $\eta_{th} = 39.76\%$. In it, 6912 kg/s of carbon dioxide are flowing, passing from 85 bar and 35°C at the compressor inlet, close to the critical point, to 300 bar and 490°C at the turbine inlet. These are the loop's points with, respectively, the lowest and highest temperature and pressure.

The thermodynamic cycle is represented on T-s and P-V diagrams in Figure 31.

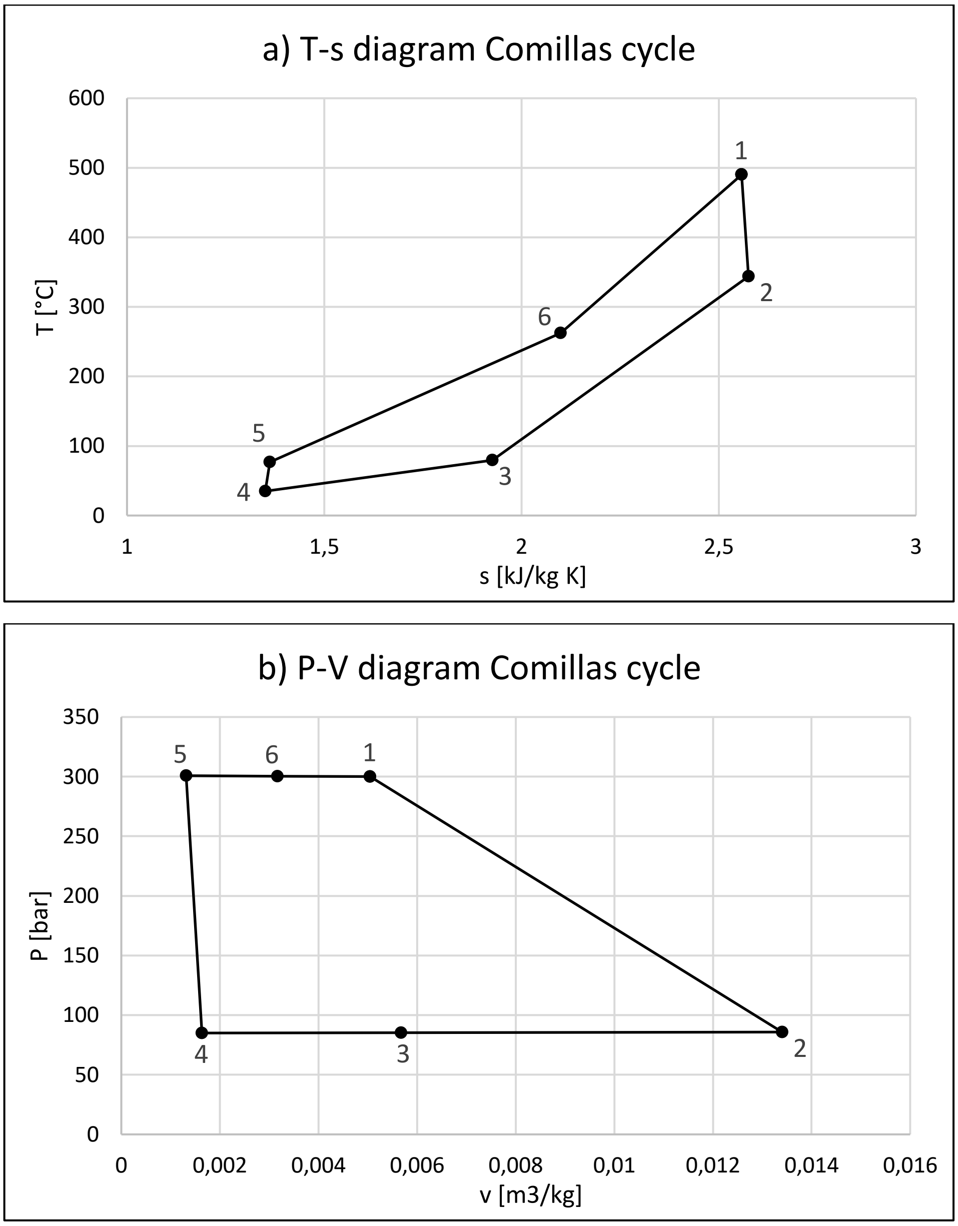

Figure 31 a) T-s and b) P-V diagrams of Comillas cycle

The turbine is producing around 1 GW with an efficiency of 93%, while the compressor has an isentropic efficiency of 88%, absorbing around 0.2 GW. The two components are working with almost the same pressure ratio, thanks to due low pressure drop in the heat exchangers. Indeed, in the whole cycle the pressure loss is slightly higher than 1 bar.

Regarding the heat exchangers, as already mentioned in the system description, the recuperator results to be the device exchanging more power between the three, almost 2.2 GW_{th}, witnessing the relevant improvements that the recuperation can bring to the base configuration. This power is graphically represented in the *T-s* curve by the area below the curves 2-3 or 5-6. The area below the line 6-1 quantifies the specific heat provided to the system, while the one below line 3-4 pictures the one released to the heat sink.

Table 6 summarizes the main reference results.

Table 6 Comillas' results summary

Comillas results summary	
Mass Flow [kg/s]	6912.00
Efficiency	39.77%
Compressor Power [GW]	0.24
Turbine Power [GW]	1.05
HTR Power [GW]	2.18
HTS Power [GW]	2.03
PC Power [GW]	1.22
Total Pressure Drop CO2 [bar]	1.08
Low Pressure Level [bar]	85.00
High Pressure Level [bar]	300.80
Minimum Temperature [°C]	35.00
Maximum Temperature [°C]	490.00

3.2 Ideal case

The ideal case modelled with Modelica has identical configuration and components to the reference, except for the turbomachinery. Therefore, operating at the same conditions and being built with the same layout, similar results are expected.

Although, some discrepancies could arise as consequence of differences in the turbine and compressor; since in the present work, more realistic devices have been used, it is reasonable to suppose and await a slight different behaviour, that could appear in pressure levels and mass flow rate, since the compressor is the element imposing the motion to the flow.

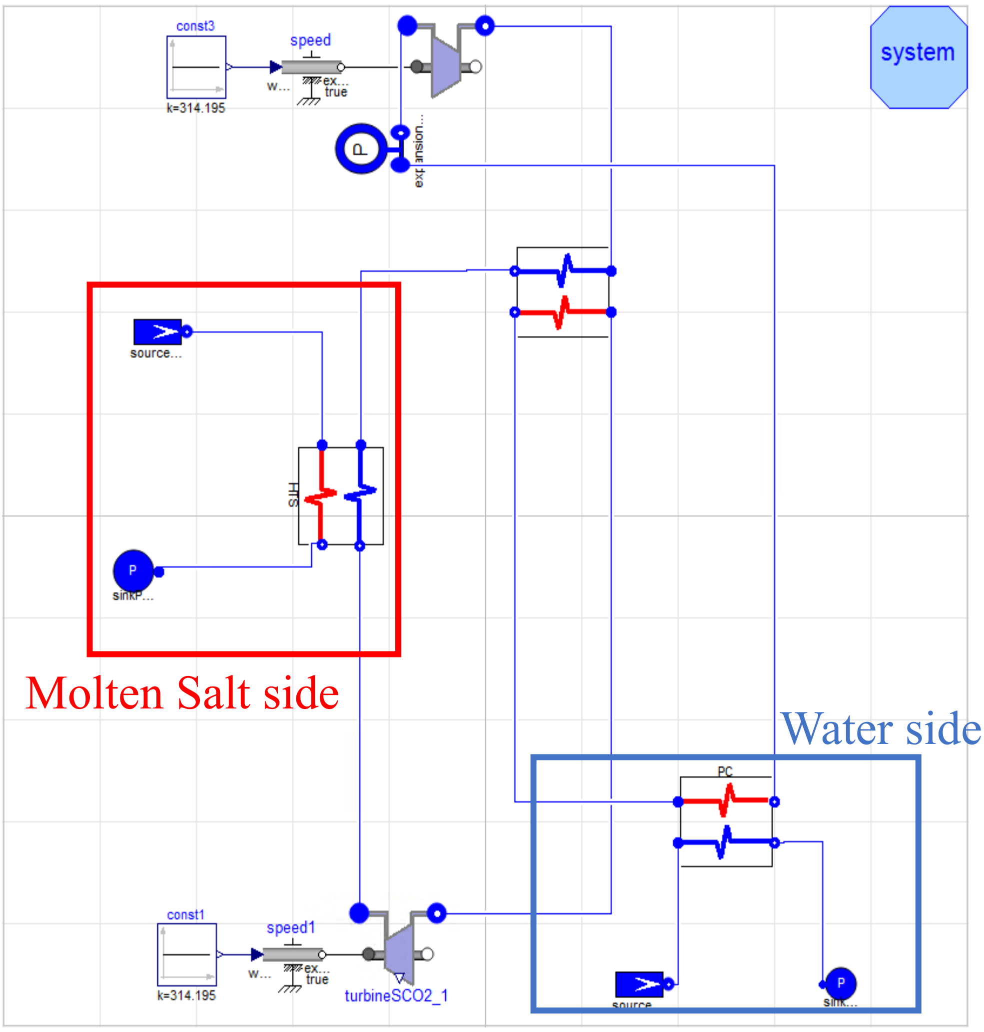

Figure 32 Ideal case layout in Dymola

Figure 32 shows the cycle's layout and aspect in Dymola, highlighting molten salt and water components.

3.2.1 Results and comparison

The loop is producing 770 MW with a global efficiency η_{th} = 37.14%; 7138.9 kg/s of CO_2 are flowing, varying from 35 °C and 85 bar to 488 °C and 310 bar, respectively at compressor and turbine inlet, undergoing 1.15 bar of total pressure drop.

Also in this case, the HTR is the heat exchanger entrusted of the highest thermal power transfer, 2.13 GW_{th}, followed by HTS and PC. Turbine is generating 1.08 GW of power output, working with 92.94% of isentropic efficiency, while the compressor absorbs 0.31 GW, operating with η_{iso} = 76.48%. Moreover, it is important to highlight that the compressor is operating within the performance curves provided by Comillas University, so in a valid operative region, with $\nu = 1.19$ and $\alpha = 1.06$ (Figure 33).

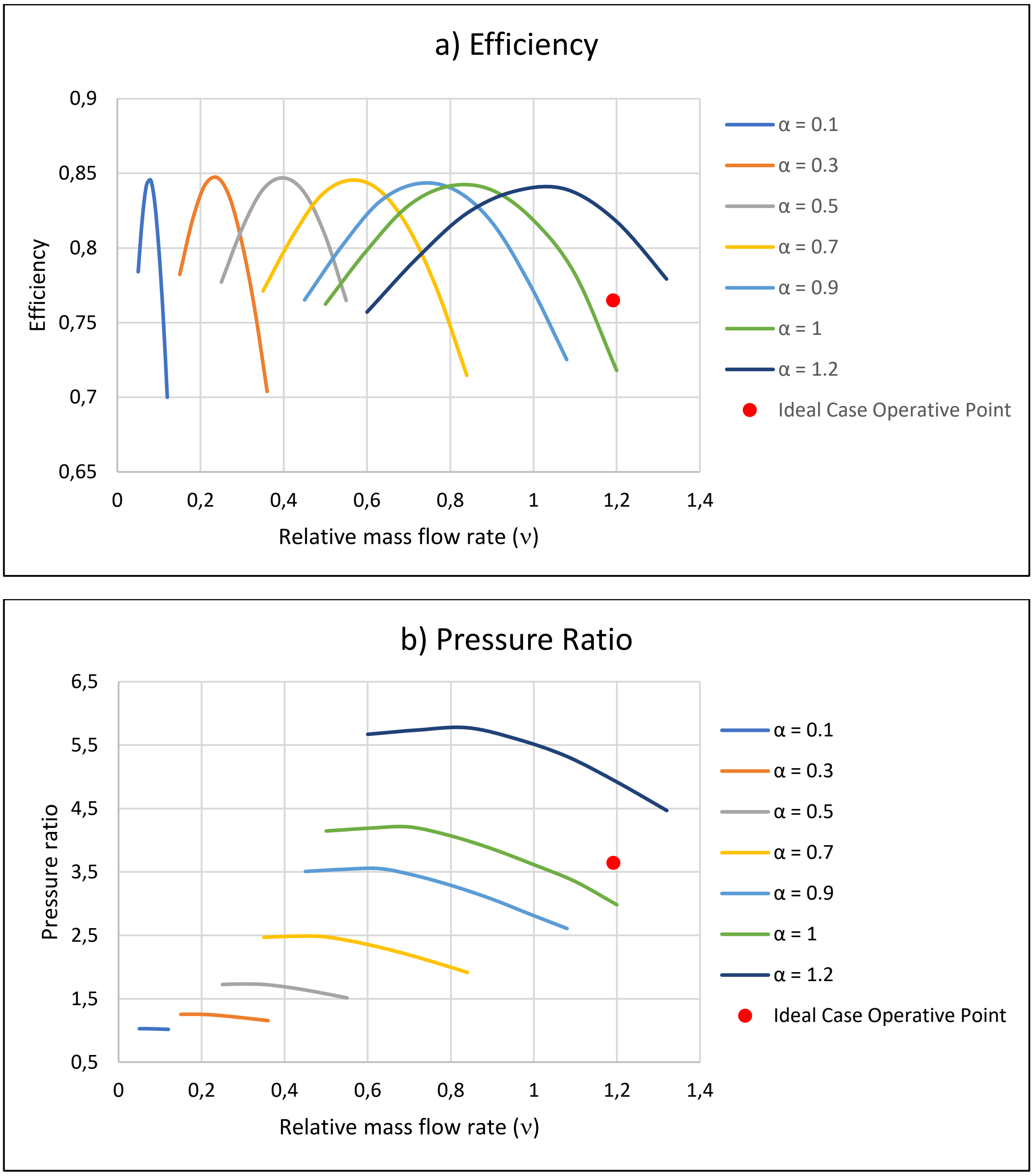

Figure 33 Compressor ideal case operative point representation in a) efficiency and b) pressure ratio maps

In Figure 34 the T-s and P-V thermodynamic diagrams of the cycle (solid line) are represented, compared with the reference cycle (dashed line).

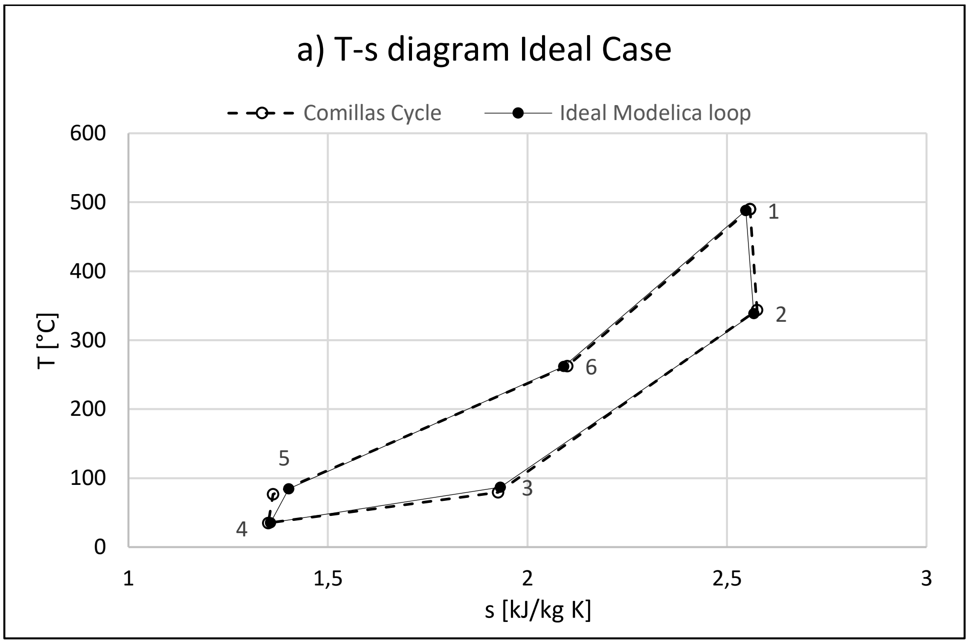

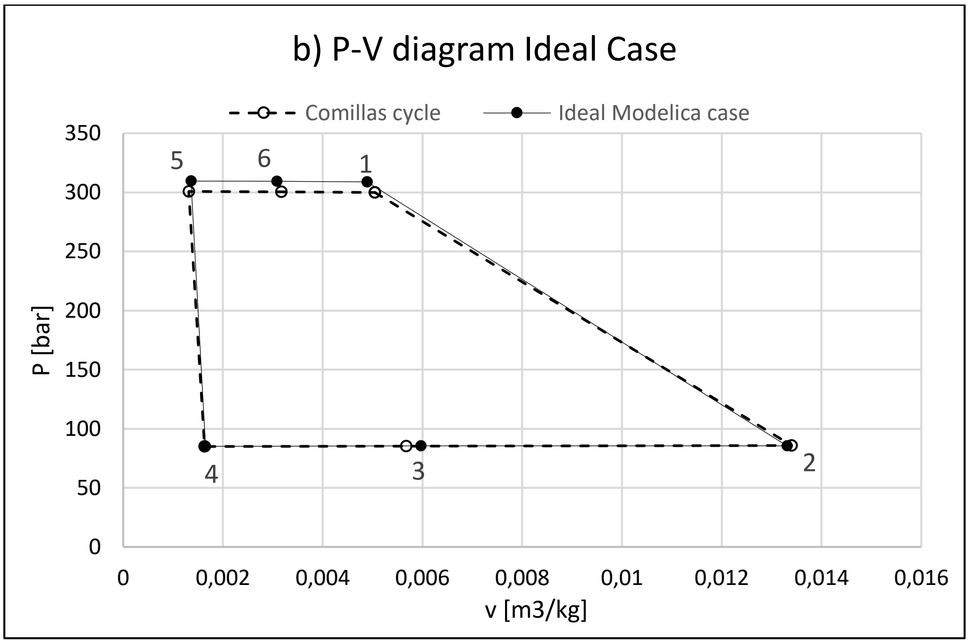

Figure 34 a) T-s and b) P-V Ideal loop diagrams

As expected, discrepancies are present between the cycle modelled with Modelica and the reference, mainly due to the different operation of the turbomachinery components. Indeed, what can be noticed from Figure 34 is that the cycle modelled here is operating at a higher maximum pressure than the reference, almost 10 bar above. Moreover, the 5th point indicating the compressor outlet, results shifted towards more high temperatures, justified by the lower isentropic efficiency at which the compressor is working.

The mass flow rate of CO_2 appears to be 3.28% higher, another difference attributable to the operation of the turbomachinery; as a consequence of this, also the total pressure drop results bigger. The greater mass flow, lower compressor efficiency and higher-pressure level are reflected in an increased power consumption of the device (+27%), which consequently leads to a loss of about 2.5 percentage points in the global cycle efficiency, even though the turbine is extracting more power, being operating almost with the same efficiency as the reference case, higher PR and mass flow. All the heat exchangers are working almost as Comillas devices, especially the pre-cooler. To conclude, the results obtained in the first configuration are very close to Comillas loop, proving the Modelica code to be operating well.

Table 7 resumes the cycle's results and compares them with the reference loop.

Table 7 Ideal case's results summary, compared with the reference values

	Comillas	Modelica	Relative Difference
CO_2 Mass Flow [kg/s]	6912.00	7138.90	**3.28%**
Efficiency	39.77%	37.14%	**-6.91%**
Compressor Power [GW]	0.24	0.31	**27.14%**
Turbine Power [GW]	1.05	1.08	**2.83%**
HTR Power [GW]	2.18	2.13	**-2.12%**
HTS Power [GW]	2.03	2.09	**2.73%**
PC Power [GW]	1.22	1.22	**-0.34%**
Total Pressure Drop CO2 [bar]	1.08	1.15	**6.25%**
Low Pressure Level [bar]	85.00	85.00	**0.00%**
High Pressure Level [bar]	300.80	309.58	**2.92%**
Minimum Temperature [°C]	35.00	35.22	**0.62%**
Maximum Temperature [°C]	490.00	487.97	**-0.41%**

3.3 Real case

As widely explained in the previous chapter, the real case modelled in Modelica, keeps the same layout and boundary conditions as the ideal and the reference. The difference is given by the introduction of the connection pipes between the cycle's components and the inclusion of friction losses in the distribution elements of the PCHEs. Due to this, the results are again expected similar to the previous case, differing for higher pressure drops that will lead to lower mass flow rate.

Figure 35 shows the loop's diagram built in Dymola.

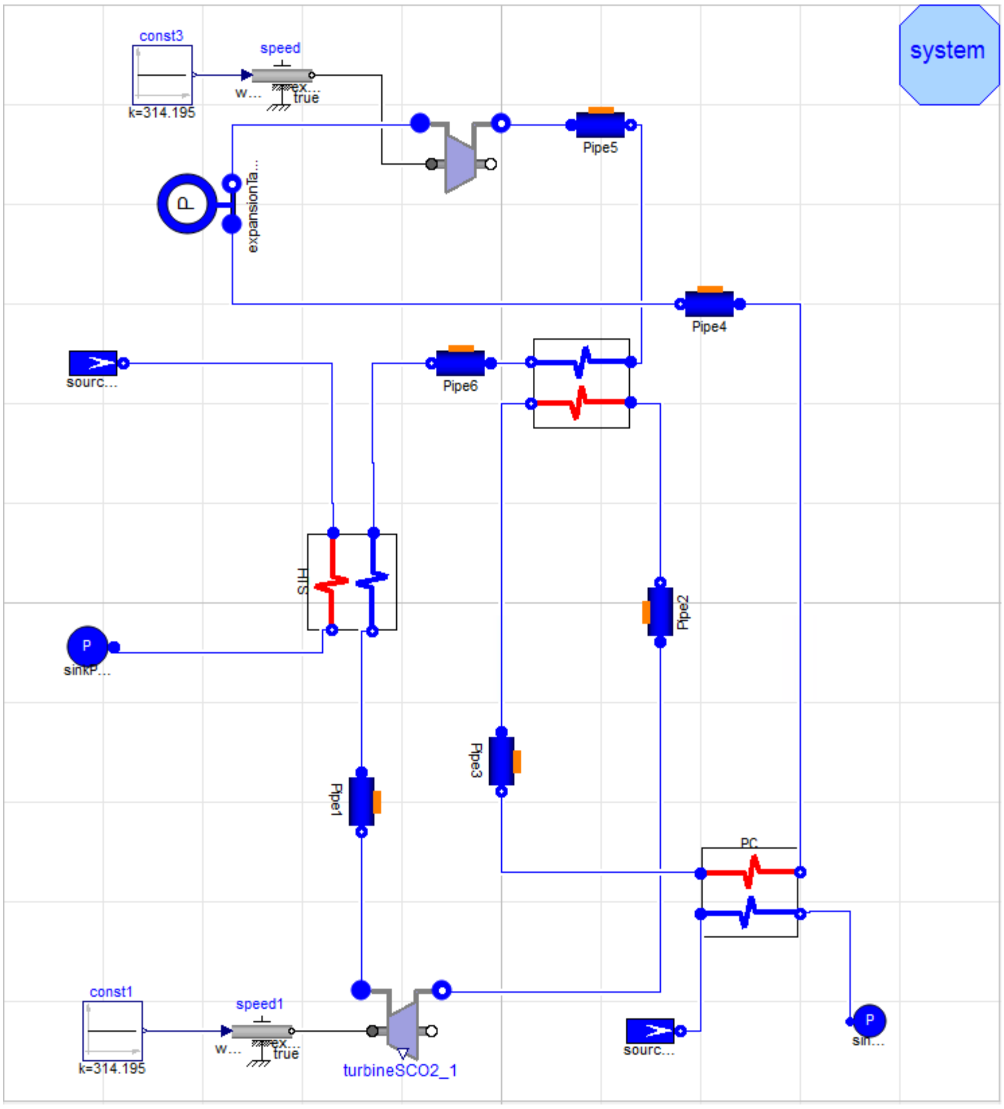

Figure 35 Real case layout in Dymola

3.3.1 Results and comparison

In Figure 36 are presented the T-s and P-V diagrams of the cycle, benchmarked with the reference cycle.

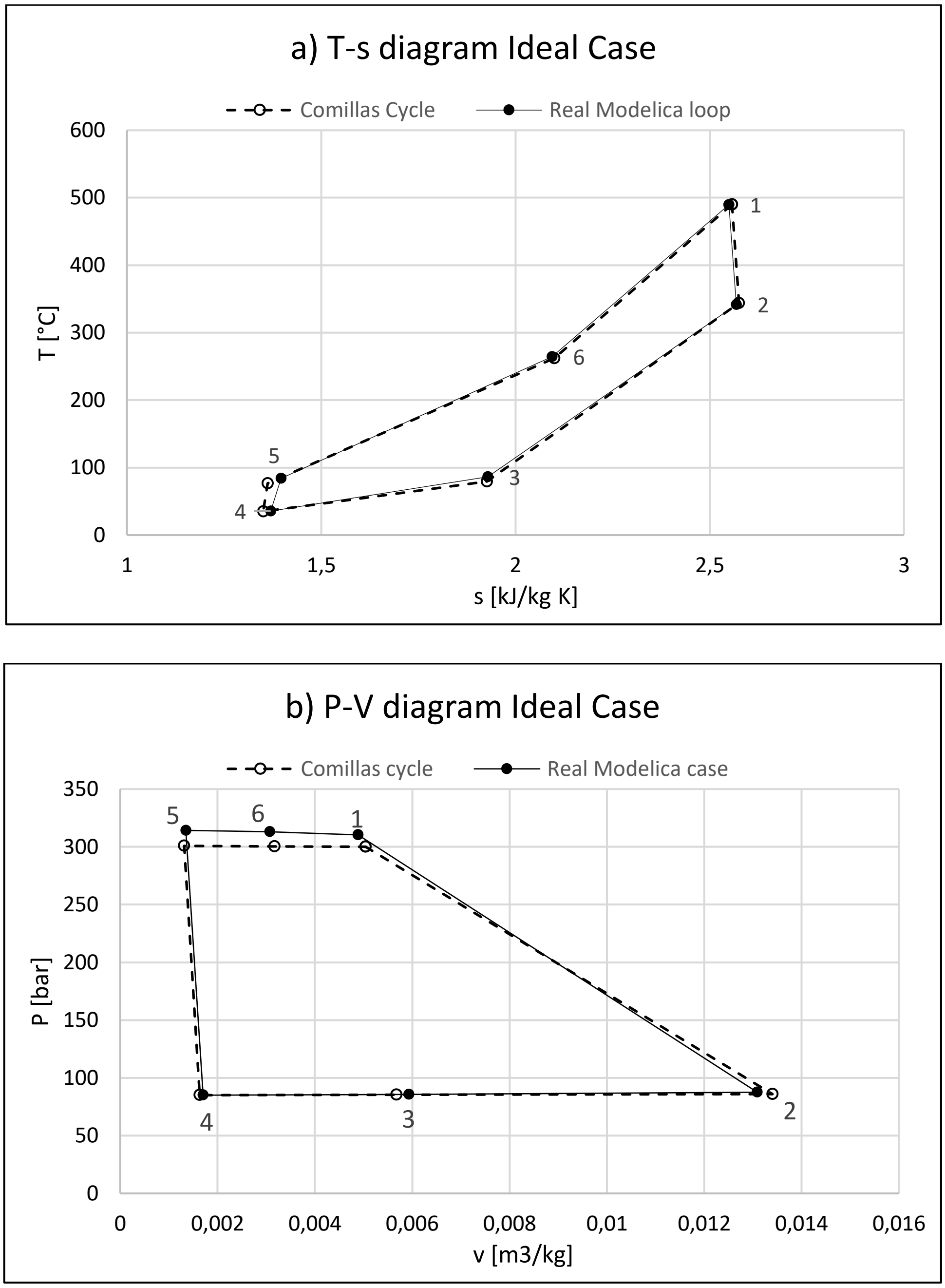

Figure 36 a) T-s and b) P-V diagram of real case, compared with the reference cycle

The presence of the pipes and local pressure drops in HXs led to considerably higher friction losses, around 6.5 bar, almost five times more than the previous case. This is translated in a small loss in the loop efficiency, now at 36.83%, and a reduction of the mass flow to 7008 kg/s, closer to the reference value, only 1.39% bigger. Moreover, the more consistent pressure drop now requires a greater pressure output from the compressor, reaching 314bar. Also the temperature level appears slightly increased, due both to the higher pressure and the reduced mass flow passing through the HXs; indeed, the fluid is now operating between 314 bar and 490 °C, till 85 bar and 35.6 °C. As can be seen from Figure 36.a and from Table 8, the heat exchanger are performing again very similarly to the reference; in this case the HTS is the exchanger with the smallest relative difference in terms of thermal power exchanged.

Also in this case, the compressor is operating inside the performance curves, closer to the nominal conditions, so unitary values of relative mass flow and speed, thanks to the mass flow decrease (Figure 37). In particular, the device now operates with $\nu = 1.15$ and $\alpha = 1.06$, which led to an increase in its isentropic efficiency, reaching 77.9%.

On the other hand, the turbine's efficiency is almost unvaried, stable at 92.94%, thanks to its almost flat efficiency curve when running at 3000 rpm. Both the turbine's and compressor's powers result decreased, nominally 1.05 GW and 0.3 GW, with a more evident reduction in the turbine compared with the first case, leading to a drop also in the net cycle's power output to 750 MW.

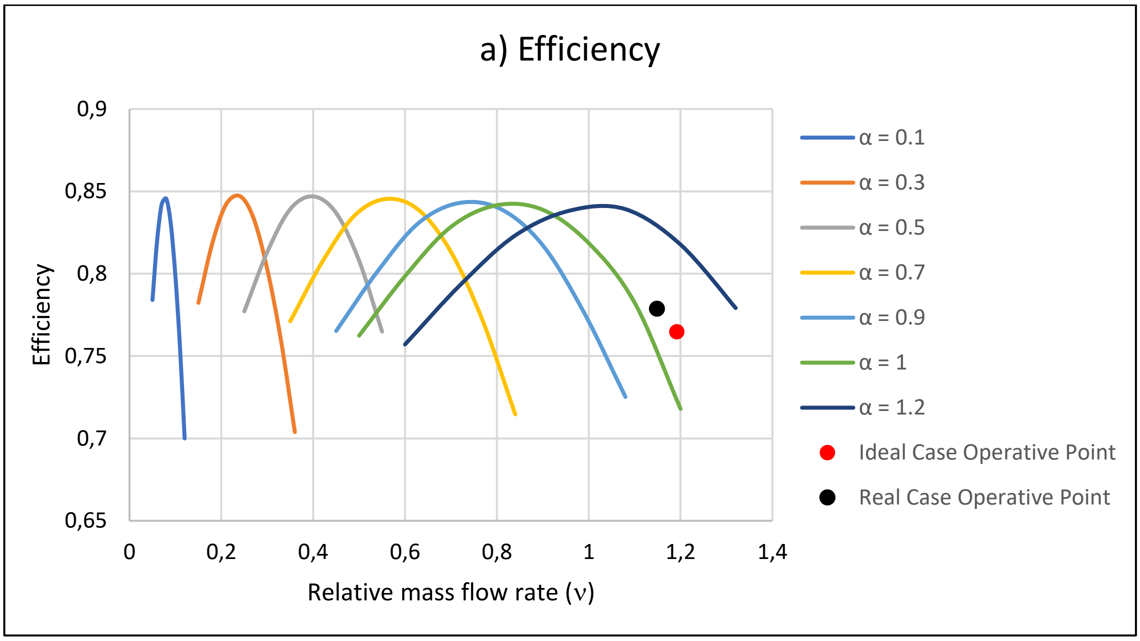

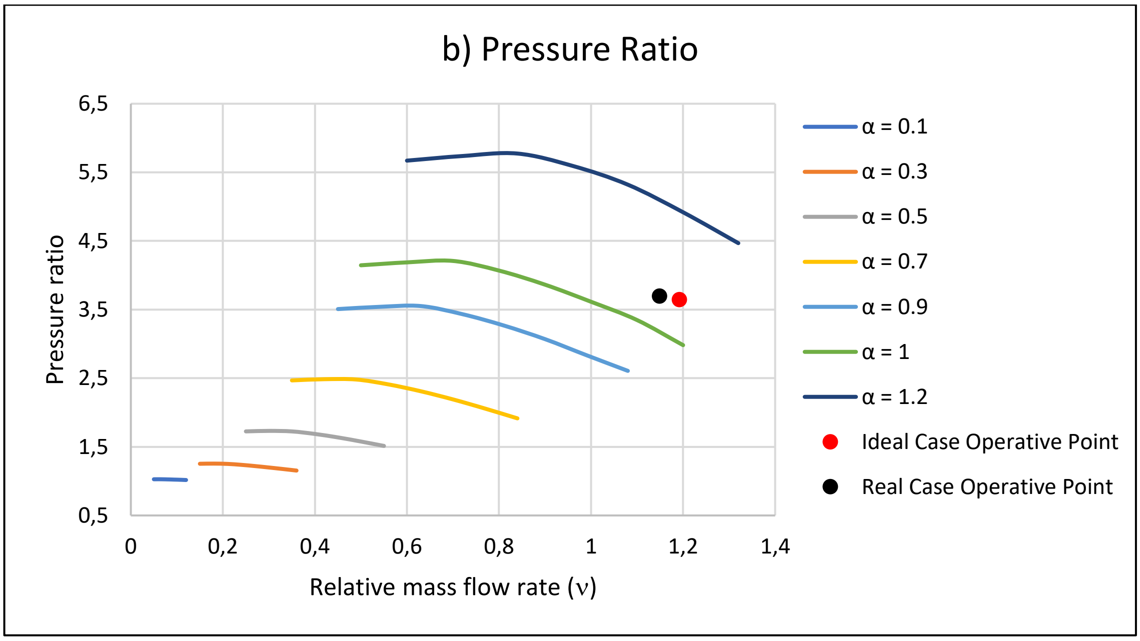

Figure 37 Real case compressor operative point benchmarked with the ideal case, a) efficiency b) pressure ratio maps

The differences with the reference case are mainly the same as the ones with the ideal case, thanks to the closeness of the systems. To conclude, the cycle's results respect the forecasts, presenting differences with the ideal case where expected and showing, anyway, the good functioning of the system, not far from the reference's performances, even introducing those modifications. Table 8 summarized what explained in these lines, reporting results and relative differences with the reference cycle.

Table 8 Real case's results summary, compared with the reference values

	Comillas	Modelica	Relative Difference
CO_2 Mass Flow [kg/s]	6912	7008.32	1.39%
Efficiency	39.90%	36.83%	-7.70%
Compressor Power [GW]	0.24	0.30	24.23%
Turbine Power [GW]	1.05	1.05	0.0014%
HTR Power [GW]	2.18	2.12	-2.54%
HTS Power [GW]	2.03	2.04	0.57%
PC Power [GW]	1.22	1.27	3.95%
Total Pressure Drop CO2 [bar]	1.08	6.48	499.06%
Low Pressure Level [bar]	85.00	85.00	0.00%
High Pressure Level [bar]	300.80	314.24	4.47%
Minimum Temperature [°C]	35.00	35.61	1.74%
Maximum Temperature [°C]	490.00	489.67	-0.07%

4 Dynamic Simulations

The current chapter will demonstrate the results of the dynamic simulations, including the control techniques and the definition of partial load operation strategies of the plant.

The simulations have been performed on the second layout presented in the previous chapter, modified by the inclusion of a valve, located on the pipes after the compressor, which will be used in one of the control strategies. The valve model has been taken from the water section of ThermoPower (*'ThermoPower.Water.ValveVap'*); it is suitable for compressible fluids and based on IEC 534 / ISA S.75 standard for valve sizing and it can be controlled through the opening factor θ, which regulates pressure drop and mass flow across the component. Being acting on the pipes after the compressor (80m far), the valve has been set with the same dimensions; in particular, 12 parallel pipes are present and instead of introducing 12 valves, only one equivalent has been considered. The flow coefficient has been given by the metric Av coefficient, decided with UPC to be set at 1.92 m^2, which causes a pressure drop of 0.16 bar when totally opened. The valve flow characteristic has been considered linear.

The simulations performed led to the integration of 3 PIs, respectively acting on:

- Water mass flow rate, to control the compressor inlet temperature. The controller will be kept active for all the following simulations.
- Molten salt mass flow rate, firstly used to control the Turbine Inlet Temperature (TIT), then used as power control strategy.
- Valve's opening factor, in order to impose an additional pressure drop and consequently regulate the mass flow rate.

Figure 38 shows the loop scheme in Dymola, inclusive of all the controllers.

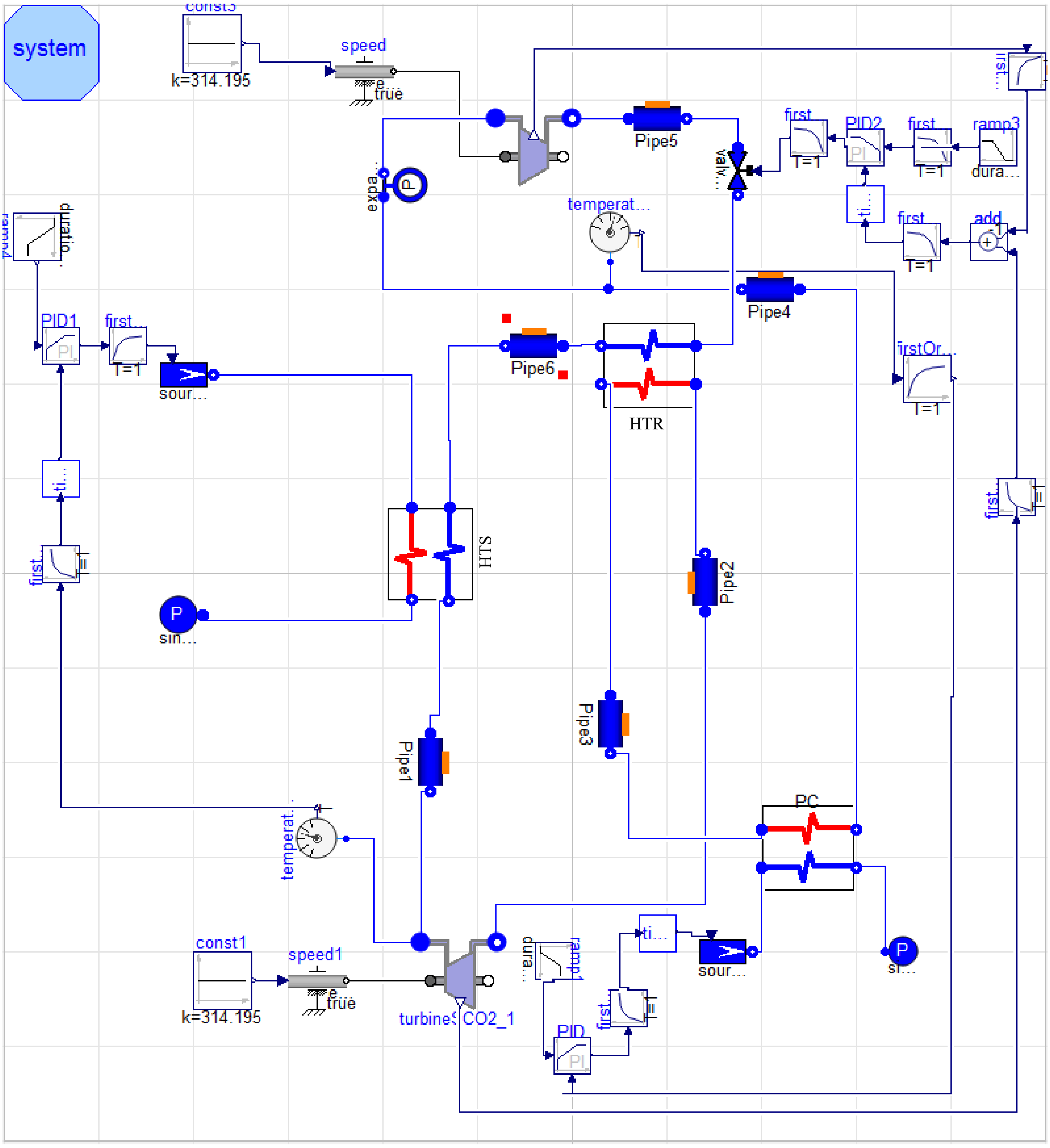

Figure 38 Dymola plant scheme inclusive of the controllers

Thanks to these components it was possible to propose and test two different part-load operation strategies, one acting on the TIT and one on the CO_2 mass flow rate circulating in the loop, comparing the results and finding the most convenient.

The chapter will firstly report a brief description of the PIs controllers and the steps followed for their tuning, together with the dynamic simulations needed in this process. Lastly, the partial strategies will be presented with the respective results, that will be consequently benchmarked to find the optimal one. Appendix E contains the thermodynamic values of all the cycle points.

4.1 PI controllers

The Proportional Integral (PI) control is a simplification of the Proportional Integral Derivative (PID) controller, in which the derivative part is removed. The controller output acts according to Equation (25).

$$u(t) = u_0 + K_c\, e(t) + \frac{K_c}{T_i} \int_0^t e(t)dt \tag{25}$$

The first term u_0 is the controller initial output value, it defines the "bumpless" of the controller's response in case the initial error is zero. K_c is the gain which characterizes the aggressiveness of the answer, while $e(t) = SP - PV$ is the error from the set point, defined as difference between the set point value *SP* and the variable measured, called process variable *PV*. Finally, T_i is the integral time constant that, together with the gain, will establish the weight of the integral term in the equation, which keeps track of the error over the time.

The tuning procedure starts imposing a step variation of the controlled variable, analysing the PV's response, from which the following parameters can be computed. The first is the Process Gain $K_p = \frac{\Delta PV}{\Delta CO}$, measuring the steady state variation of the PV in response to the perturbation imposed, defined as the change of the Controller Output CO.

Afterwards, the Time Constant T_p should be evaluated. This is the time gap between the moment of the initial response of the system and the time when the PV has reached the 63% of its steady state variation: $T_p = Time(0.63\ \Delta PV) - Time\ initial\ response.$

The Dead Time Θ_p evaluates the time elapsing between the perturbation and the first response of the PV, evaluated as $\Theta_p = Time\ initial\ response - Time\ perturbation.$
With this parameters, it is possible to compute the Time Constant of the closed loop T_C, depending on the type of response desired (Table 9).

Table 9 Time constant value depending on the type of response

Type of response	T_C
Aggressive	$\max(0.1 \cdot T_p, 0.8 \cdot \Theta_p)$
Moderate	$\max(1 \cdot T_p, 8 \cdot \Theta_p)$
Conservative	$\max(10 \cdot T_p, 80 \cdot \Theta_p)$

Generally, in the present model the response has been set to be between aggressive and moderate. Finally, it is now possible to calculate the tuning parameters of the controller, using Equations (26) and (27).

$$K_C = \frac{1}{K_p} \cdot \frac{T_p}{\Theta_p + T_C} \tag{26}$$

$$T_i = T_p \tag{27}$$

In all the simulations here presented, the PIs will be activated after the achievement of the steady state in order to avoid unwanted perturbations still present in the system. The controller component has been taken from the Modelica Standard Library (*'LimPID'*), in which is possible to set superior and inferior limits of the controller, setting the derivative term to zero.

4.1.1 Water flow control

The control of the water flow in the pre-cooler was of high interest for the regulation of the compressor inlet temperature, in order to seek the nominal inlet temperature of the device, improving its performances and consequently the whole cycle's efficiency.

As mentioned in the previous section, the PI setting requires a dynamic simulation in which the manipulated variable undergoes a step variation, to evaluate the process variable's response. Thus, a step of -10% was imposed to the water flow in the PC at the 0 seconds mark, obtaining an increment of the compressor inlet temperature of about +0.5 °C (Figure 39).

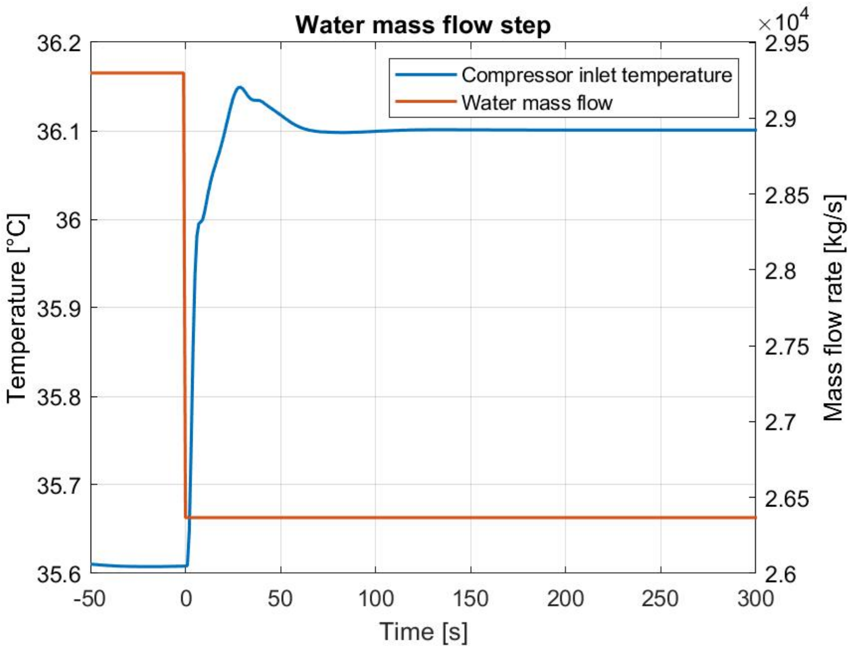

Figure 39 Water mass flow step variation effect

Even if between the precooler and the compressor there is a considerable distance, the effects of the water drop cause an almost immediate variation of the compressor inlet temperature, due to the change of pressure consequent to the higher temperatures in the pre-cooler. This initial variation is then followed by the heat wave after some seconds. Indeed, pressure variation moves with the velocity of sound, while changes in temperature follow the fluid velocity, thus, there will be a delay between the two.

Following the procedure explained before and after some adjustments, the PI can be set with $K_c = -3914.1$ and $Ti = 28.6\ s$.

It is now possible to use the controller, activating it after the steady state, again at time 0 seconds. The set point is firstly set at 35.6 °C, lowered at 35°C at the PI's activation moment in order to limit the integral term of the controller's response. As can be seen from Figure 40, after some initial oscillations, the controller is able to reach the desired compressor inlet temperature in about 200 seconds, with a water mass flow $\dot{m}_{water} = 31657.13\ \frac{kg}{s}$. Being the distance between compressor and pre-cooler not excessively big, the delay between the control action and the system response is short.

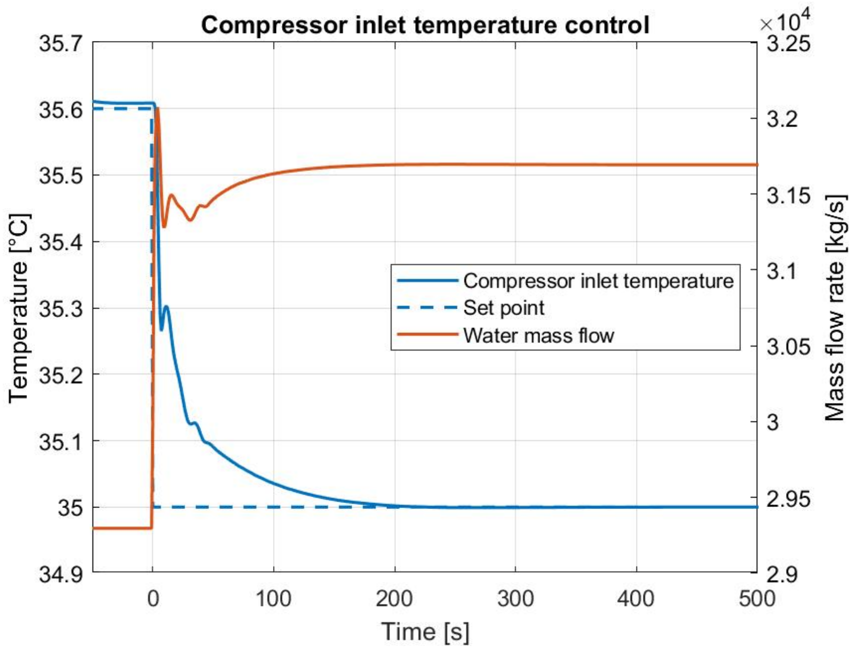

Figure 40 Water PI activation

The compressor inlet thermodynamic conditions are now the same as the reference and the nominal values, therefore, the relative speed α will be now equal to 1. Indeed, from the Figure 41 it is possible to notice that ν is shifted towards unitary values, consequence also of the reduction of mass flow rate elaborated by the compressor, precisely 6835 kg/s. Moreover, the smaller mass flow causes a decrease in the pressure drop, 4% smaller than before the control. This shift of relative parameters will make the compressor working with improved performances, increasing its efficiency up to $\eta_{iso} = 81.05\%$.

As a result of the efficiency improvement, the enthalpy of the fluid exiting the compressor will be closer to the isentropic value, reflected in a lower temperature. Indeed, the outlet compressor temperature results decreased to 78.8 °C, with a difference between inlet and outlet that is now 43.8 °C, while before was 48.6 °C. On the other hand, the PR results reduced and with it the high-pressure level (Figure 42.b).

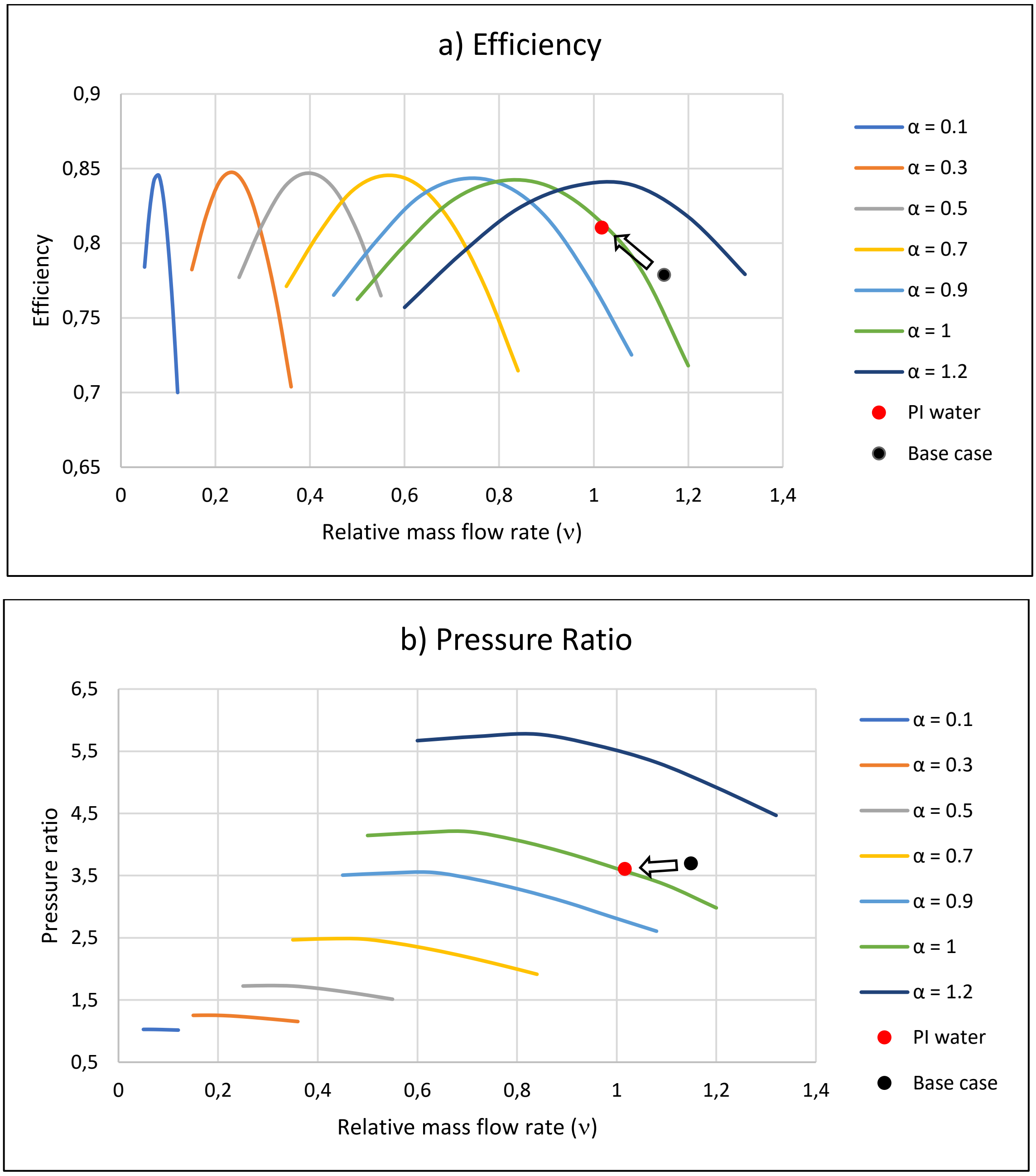

Figure 41 Compressor performances after the water PI's action, on a) efficiency and b) PR curves

The lower mass flow allows the HTR to perform a better heat recover, as it possible to notice for the *T-s* diagram (Figure 42.a), where the area below the lines 5-6 and 2-3 represents the specific heat exchanged in the recuperator. Moreover, thanks to this is also possible to reach a higher TIT value, increased at 491.6 °C, while reducing the power provided by the heat source, exchanged in the HTS.

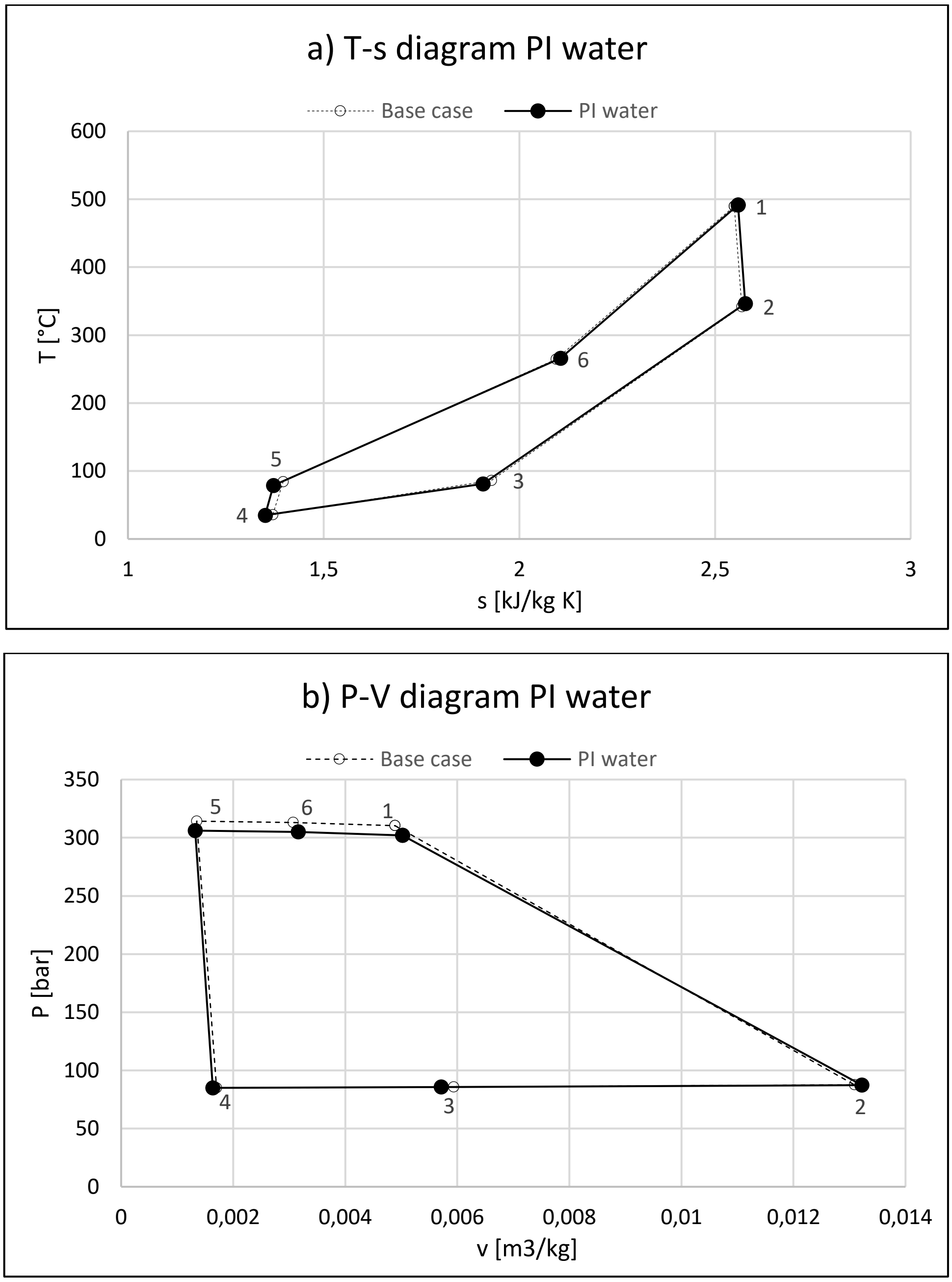

Figure 42 a) T-s and b) P-V diagram after the water PI activation

The improvements are reflected in the overall system's performance: the compressor decreases its power absorption of 40 MW and the heat input is also reduced of 50 MW. On the other hand, the smaller mass flow rate implies lower power output from the turbine, but, however, the global effect on the cycle is positive. The results confirm what expected, showing a system improvement, with an increase of cycle efficiency of almost one percentage point. Table 10 resumes the differences explained above with the base case (Real cycle steady state).

Table 10 Summary of results after the water PI activation compared with the real case static

	Base case	PI water	Relative Difference
CO_2 Mass flow [kg/s]	7008.32	6835.13	-2.47%
Molten Salt Flow [kg/s]	6184.60	6184.60	0.00%
Water Flow [kg/s]	29297.00	31657.13	8.06%
Efficiency	36.83%	37.48%	1.77%
Compressor Power [GW]	0.30	0.26	-11.59%
Turbine Power [GW]	1.05	1.01	-3.88%
HTR Power [GW]	2.12	2.16	1.79%
HTS Power [GW]	2.04	1.99	-2.55%
PC Power [GW]	1.27	1.22	-3.55%
Total Pressure Drop CO2 [bar]	6.48	6.21	-4.12%
Low Pressure Level [bar]	85.00	85.00	0.00%
High Pressure Level [bar]	314.24	306.11	-2.59%
Minimum Temperature [°C]	35.61	35.00	-1.71%
Maximum Temperature [°C]	489.67	491.62	0.40%

4.1.2 Molten salt flow control

The second PI controller has been introduced to manipulate the molten salt mass flow in order to manage the turbine inlet temperature, stabilizing it at the nominal value. In a real situation, this should enhance the device's performances, but in the present model no distinct improvements are expected in the device, due to its performance curves independency of the inlet temperature. Rather, the control will be useful during the second partial-load operation strategy tested.

For its calibration a molten salt mass flow step of -30% has been imposed, analysing the TIT variation in response. This time le perturbation has been started after the introduction of the water control and the achievement of the steady state with the compressor inlet temperature stabilized at 35 °C, at 500 seconds. The considerable drop in molten salt mass flow causes a decrease of almost 80 °C at the turbine inlet, with a delay of about 600 seconds (Figure 43).

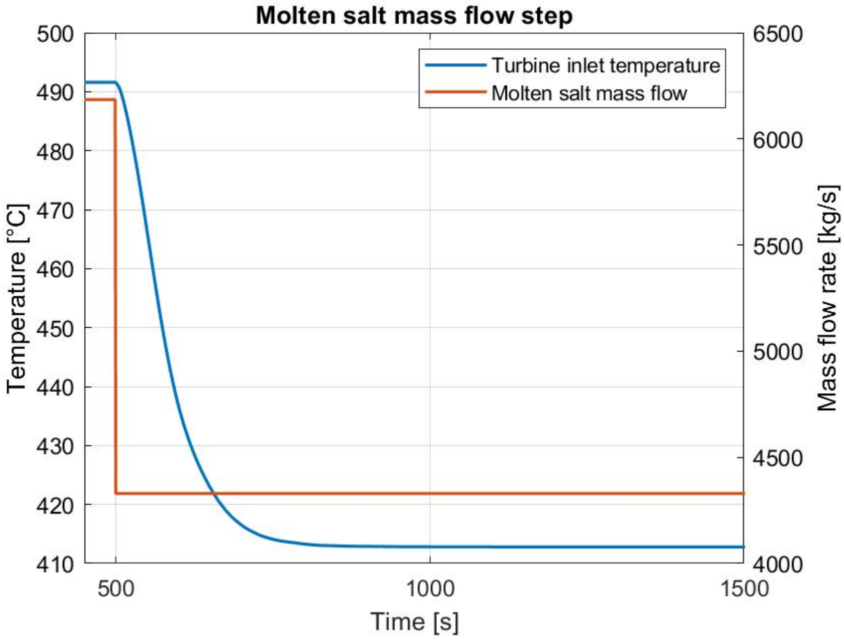

Figure 43 Molten salt step variation

Further in the loop, it is interesting to appreciate the activity of the water PI controller, shown in Figure 44; the temperature decrease is transported till the compressor inlet and perceived by the controller, which tries to compensate the perturbation reducing the water mass flow. The response is initially excessively strong and the temperature rises quickly, crossing the 35 °C border. The control system adapts its output and gently increase the water flow, finally stabilizing the temperature at 35 °C.

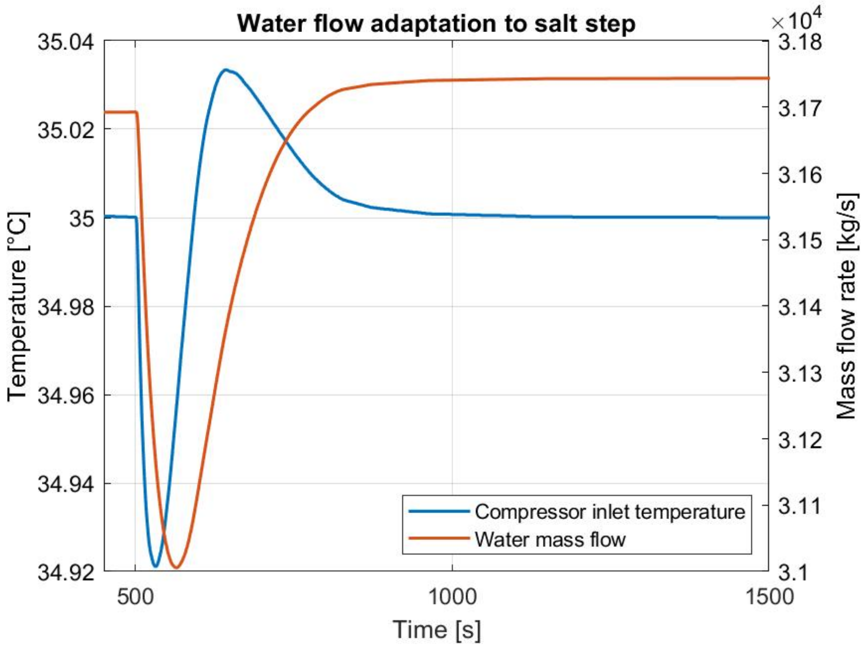

Figure 44 Water PI response to the salt step

With the tuning procedure, it is possible to set up the PI controller, deciding for a more conservative control, due to the delay elapsing between the control action and the TIT variation: $K_c = 5.3176$ and $Ti = 6.65\ s$.

The controller is activated at 500 seconds, leaving the system enough time to reach the steady state, after the first control, fixing the set point at 490 °C. The temperature at the turbine inlet is initially higher than the set point value, therefore, the PI will reduce the molten salt flow and slowly stabilize the TIT, reaching the target with 6031.5 kg/s of molten salt.

The HTS is the exchanger with the highest size and consequently highest inertia in the loop, thus the control will act in quite long time, requiring around 600 seconds to reach the new steady state (Figure 45). This is noticeable also by the delay between the two minimums of the curves, almost 100 seconds far, time needed to transfer the thermal information till the turbine inlet, justifying also the necessity of a more conservative control action, which otherwise could make the TIT oscillating and, eventually, cause damages in a real turbo-machine if chosen too aggressive.

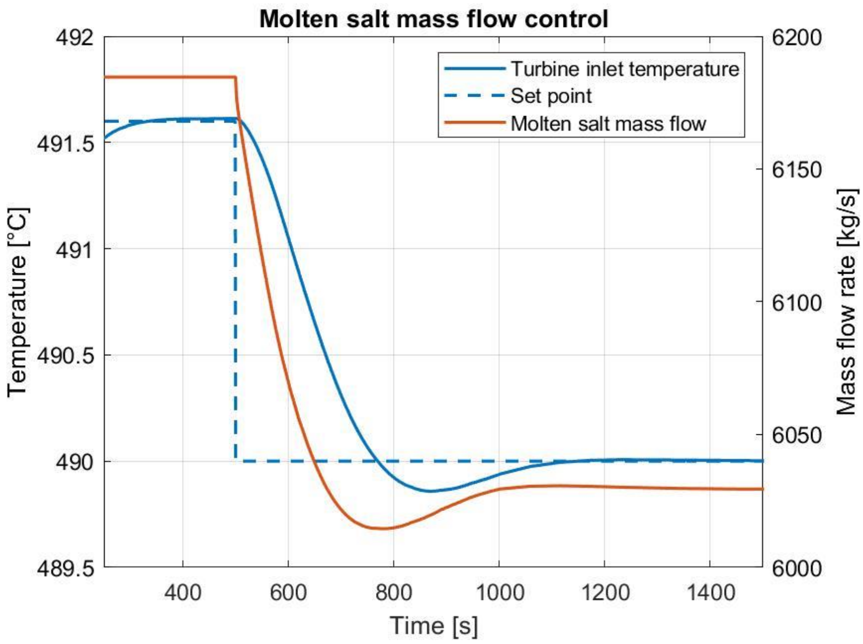

Figure 45 Molten salt PI activation

The decrease of TIT causes a reduction of the inlet pressure and a raise in density, which in turn implies a congestion of the flow before the heat exchanger, and a decrease of mass flow rate at the turbine inlet (Figure 46).

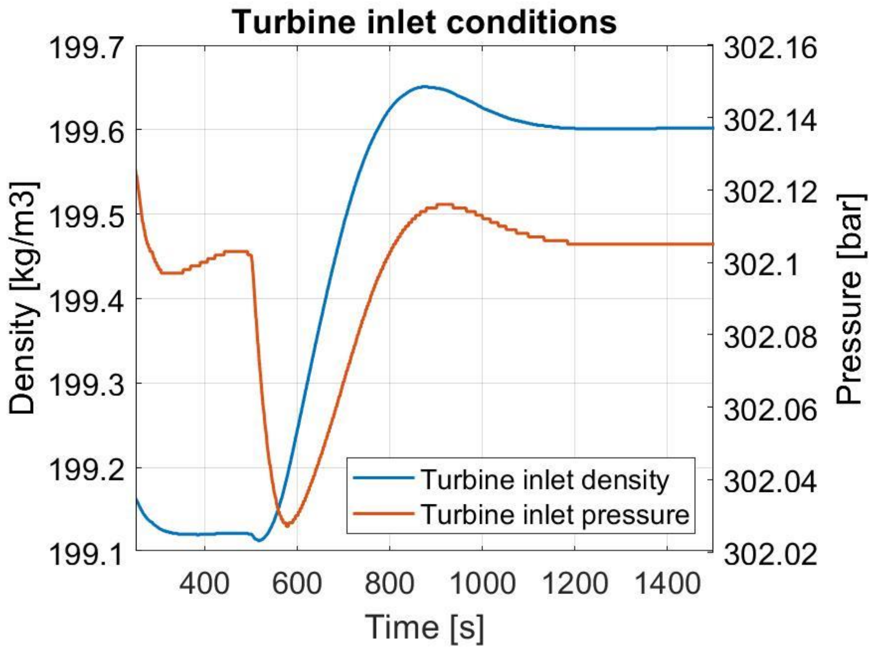

Figure 46 Turbine inlet density and pressure

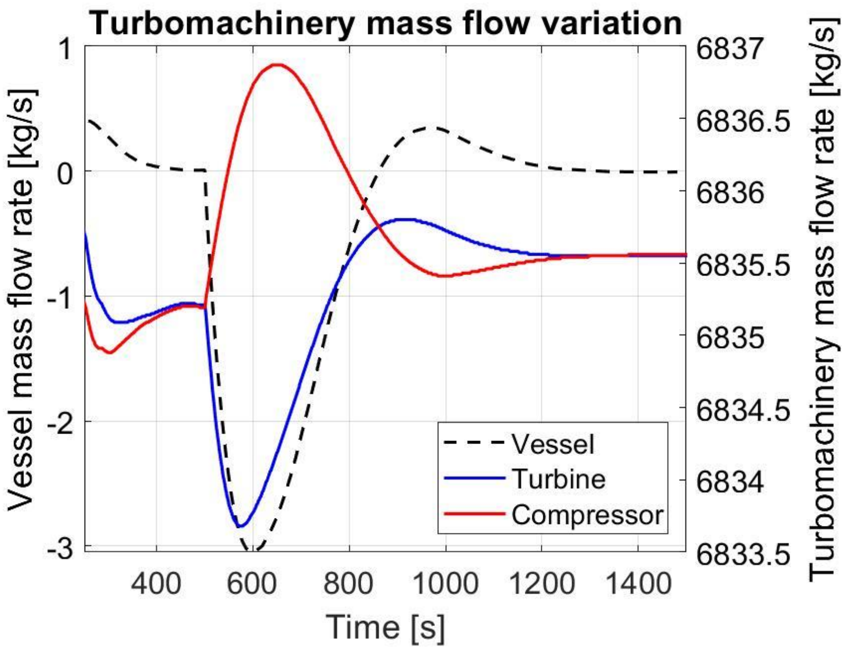

Figure 47 Mass flow rates in turbine, compressor and expansion vessel. Note: negative values mean flow injected in the loop

The pressure drop should now be transmitted further in loop, but, meanwhile, the expansion vessel works to keep the pressure constant at the compressor inlet, accepting or injecting mass when needed; in particular, to compensate the pressure drop, the component is introducing a small amount of mass in the system (Figure 47) making the compressor working with a slightly higher flow. After that, the molten salt control will stabilize the TIT and, hence, all the other parameters.

On the other hand, the well-functioning of the water control can be noticed again by checking the compressor inlet temperature, whose variation is almost null thanks to the PI action, which limits its variations in the order of 1E-4, even difficult to be visualized in Dymola, as can be noticed from Figure 48.

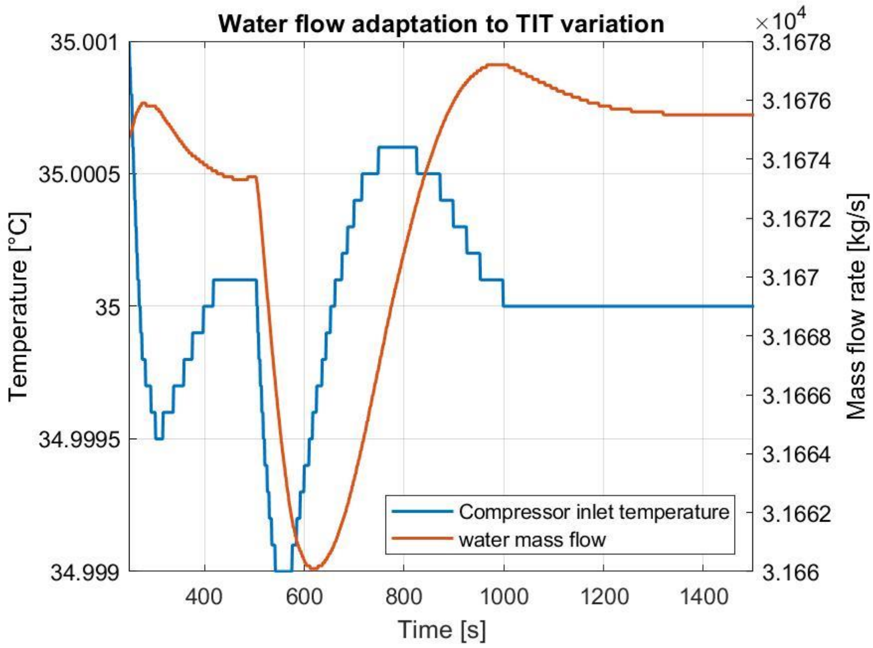

Figure 48 Water PI activity at molten salt PI activation

Table 11 resumes the cycle's results, compared with the previous case with the only PI water controller activated. As can be seen, the overall system doesn't show with any particular strong response to the variation, with carbon dioxide mass flow, pressure and temperature levels almost unvaried once achieved the new steady state. Even if the turbine is now working with the nominal inlet temperature, it results to be disadvantaged by the temperature control: the device is operating with almost the same efficiency, due to the shape of its performance curves, but the lower mass flow rate and TIT will make the turbine extracting slightly less power from the fluid, marginally affecting the global cycle efficiency. To conclude, the control didn't bring any improvement, rather small decreases in the loop's performances due to the turbine's definition, while in a real component more concrete enhancements are expected. However, the control will be useful in the second part-load strategy.

Table 11 Summary of results after the molten salt PI activation

	PI water	PI salt	Relative Difference
CO_2 Mass Flow [kg/s]	6835.13	6835.54	-0.02%
Molten Salt Flow [kg/s]	6184.60	6031.52	-2.48%
Water Flow [kg/s]	31657.13	31675.48	0.06%
Efficiency	37.48%	37.39%	-0.23%
Compressor Power [GW]	0.26	0.26	-0.01%
Turbine Power [GW]	1.01	1.01	-0.29%
HTR Power [GW]	2.16	2.15	-0.54%
HTS Power [GW]	1.99	1.99	-0.17%
PC Power [GW]	1.22	1.22	-0.02%
Total Pressure Drop CO2 [bar]	6.21	6.24	0.48%
Low Pressure Level [bar]	85.00	85.00	0.00%
High Pressure Level [bar]	306.11	306.17	0.02%
Minimum Temperature [°C]	35.00	35.00	0.00%
Maximum Temperature [°C]	491.62	490.00	-0.33%

4.1.3 Valve control

The control of the valve aperture was the last one inserted, thought as way to impose a further pressure drop to the system in order to manage the cycle's power output through the mass flow rate. As mentioned in the chapter introduction, the valve is located after the compressor, at the end of the first set of pipes, adding a small pressure drop of about 0.16 bar when totally open; it can be controller through the opening factor, which is not physically the valve's aperture, but acts as multiplier for the valve's area, taking part in the computation of pressure drop and mass flow rate across the valve. A decrease of this parameter would cause a flow congestion in the valve, with a consequent increase of the inlet pressure, that the compressor will have to face. As consequence of this, the mass flow will result overall reduced, causing a related reduction of the power output.

As done for the previous cases, the component has been tested with a sharp variation, bringing the opening factor from 1, totally opened, to 0.1 at the second 1500, after the action of the previous two controllers and the achievement of the steady state; then, the system's response in terms of cycle power output has been measured (Figure 49).

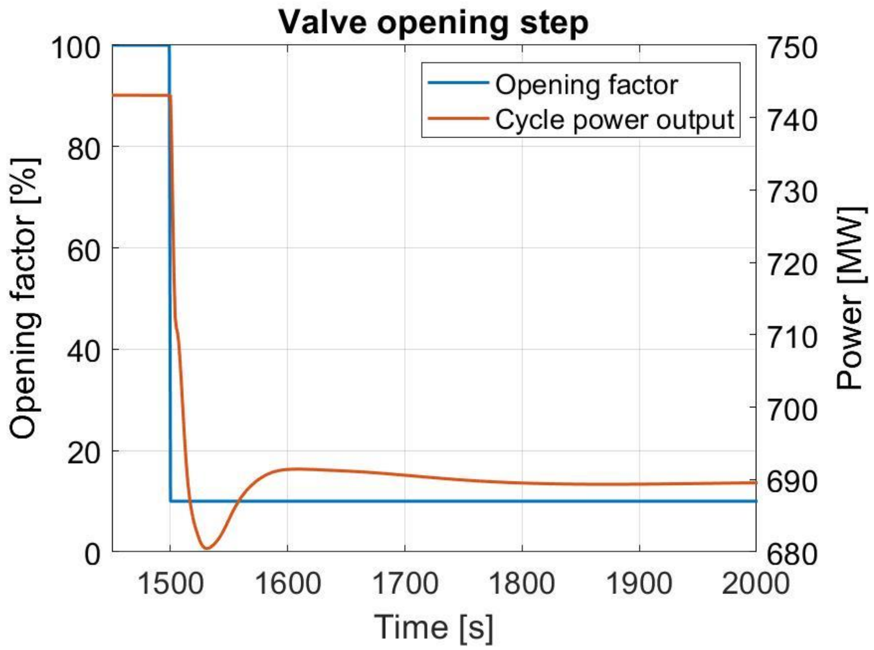

Figure 49 Valve opening factor step effects on cycle power output

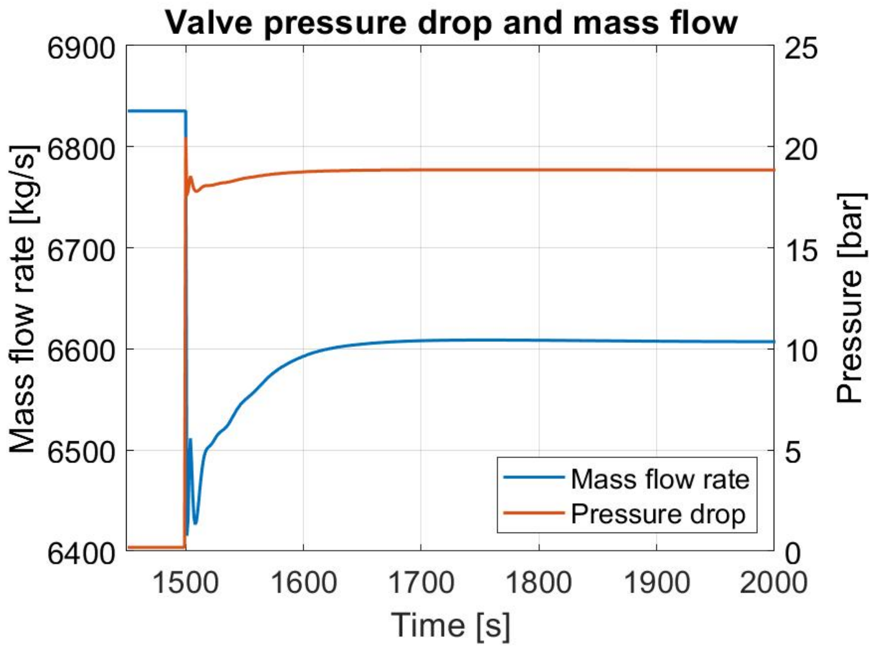

Figure 50 Mass flow rate and pressure drop after the valve closure

As expected, the power output decreases with the valve closure, consequently of the higher pressure loss and smaller mass flow rate (Figure 50), dropping of about 150 MW. According to the PI's tuning procedure, the controller has been set with $K_c = 2.642E - 9$ and $Ti = 136\ s$.

4.2 Partial load operation strategies

Operating the plant with partial load is one of the most common situations that a power plant could face, due to several factors, like the need to meet a variable demand, heat source's availability, economic reasons and many others. Though, the partial operation of a supercritical cycle is non-trivial due to the non-linear properties of the fluid, much more complex than an ideal gas.

Many strategies can be used for the purpose, mainly acting on mass flow and temperatures in different points of the loop. Two of them have been be here tested and benchmarked, one acting on the Turbine Inlet Temperature and the other on the mass flow through a valve. Typically, controlling the power output through the TIT is not recommended for two reasons: firstly, it would lead to a consistent cycle efficiency decrease and, secondly, since the turbine is built to operate at prescribed temperatures, running it at sensibly lower values would mean working with low isentropic efficiency and even leading to malfunctions or damages. Instead of this strategy, it is usually preferred to act on the compressor inlet conditions, even though its closeness to the critical point makes this technique more risky, or using valves for bypass and throttling, considered more effective (Carstens, 2004). Generally, the main goal of a part-load strategy is to reduce the power output while keeping the components operating as much as possible within their nominal conditions and, consequently, retain as high cycle's efficiencies as possible.

In both of the strategies tested, the plant's power output has been lowered from the nominal operation of 770 MW to 600 MW, simulating a 20% reduction in 10 minutes, starting at the 1500th second with steady state conditions. The results will be analysed and, based on the cycle's efficiency, it will be decided which of the two should be preferred.

4.2.1 Turbine Inlet Temperature

The first strategy focuses on the TIT value to reduce the global power output. At lower temperatures, the power that the turbine can extract is smaller even if the device is operating with high efficiencies, due to the thermodynamic properties of the fluid. Indeed, considering two isobaric curves in the *h-s*, it is evident that the distance between the two is growing with the temperature; as a consequence of this, the enthalpy jump harvestable by the turbine is smaller at lower temperature. In Figure 51 the enthalpy (solid) and temperature (dotted) isobaric curves of CO_2 as function of entropy are shown, respectively at 300 bar and 85.8 bar, the reference cycle's conditions. It is evident that, imaging an isentropic process, the enthalpy gap at higher temperature is bigger than at lower values.

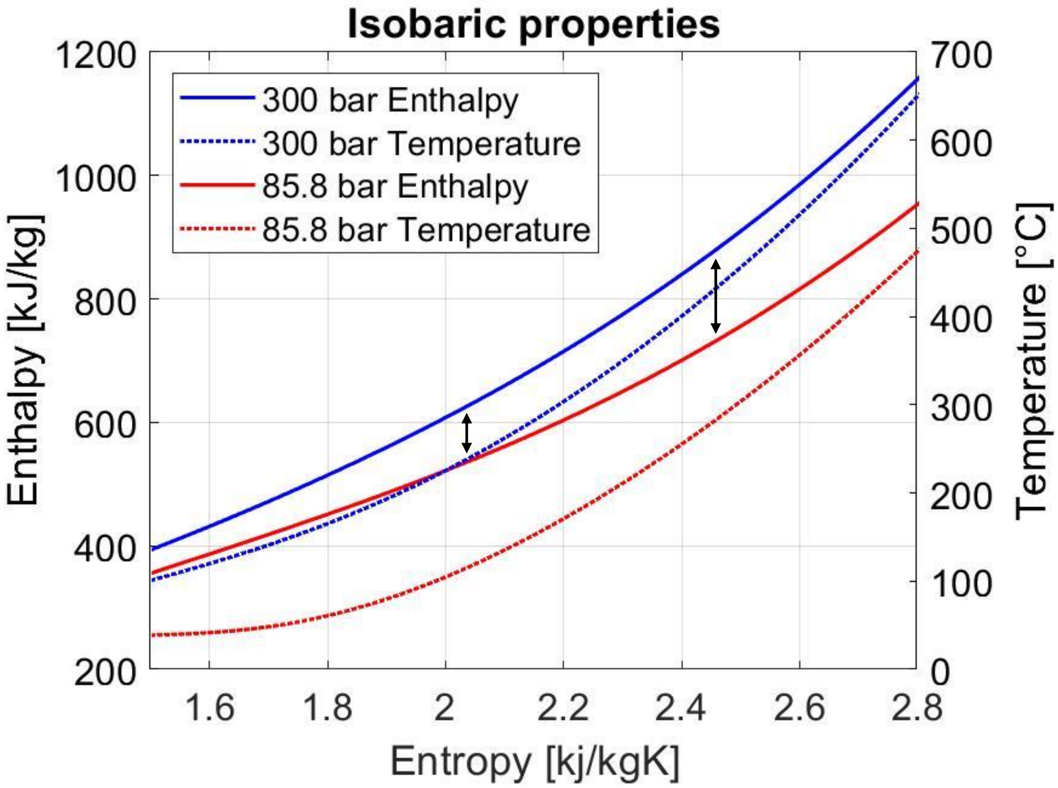

Figure 51 Example of reduced enthalpy head at lower temperatures

To perform this control technique, the PI acting on the molten salt flow should be reset, in order to seek the power output rather than the turbine inlet temperature. The tuning procedure, not reported since the same as the multiples presented, led to the following PI settings: $K_c = 3E - 6$ and $Ti = 6\ s$.

Theoretically, in a real turbine the efficiency should decrease with lower inlet temperature, since moving from the nominal value. While, being the device used here not real, its efficiency is function only of the mass flow rate and the speed, as explained in the System Description; moreover, the efficiency curve at 3000 rpm is almost flat for a wide range of flow values, therefore, the component is expected to operate with almost constant efficiency also with TITs considerably lower. Thus, the reduction in power output will be consequence of the thermodynamic conditions of the fluid, rather than the turbine's functioning.

On the other hand, lowering the temperature will imply higher densities and lower pressures, that will be compensated by the expansion vessel, injecting fluid in the loop and increasing the mass flow rate; thus, being the turbine's PR characteristic linearly proportional with the mass flow rate, the pressure head imposed by the device, is expected to be even higher than at nominal TIT values. Anyway, the reduction of harvestable enthalpy due to the temperature drop will be more consistent than the increase related to the bigger pressure head, leading to a global reduction of its power output.

Meanwhile, the compressor will operate with fixed inlet conditions since the controls are still active, just elaborating a higher mass flow, reflected in a lower PR and isentropic efficiency.

The reduction of the turbine inlet temperature, while keeping the compressor inlet's thermodynamic conditions fixed, will only lead to a reduction of the high-temperature level, with almost constant pressure. This is evident by the *T-s* diagram, where the cycle's right side is clearly squeezed towards left, keeping the left part almost unvaried. In the same way, the density will increase, resulting in lower specific volumes and lower power of the turbine. In particular, in the *P-V* diagram it is possible to notice that the line 1-2 results now more tilted; therefore the area below that curve, representing the specific work of the turbine, will be smaller.

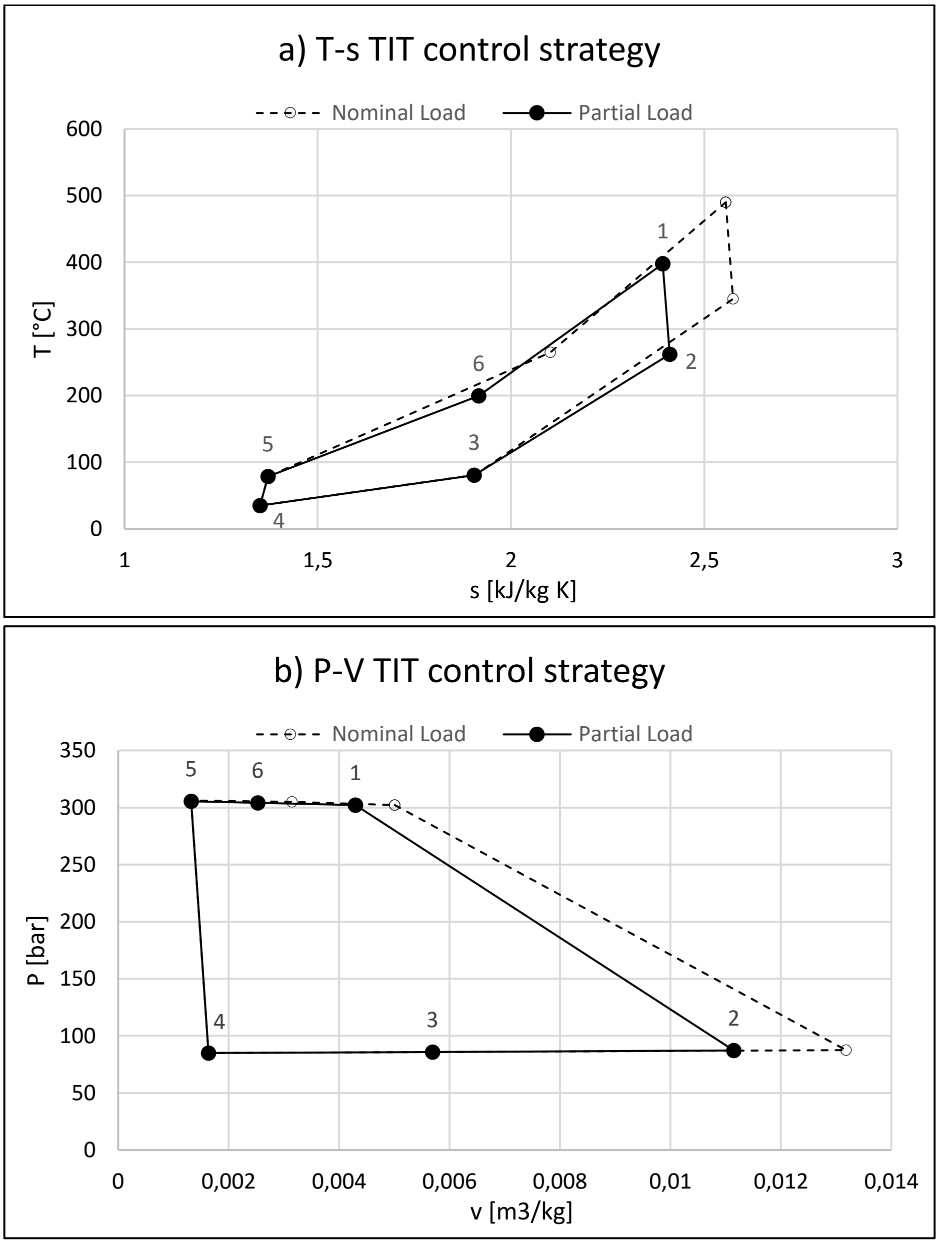

Figure 52 a) T-s and b) P-V diagram of the first control strategy

In Figure 53 it is possible to see the decrease of the set point power and the action of the PI controller, reducing the molten salt mass flow according to the error between the set point and the process variable, the net power output. From this, it is evident the effectiveness of the control, since the net power produced follows faithfully the set point, requiring only around 100 seconds to reach the steady state once the set point has been stabilized, finding the new equilibrium with 4122 kg/s of molten salt and a TIT value of 397 °C. In the first half of the process it is possible to notice a first aggressive response of the control that imposes a steeper reduction of the salt, followed by a short nearly flat behaviour and a further smoother decrease.

These two slopes in the molten salt variation are reflected in the TIT, which mirrors its trend, with a first sharp drop that then becomes softer, followed by the density with opposite behaviour (Figure 54).

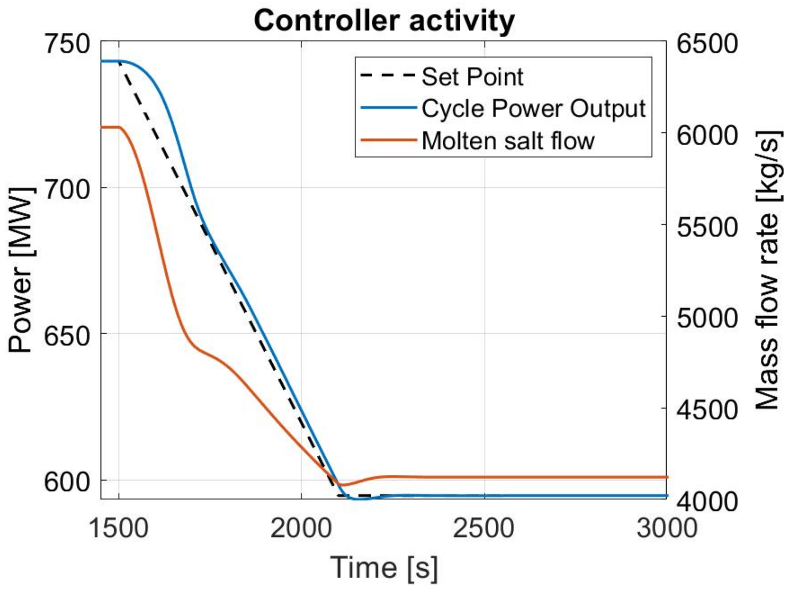

Figure 53 Controller activity and effect on the molten salt

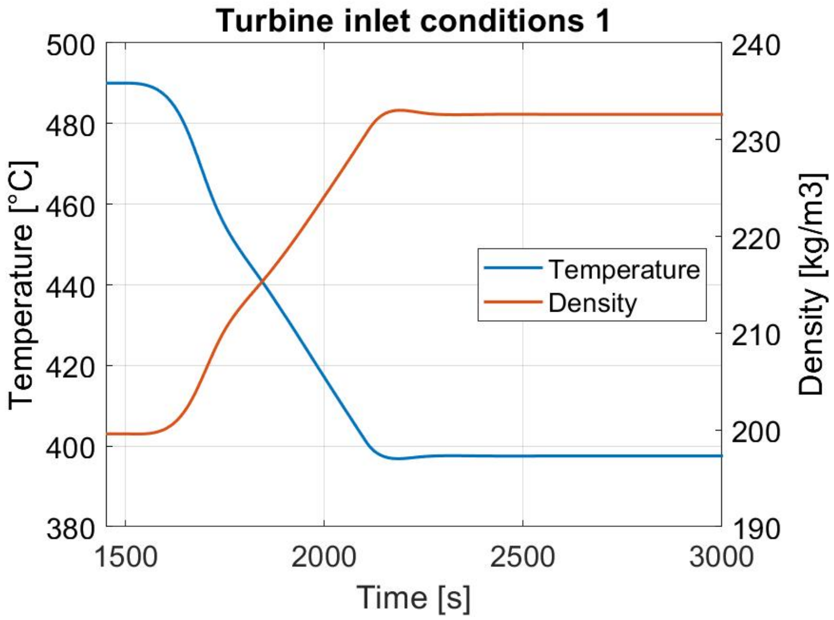

Figure 54 Temperature and density at turbine inlet

Much more evident oscillations, due to the same reason, are evident in the turbine inlet pressure, and consequently in the mass flow rate; in the same way as explained in Section 4.1.2, being the density lower, the pressure in the system would decrease, but the expansion tank reacts and stabilizes it injecting mass in the loop, which at the end of the transitory will result around 20 kg/s higher than before the variation. On the other hand, the pressure at the turbine inlet returns almost at the same value as during the nominal load (Figure 55).

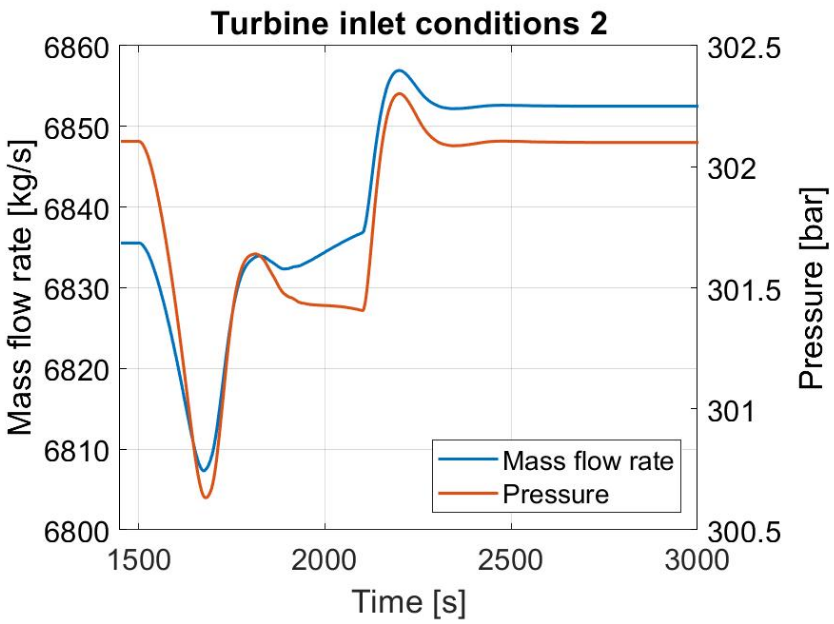

Figure 55 Pressure and mass flow rate at the turbine inlet

The effects of the control strategy on the power output can be seen checking the turbomachinery's activity: the compressor is working with almost the same power and efficiency as before (80.96% against 81.03%), since its inlet conditions are kept fixed by the control system; the slight variations are due to the increase of mass flow, as well as the intermediate oscillations.

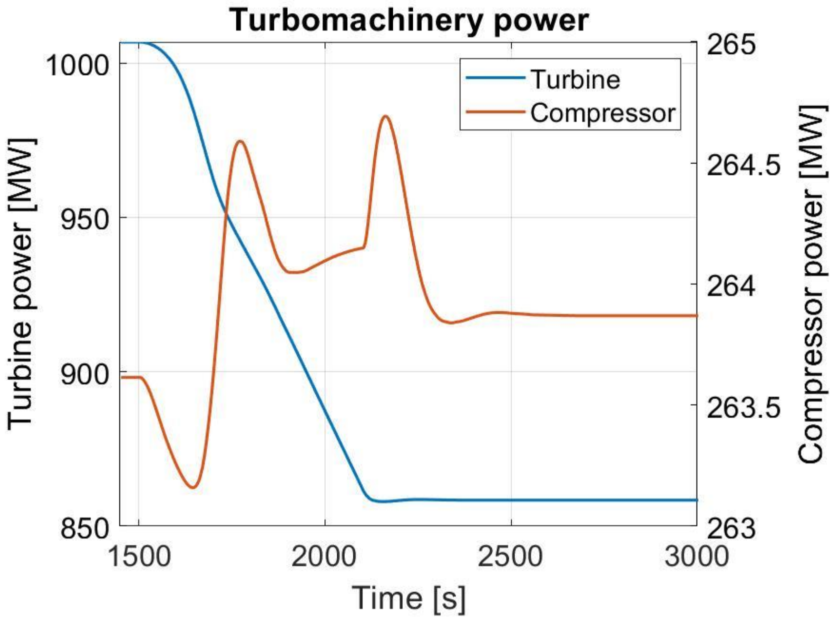

Figure 56 Compressor and turbine powers

As expected, the turbine is the component more affected by the control action, loosing almost 200 MW of power production; its efficiency is almost constant (the variation is in the range of 0.01%) while the pressure ratio slightly increases thanks to the higher mass flow rate, releasing the fluid at about 0.2 bar less than at nominal load. However, the enthalpy collectable by the component is significantly lower, as explained before; Figure 57 presents the isentropic (left) and real (right) enthalpy heads, before and after the change of TIT, showing that the harvestable enthalpy is decreased.

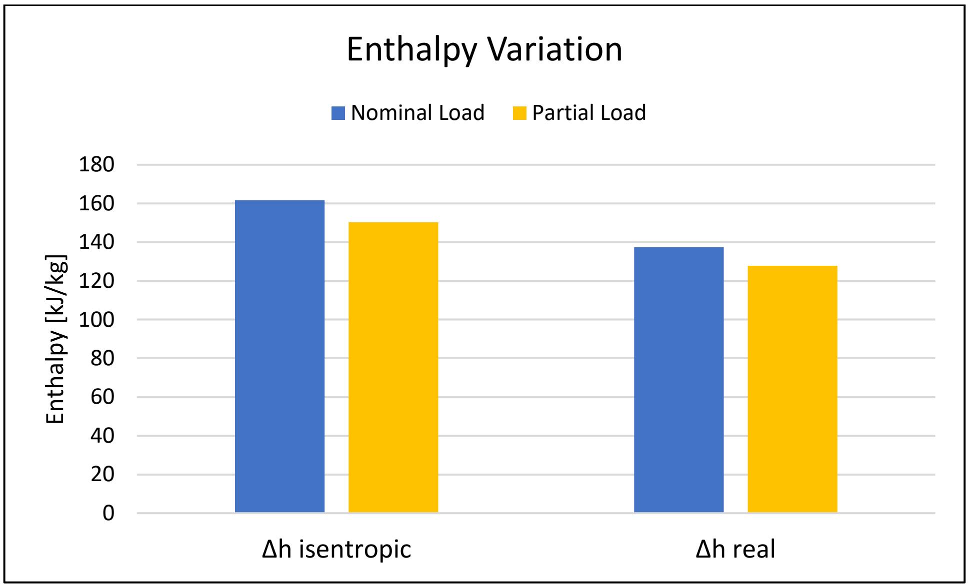

Figure 57 Enthalpy head ideal and real, before the control (blue) and after the control (yellow)

Table 12 resumes the main results of the partial load operation explained. It can be noticed that almost all the components powers are decreased; obviously, external heat input is reduced and this improves the global efficiency, but in the efficiency this is not enough to compensate the less turbine power output, leading to a cycle efficiency loss of five percentage points. Moreover, the lower temperature at the turbine outlet reduces the possibility of heat recovery in the HTR; it results to be the exchanger most affected, with the biggest reduction of thermal power exchanged, more than 600 MW. Becoming less recuperative, the cycle will operate with lower performances.

Table 12 TIT control strategy summary

	Nominal Load	**Partial Load**	**Relative Difference**
CO_2 Mass Flow [kg/s]	6835.13	6852.50	0.25%
Molten Salt Flow [kg/s]	6031.52	4121.94	-31.66%
Water Flow [kg/s]	31675.48	31731.60	0.18%
Cycle Efficiency	37.48%	32.44%	-13.46%
Compressor Power [GW]	0.26	0.26	0.10%
Turbine Power [GW]	1.01	0.86	-14.94%
HTR Power [GW]	2.16	1.51	-29.99%
HTS Power [GW]	1.99	1.83	-7.86%
PC Power [GW]	1.22	1.22	-0.19%
Total Pressure Drop CO2 [bar]	6.21	5.36	-13.73%
Low Pressure Level [bar]	85.00	85.00	0.00%
High Pressure Level [bar]	306.11	305.48	-0.21%
Minimum Temperature [°C]	35.00	35.00	0.00%
Maximum Temperature [°C]	491.62	397.54	-19.14%

4.2.2 Valve closure

The second and last strategy presented acts on the opening factor of the valve located 80 meters far after the compressor; closing the valve, an additional pressure drop will be created, reducing the mass flow rate in the loop and, consequently the power output. Compared to the previous technique, this one is a third control level, after the PIs acting on water and molten salt flows, and its integration in Dymola carried with it some difficulties, requiring a proper initialization of the system and many attempts. In particular, the most critical moment was the end of the set point's ramp, when it reaches the final value; at that time, still some computational oscillations are present. It must be highlighted that the PI acting on the molten salt flow has been again reset to the original values, in order to fix the TIT at 490 °C.

Goal of this strategy is the reduction of the cycle's power output by lowering the mass flow circulating, while keeping the loop's thermodynamic conditions as close as possible to the nominals, in order to maintain high efficiency values of the components and the entire cycle.

The valve's closure will cause a congestion of the fluid flow, that in turn will imply an increase of pressure at the valve inlet, which the compressor should face imposing a higher PR. According to the performance curves, being the turbo-machine inlet conditions and the rotation velocity fixed, the device will have to reduce the relative mass flow rate, and consequently the mass flow, in order to provide a higher PR. Checking the efficiency curves in the same way, it can be forecasted that the device's efficiency will increase with lower ν, so the fluid's temperature at its outlet will be lower. The combined effect of reduced mass flow rate and higher efficiency will lower also the power absorbed by the compressor.

Similarly, the lower mass flow will make the heat exchange in HTS and PC more efficient, therefore, the control systems will have to adapt their action, decreasing the flows of both salt and water, in order to respect the set point temperatures at the turbomachinery inlet.

On the other hand, the turbine is expected to work with almost unvaried efficiency thanks to its performance curve particularly flat at 3000rpm; the inlet temperature is controlled, while the lower mass flow rate will be reflected in a smaller PR value, thus the turbine will be able to exploit a lower enthalpy head; this, joined with the smaller mass flow will imply less power extracted by the device.

Globally, the presence of controls, will help to maintain the temperature conditions almost stable all over the loop, but, due to the new consistent pressure drop, the entire cycle will work at a lower high-pressure level, while the low-pressure level will be maintained thanks to the expansion vessel, which keeps the compressor inlet pressure fixed at 85 bar.

Similarly to the previous strategy, the cycle net power output set point has been lowered by 20% in 10 minutes at the 1500th second; as it is possible to see in Figure 58 and Figure 59, the effect of the opening factor is almost negligible until 20%, after which small changes cause consistent variations of pressure drop, becoming extreme at values in proximity to zero, where very tiny variation of the opening factor causes important pressure drop oscillations, that will be reflected in every loop's variable. This witnesses the sensibility of this control and proves the difficulties related to its integration in the model; indeed, the oscillations present at the time 2100 could be also attributed the growing effect of the valve closure or to computational inaccuracies, which could be object of further studies and improvements. The target has been reached with an opening factor of 5.76%, to which is related a pressure drop of 50.85 bar.

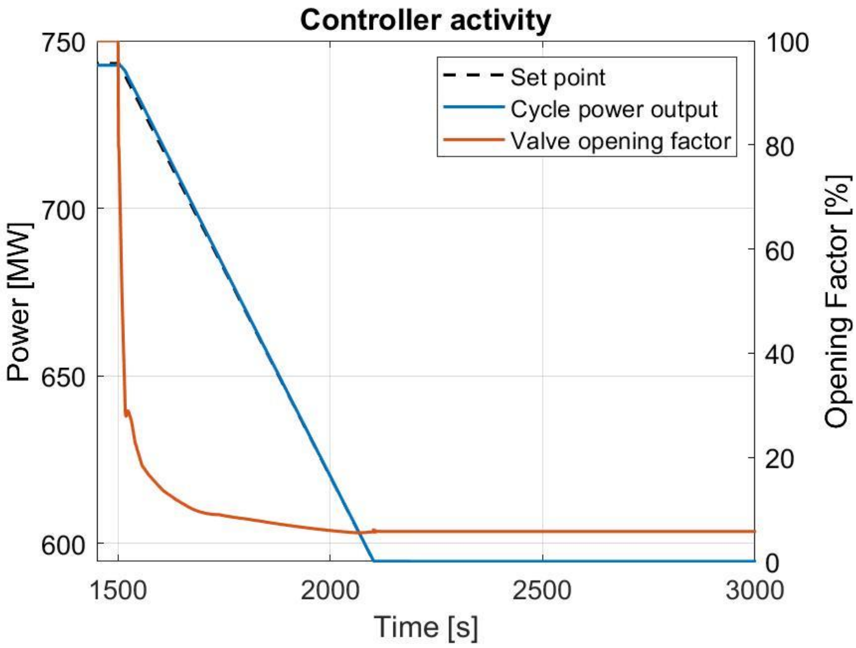

Figure 58 Valve opening factor effect on the cycle power output

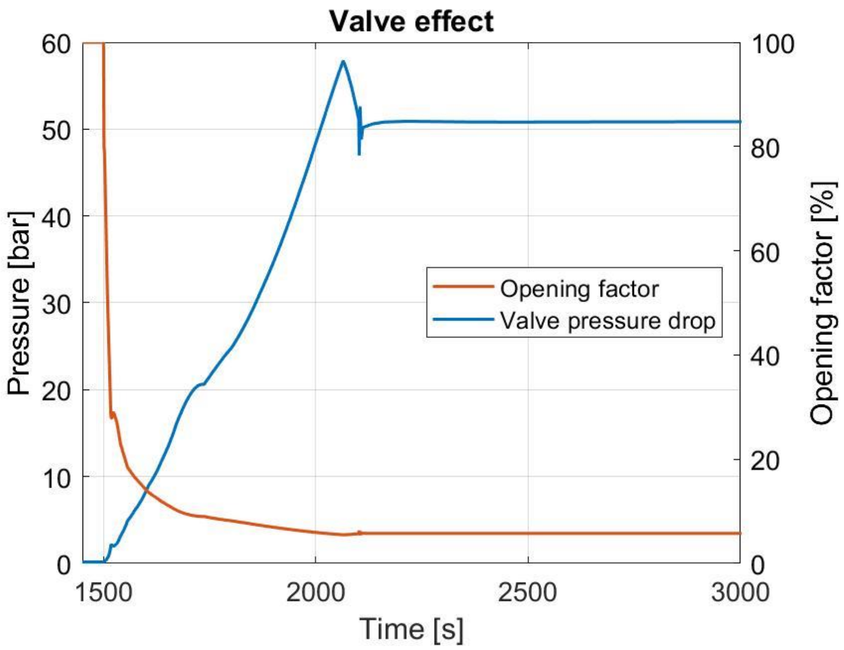

Figure 59 Valve opening factor effect on pressure drop

During the transient, the increment of the pressure drop is followed by a reduction of mass flow passing across the valve, which undergoes a consistent decrease, with an important oscillation again at 2100 seconds when also the pressure drop has, then stabilized at 6189 kg/s. As expected, the inlet pressure increases as consequence of the flow congestion, while the outlet pressure has a symmetrical behaviour, dropping quickly. Moreover, the outlet valve pressure presents the same specular minimum as the pressure drop, then absorbed along the loop and not visible anymore at the turbine inlet, as well as the oscillations at 2100 seconds (Figure 60 and Figure 61).

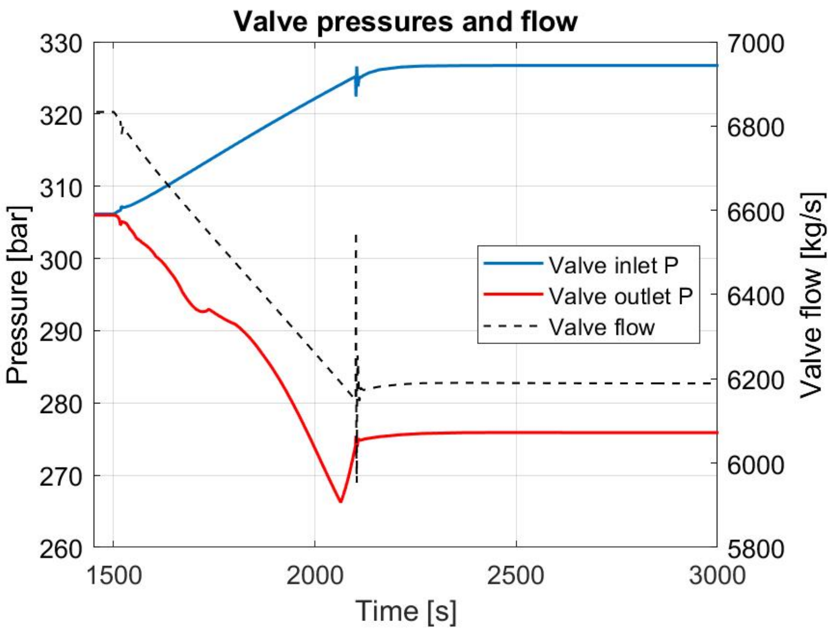

Figure 60 Pressures and mass flow rate across the valve

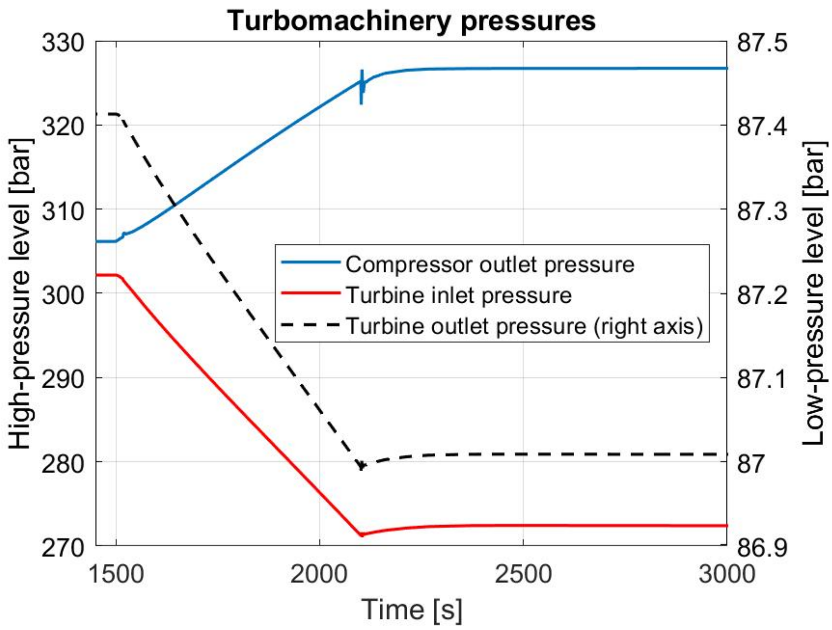

Figure 61 Turbomachinery pressures

Upstream the valve, the expansion tank acts in order to keep the compressor inlet pressure fixed, helping its activity: the raise of pressure that the compressor is facing, requires a higher pressure ratio, that at fixed inlet thermodynamic conditions and rotational speed, can be reached through a decrease of mass flow as explained above; therefore, the expansion vessel will collect fluid during the transient, followed by a marked oscillation at 2100 seconds connected with the ones explained before (Figure 62). The compressor's operation point on the performances curves shows what just explained, the reduction of relative flow rate guarantees the needed PR, while increasing the component's efficiency as foreseen (Figure 63).

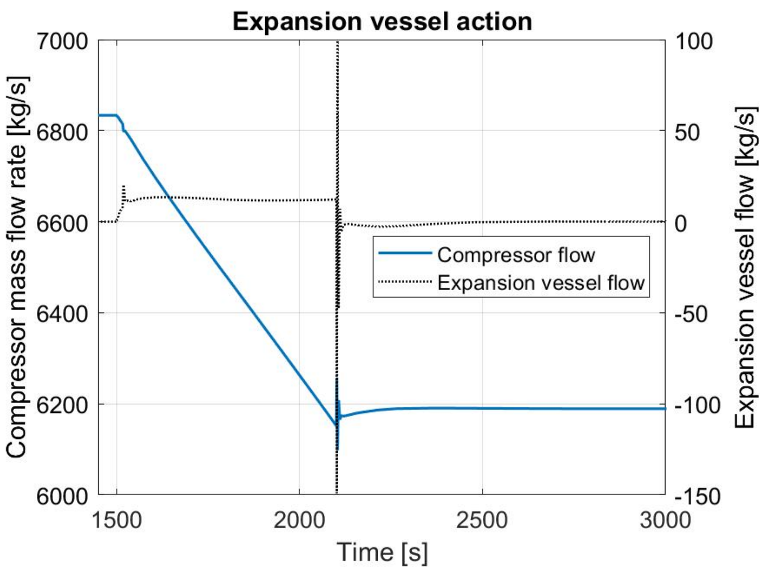

Figure 62 Compressor and expansion vessel flow during the second part-load operation. Note: positive values of vessel's flow mean fluid injected in the loop

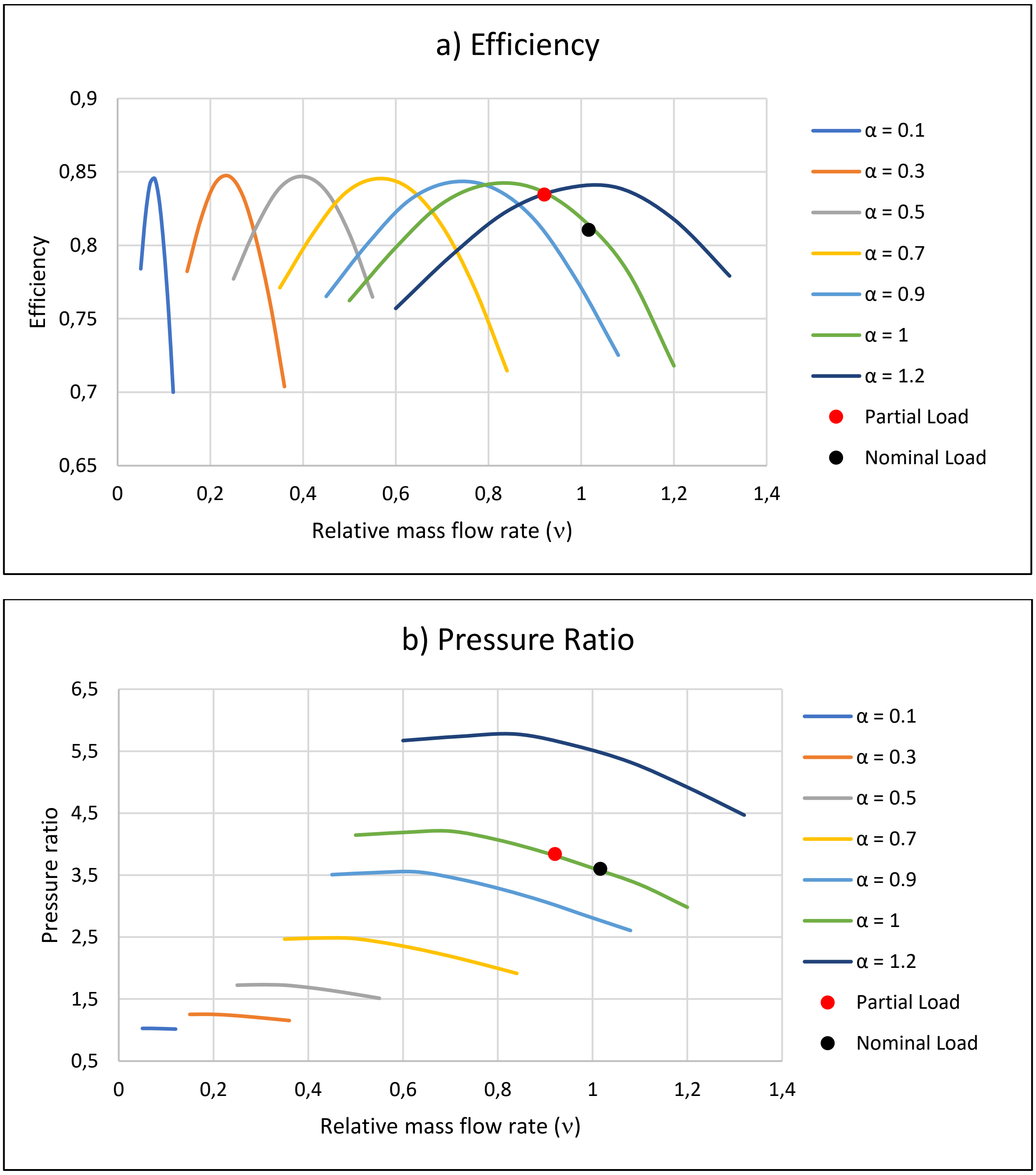

Figure 63 Compressor operation point after the second part-load operation, in a) efficiency and b) pressure ratio curves

The valve's effect is particular evident in the *P-V* diagram (Figure 64.b) where the 6th and 1st point of the loop, respectively indicating the locations after HTR and HTS, result considerably shifted towards lower pressures, due to the pressure drop imposed by the component. Further in the cycle, the expansion vessel fixes the low-pressure level, therefore the turbine is accepting fluid at lower pressure but will discharge it almost at the same pressure than before the part-load operation, so globally the pressure head will be lower and the mass flow reduction will allow the turbine to guarantee the desired PR value.

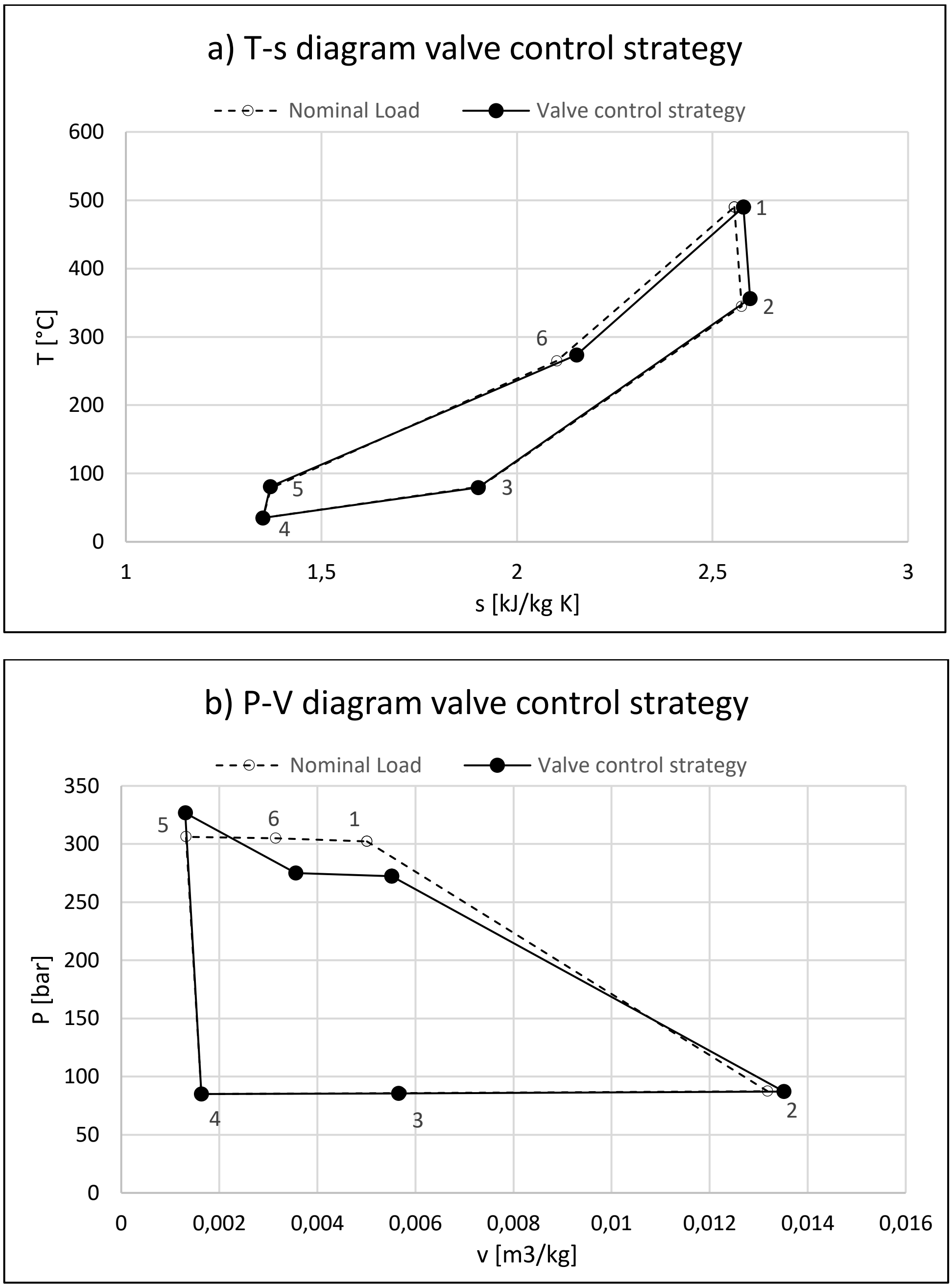

Figure 64 a) T-s and b) P-V diagram at partial load operation

On the other hand, the *T-s* diagram (Figure 64.a) results almost unchanged, being the upper and lower temperatures controlled; the right side of the graph results just slightly shifted towards higher entropy values, due to the lower pressure (at isothermal conditions the entropy is inversely proportional to the pressure). Moreover, being the temperature also unvaried, the specific heat transferred in the heat exchangers will remain mainly constant; indeed, the areas below lines 6-1 (HTS), 3-4 (PC), 5-6 and 2-3 (HTR) are approximately unchanged. The only variation is a small increase of the heat recovered by the HTR, lowering the one provided by the HTS.

To guarantee the temperature stability, the controllers are adapting the mass flow rates of salt and water to the new CO_2 conditions, acting as awaited. In both exchangers, the flows of molten salt and water are decreasing, since less CO_2 is crossing the components. It can be noticed from the graphs below that in HXs, the reduction of CO_2 flow is accompanied by, respectively, a temperature increase in HTS (Figure 65) and decrease in the PC (Figure 66). This can be explained by the exchangers' thermal inertia and the lower flow which enhance the heat exchange temporarily. None of the control systems is able to keep the temperatures perfectly at the set point during the transient, due to several reasons, like the continuous variation of the carbon dioxide flow, different reactivity of the control systems and thermal inertia of the exchangers, and the consequent time delay of control's effectiveness. The first control requires around 600 seconds to bring the TIT temperature back to 490 °C after the end of the transient, while the second manages it in about 300 seconds.

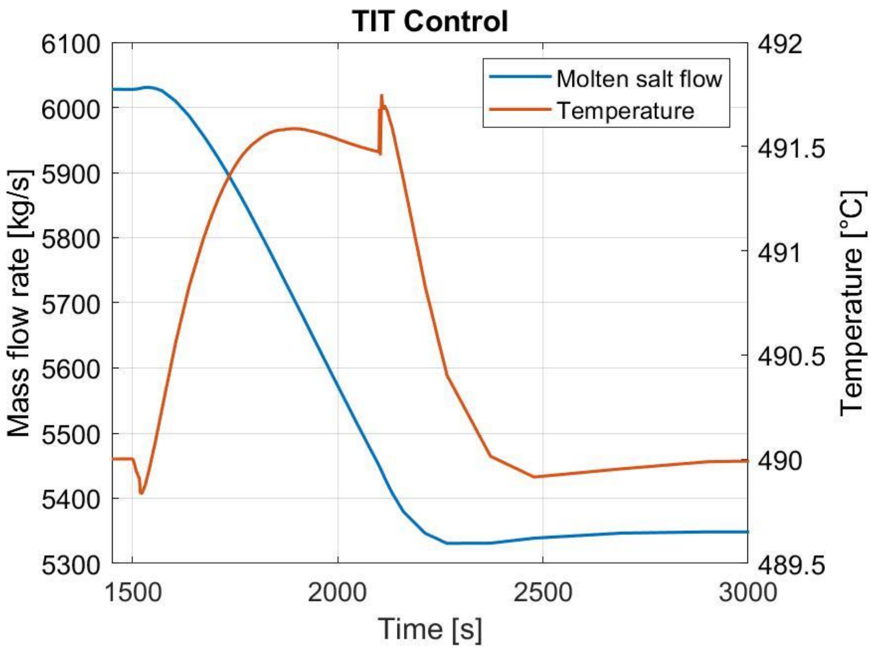

Figure 65 Molten salt control system activity during the second part-load operation

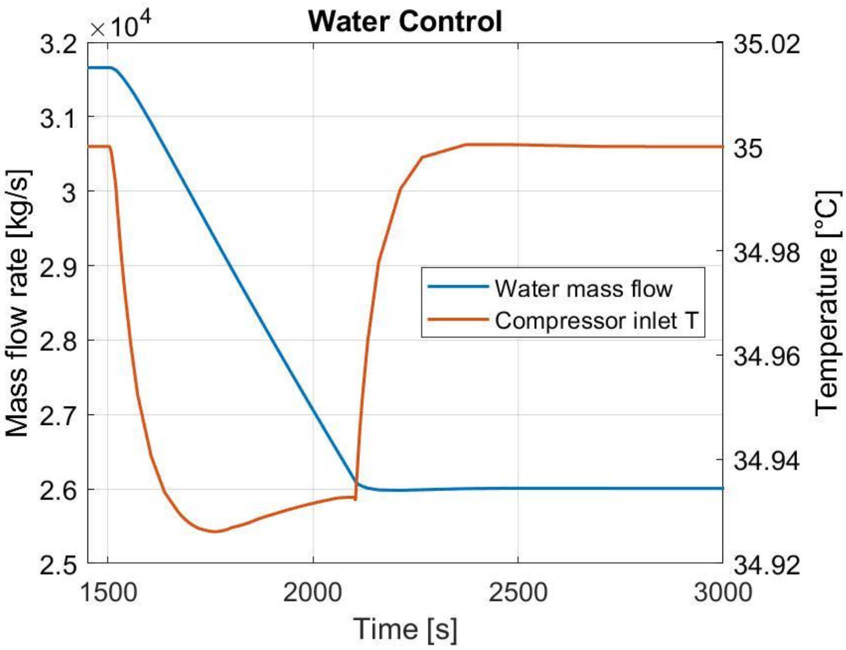

Figure 66 Water control system activity during the second part-load operation

To conclude, the strategy here presented reduced the plant operation at 80% of nominal power, by decreasing the opening factor till 5.76%. Both compressor's and turbine's powers are decreased due to the lower mass flow and pressure levels, while keeping high isentropic efficiencies, nominally 83.46% the compressor and 93% the turbine. The compressor power reduction is attributed to the new efficiency, higher than during nominal load, and lower mass flow rate; while for the turbine the decrease is attributed to the lower inlet pressure and mass flow, being operating almost with the same efficiency as at nominal load. Moreover, as mentioned before, thanks to the improved heat recovery of the HTR, also the heat introduced by the HTS is lower, which is part of the loop's efficiency formula. This led to relatively high cycle efficiency $\eta_{th} = 34.87\%$, only 2.5 percentage points lower the nominal load efficiency. The results explained in this section are summarized in Table 13.

Table 13 Results summary of the second part-load operation strategy

	Nominal Load	Partial Load	Relative Difference
CO_2 Mass Flow [kg/s]	6835.54	6189.23	-9.43%
Molten Salt Flow [kg/s]	6031.52	5348.36	-11.33%
Water Flow [kg/s]	31675.48	26006.48	-17.90%
Cycle Efficiency	37.39%	34.87%	-6.75%
Compressor Power [GW]	0.26	0.25	-4.58%
Turbine Power [GW]	1.01	0.85	-15.92%
HTR Power [GW]	2.15	2.04	-5.03%
HTS Power [GW]	1.98	1.70	-14.15%
PC Power [GW]	1.22	1.09	-10.61%
Total Pressure Drop CO2 [bar]	6.24	56.32	802.27%
Low Pressure Level [bar]	85.00	85.00	0.00%
High Pressure Level [bar]	306.17	326.73	6.72%
Minimum Temperature [°C]	35.00	35.00	0.00%
Maximum Temperature [°C]	490.00	490.00	0.00%
Valve Opening Factor	100%	5.763%	-94.24%

4.2.3 Discussion

Two part-load operation strategies have been modelled in Modelica, one operating on the Turbine Inlet Temperature, the other on the opening factor of a valve located between the compressor and recuperator. Both of the techniques proved to be effective, achieving a 20% reduction of the net power output, distributed in ten minutes.

The first strategy imposed almost 100°C of TIT reduction to achieve the desired plant operation. Consequence of the lower TIT, is the smaller enthalpy head exploitable by the turbine, translated into less power extracted by the device; whilst, the compressor would absorb almost the same power as during the nominal load operation, leading to a reduction in cycle's efficiency.

The second strategy focused on the valve opening, applying an additional pressure drop of 50.85 bar to the loop, consequently reducing the mass flow circulating. On the other hand, temperatures and low pressures remained almost unchanged thanks to the control systems' actions. All the components scaled down their activity with the lower mass flow rate, limiting the cycle efficiency loss.

After having tested them with the same initial and final conditions, the last technique led to higher efficiencies, both in single turbomachines and the entire cycle. It is noticeable that, in the second case, the increase of heat recovered and decrease of thermal power input are more consistent than the first strategy, leading to improvements in the cycle performances. Results prove what expected, confirming that the second strategy performs better; indeed, the thermal efficiency of the loop is almost 2.5% higher than in the TIT part-load operation and, for this reason, should be preferred. Table 14 and Figure 67 below summarize and compare the results of the two strategies.

Table 14 Partial load operation strategies results comparison

	Strategy 1	**Strategy 2**
Cycle efficiency	32.44%	34.87%
Load [% of nominal]	80.00%	80.00%
Compressor Efficiency	80.96%	83.46%
Turbine Efficiency	92.98%	93.01%
Compressor Power [GW]	0.26	0.25
Turbine Power [GW]	0.86	0.85
HTR Power [GW]	1.51	2.04
HTS Power [GW]	1.83	1.70
PC Power [GW]	1.22	1.09
Total Pressure Drop CO2 [bar]	5.36	56.32
Maximum Pressure [bar]	305.50	326.70
Maximum Temperature [°C]	397.54	490.00
Valve Opening Factor	100%	5.76%

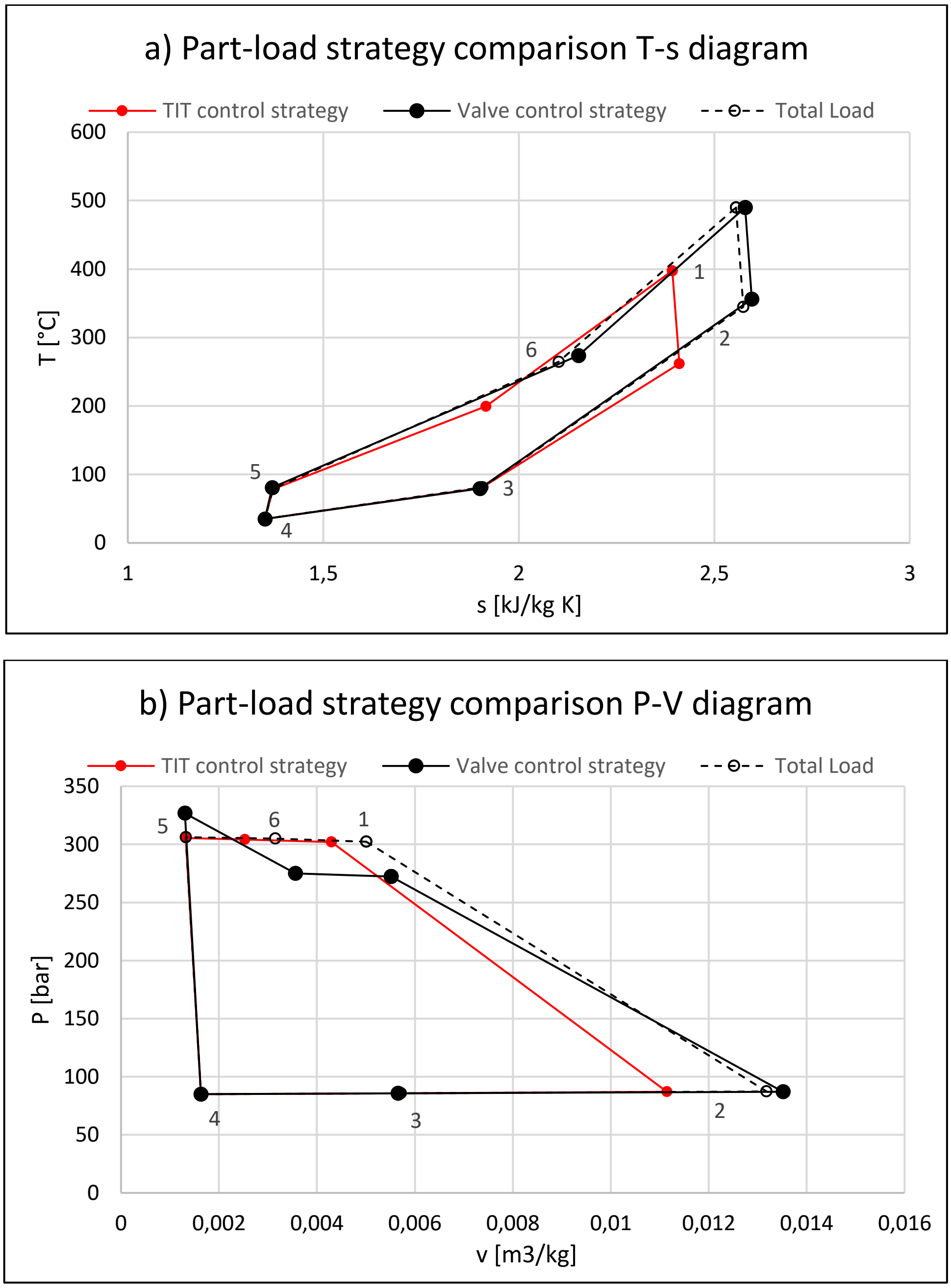

Figure 67 a) T-s and b) P-V diagram of the two part-load control strategies, benchmarked with the cycle running at nominal load (dashed lines)

5 Conclusions and Future Work

In this thesis work, a supercritical CO_2 Brayton power cycle for solar and nuclear applications have been modelled in Modelica, using the Dymola program. For its design, a sCO_2 loop made with the EES have been provided by the Comillas Pontificial University (Madrid, Spain) and used as reference.

The Modelica loop has first been tested in static conditions, with two different layout: the first was identical to the reference to be benchmarked with, in order to prove the solidity of the results and the code, but not including the presence of the pipes in between the different cycle components, meaning lower loop's volume and inertia. These pipes have been included in the second layout, together with a more precise evaluation of the pressure drops in the heat exchangers' connection, resulting in an improved and more realistic version of the first. In both cases, the results showed good agreement with the reference values, especially the first one, since provided with the same layout, while the second presents some differences related with the higher pressure losses and the relative effects.

The second more realistic layout has been further tested in dynamic simulations to, initially, insert controls in precise loop's points and, lastly, to define and test two different partial-load operation strategies. Three PIs have been inserted, acting respectively on the compressor inlet temperature, turbine inlet temperature and valve opening. The presence of the first controller sensibly improved the loop's performances, fixing the temperature at the compressor's nominal value, while the other two controllers were mainly useful in regard to the part-load operation.

Indeed, two strategies for the cycle's operation with partial power output have been simulated using the last two PIs; the first acts on the Turbine Inlet Temperature through the regulation of the molten salt mass flow, in order to reduce the turbine's power output, decreasing the fluid temperature at its inlet; the second regulates the valve opening, imposing an additional pressure drop, in order to decrease the CO_2 mass flow rate and with it the cycle power output, while keeping the temperatures along the loop almost unvaried, thanks to the controllers. The second strategy proved to perform better than the first, achieving the same results with higher performances, both in terms of cycle efficiency and turbomachinery isentropic efficiency.

To conclude, the model proved to be correctly designed with static results close to the reference values, as well as solid and stable against transients and dynamic conditions, being of interest for future applications, such as design of the plant's control strategies and integration with solar fields or nuclear reactors models. Although as mentioned in the text, the system contains some simplifications that could be improved with future work.

First of all, the loop's main weakness consist of the turbine component, which had been created from scratch and is operating with semi-realistic conditions, but the PR independence of the rotation speed and the non-influence of the inlet temperature on the device's performances is clearly a strong and imprecise approximation. Comillas University is currently working on a realistic turbine model, that will be further integrated with the present work. Moreover, the turbomachinery components are considered without inertia here, while real components of this size clearly would have a consistent mass and inertia, that would make the system respond differently to transient conditions.

Secondly, the pressure drops' computation in the heat exchangers' connections could be improved; indeed, they have been considered lumped at the components' inlet here, set with appropriate values obtained by tests at nominal conditions. Future designs could enhance their evaluation, integrating all the connection components in the heat exchanger model, to perform a more precise simulation. Moreover, the friction related to the pipes in between the different components is included in these lumped pressure drops, due to their small entity; thus, it could be evaluated directly in the pipes as it has been done for the heat exchangers' microchannels, for more precise results.

The heat exchangers' design proved to be successful and to work with performances very close to the reference. However, the one proposed is a simplified version of the complicated PCHE's layout. More detailed designs could account for the semi-circular shape or the inlet/outlet bends of the microchannels, that could influence the heat exchange.

Furthermore, the expansion vessel used here has ideal capacity, being able to accept and release infinite flow rate, always maintaining the same pressure and remaining connected to the loop. A more realistic pressure control could be made of a tank with limited capacity, connected through a valve with a defined hysteresis, to control its aperture more smoothly.

Finally, another possible improvement could be the integration of the HITEC molten salt in Modelica, since solar salts have been considered in the heat source here.

Appendix A: Modelling tool

Modelica is an open-source, object-oriented modelling language for complex cyber physical systems, released for the first time in 1997 by Hilding Elmqvist. After three years, in 2000, the Modelica Association born with the purpose to stimulate the development of the language and the creation of its standard library (Modelica Association, 2017). An increasing variety of simulation tools are appearing, all based on the same equation-based high-level code, just recompiling it depending on the environment used. Thanks to this, the language's development has been guaranteed, since it is not tied to any specific tool. The one used in this thesis work is Dymola, a commercial simulation environment based on Modelica, initially based on the homonym Dymola language and created by Hilding Elmqvist in 1978, now released by Dassault Systèmes (Elmqvist, 2014).

The object-oriented nature and a-causal modelling, based on differential algebraic equations (DAEs), confer high stability, flexibility and, therefore, wide spectrum of applications, making it a multi-domain modelling language able to manage easily different systems such as electrical, mechanical, thermodynamic, hydraulic, biological, control, event, real-time. Building such systems is simplified by the presence of a GUI, since components can be assembled in graphic diagrams, easier to follow and manage. Many solvers are integrated to solve the sets of DAEs, the most widely used is the DASSL algorithm, utilized also in the present case (Casella, 2011).

Moreover, one of Modelica's strengths points is the wide availability of open-source and commercial libraries, where components for specific fields are grouped together. Sharing this type of modelling knowledge concretely lightens the researcher's fatigue, allowing to re-use components and systems built by other colleagues all over the world already. The Modelica Association provides already the Modelica Standard Library (MSL), with models for all the main applications. In the present work a huge contribution came from three other libraries:

- ThermoPower library: developed by Francesco Casella, from Politecnico di Milano (Italy). It contains all the main mechanical and thermal components for water and gas applications in thermal power plants and systems for energy conversion (Tiller et al., December 3, 2). This served as a base for the development of all the loop's elements and heat transfer components, eventually edited and upgraded depending on the specific use required.

- ExternalMedia and FluidProp: respectively, a modelica library, extending the *Modelica.Media* library with an interface to communicate with FluidProp. FluidProp is a software for the estimation of fluids' thermophysical properties, with 5 different databases. The one of interest in this case is RefProp, containing the NIST database of refrigerants and organic fluids. They provided the CO_2 at supercritical state as medium (Casella and Richter, 2010).
- SolarTherm: library built by the Australian Solar Thermal Research Institute (ASTRI) for simulation of CSP applications (Alberto de la Calle et al., 2018), containing components and several control strategies specific for this purpose. Here it was used for the definition of molten salt as medium. Although, initially some problems arose with the utilization of this medium, solved with the definition of a new type class of temperature. Moreover, the pipes from ThermoPower need the values of the density derivative respect to the enthalpy at constant pressure, absent in the SolarTherm library, and therefore manually inserted after a literature research.

Appendix B: Turbomachinery manipulation process

Compressor

As mentioned in the Section 2.1.1.1.1, the compressor set with the original inlet design parameters was not able to provide the same pressure ratio as the reference ideal model (Table B. 1). In order to reach the desired pressure head, those parameters have been modified.

Table B. 1 Compressor original inlet rated design parameters

Inlet Design Parameters		
$\boldsymbol{\rho}$	617.6	[Kg/m3]
$\boldsymbol{a}$	238.15	[m/s]
N	3000.00	[rpm]
$\dot{\boldsymbol{m}}$	6912	[kg/s]

According to Comillas' cycle data, the compressor, rotating at the nominal speed, should be able to increase the pressure of 6912 kg/s CO_2 flow from 85 bar to 300.8 bar, providing $PR = {}^{300.8}/_{85} = 3.5388$.

The inlet conditions of the fluid are 35°C and 85 bar, therefore, according to the NIST values, with density $\rho = 612.12\,\frac{kg}{m^3}$ and sound of speed $a = 235.06\,\frac{m}{s}$. These results in $\nu = 1.0222$ and $\alpha = 1.0131$, which return $PR = 3.6795$ from the performance tables, 4% higher than the predicted value.

For this reason, it appears that the component design was not perfect, and needed to be adjusted in order to perform as expected. A possible solution was found in changing the design inlet parameters, in order to obtain the desired PR value at the nominal mass flow rate of Comillas' cycle (6912 kg/s). Firstly, since those parameters were close, but not the same as the ones derived from the NIST database, was supposed an error in their computation and, therefore, reset with the ones showed above.

Consequently, running the device at the nominal velocity (3000 rpm), a relative speed α equal to 1 will be now obtained. At fixed $\alpha = 1$, through an interpolation of the values provided, it is possible to find the value of relative mass flow, which returns the researched PR, $\nu(PR = 3.5388) = 1.0282$.

:

Finally, it is possible to derive the new design mass flow, which gives the desired pressure ratio with 6912 kg/s, $\dot{m}_{rated} = \frac{6912}{1.0282} = 6722.44 \frac{kg}{s}$.

Now, being the inlet conditions equal to the designs, except for the mass flow rate, it is possible to reach a pressure ratio of 3.5388 with 6912 kg/s, at 35°C and 85 bar. The modified parameters are listed in Table B. 2.

Table B. 2 Modified compressor rated inlet parameters

New Inlet Design Conditions		
$\boldsymbol{\rho}$	612.12	[Kg/m3]
$\boldsymbol{a}$	235.06	[m/s]
N	3000.00	[rpm]
$\dot{\boldsymbol{m}}$	6764.30	[kg/s]

Turbine

The turbine model provided in the ThermoPower, tested with nominal inlet conditions, was not able to provide the appropriate values of pressure ratio and efficiency; therefore, the performance maps, function of mass flow rate and rotational speed, have been manipulated in order to achieve the desired target values, $PR_d = 3.4965$ and $\eta = 93\%$.

Starting from the pressure ratio, to impose the wanted PR with mass flow 6912 kg/s, the pressure ratio curve has been tilted by multiplying the mass flow rate values with a correction factor α, while keeping the PR y-axis values fixed. As first step, it has been found the mass flow rate values returning PR_d: $\dot{m}_{old}(PR_d) = 5159.32 \frac{kg}{s}$. Then α could be obtained as ratio between the design value 6912 kg/s and the so-found mass flow rate: $\alpha = \frac{\dot{m}_{des}}{\dot{m}_{old}} = \frac{6912}{5159.32} = 1.3397$.

All the x-values of the PR curve, corresponding to the mass flow rates, have been multiplied by this correction factor, resulting in tilting the PR curve towards the x-axis. Thus, the turbine is now able to address the desired PR value with 6912 kg/s of CO_2. In Figure B. 1 is shown the modification of the curve. The dashed red line represents the desired PR and indicates the intersection with the curves.

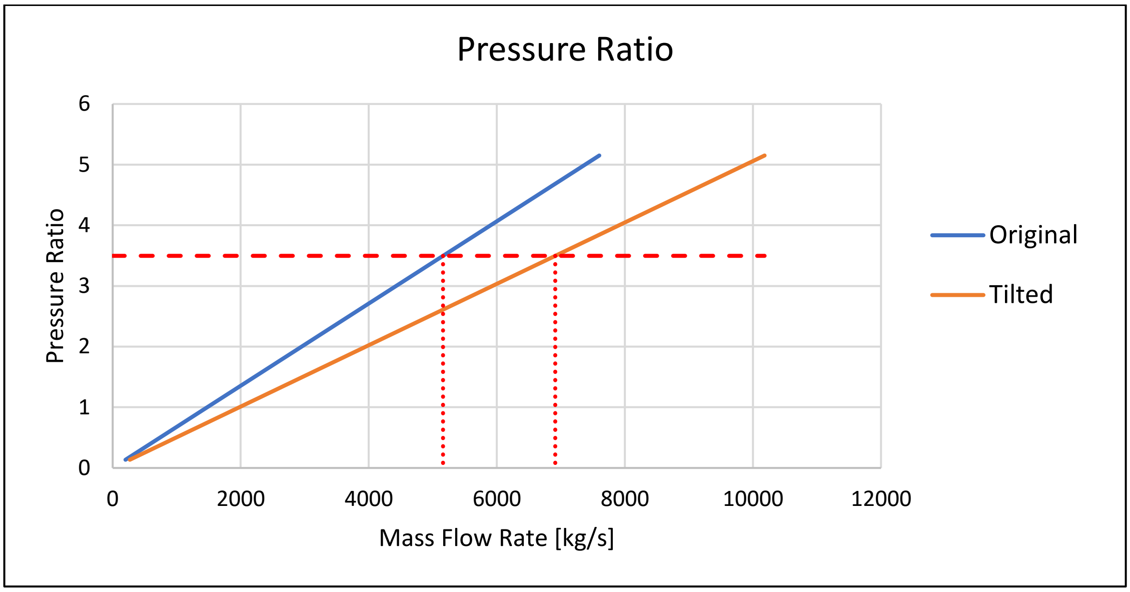

Figure B. 1 Modified turbine pressure ratio curve

Finally, the equation representing the tilted curve was extracted (Equation (9)).

Similarly, also the efficiency curves have been manipulated to reach the performances requested. Firstly, the same procedure of the PR was applied, multiplying the mass flow values for the same α correction factor, in order to widen the curves, in the same way as done for the pressure ratio. This is reflected in their dilatation towards the positive direction of the x-axis, since, again, the y-values are kept constant and the x-values are multiplied by a positive factor (Figure B. 2).

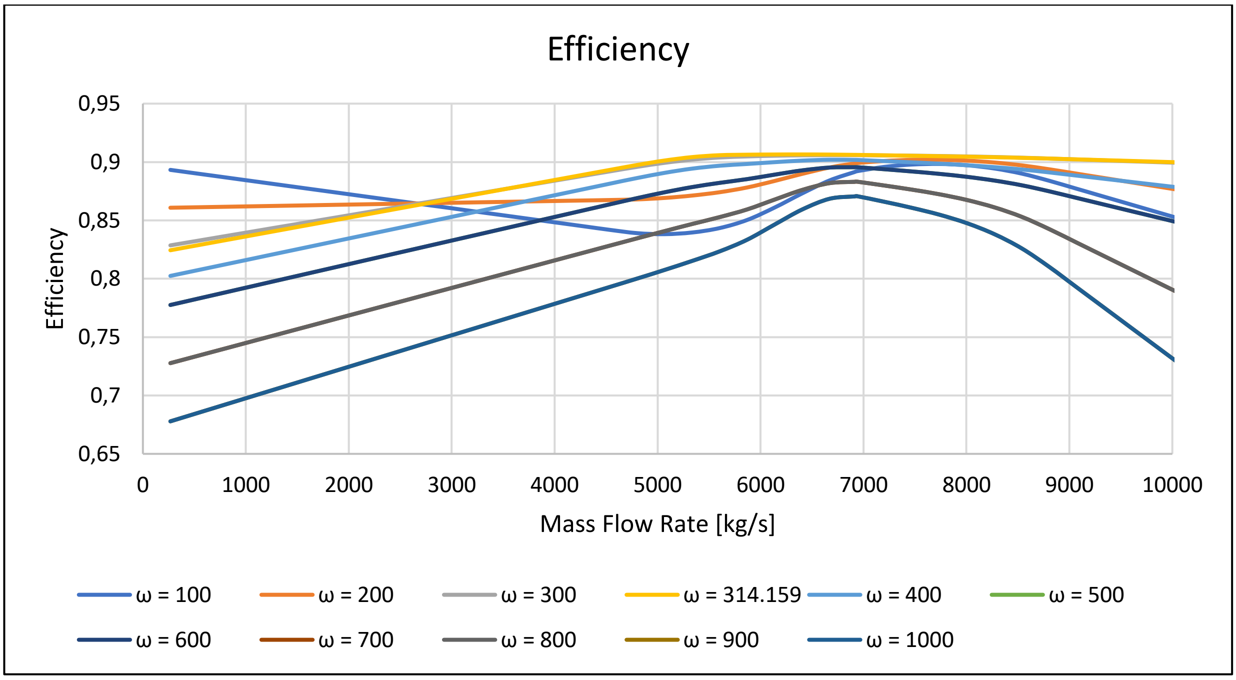

Figure B. 2 First manipulation of turbine efficiency maps

However, the maximum efficiency is still smaller than the one sought, reaching $\eta = 0.9061$ with 6912 kg/s and rotating at 3000 rpm. Therefore, another modification is required: this time, all y-values are multiplied by a further correction factor β, causing a dilatation in the positive y direction. β is computed as ratio between the target efficiency and the value obtained, in order to guarantee the achievement of the correct efficiency at $\omega = 314.159 \frac{rad}{s} = 3000\ rpm$ and 6912 kg/s: $\beta = \frac{\eta_d}{\eta_{actual}} = \frac{0.93}{0.9061} = 1.0261$

Now the component will be in the conditions to reach both the desired efficiency and pressure ratio. In Figure B. 3 the last manipulation of the efficiency curves is represented.

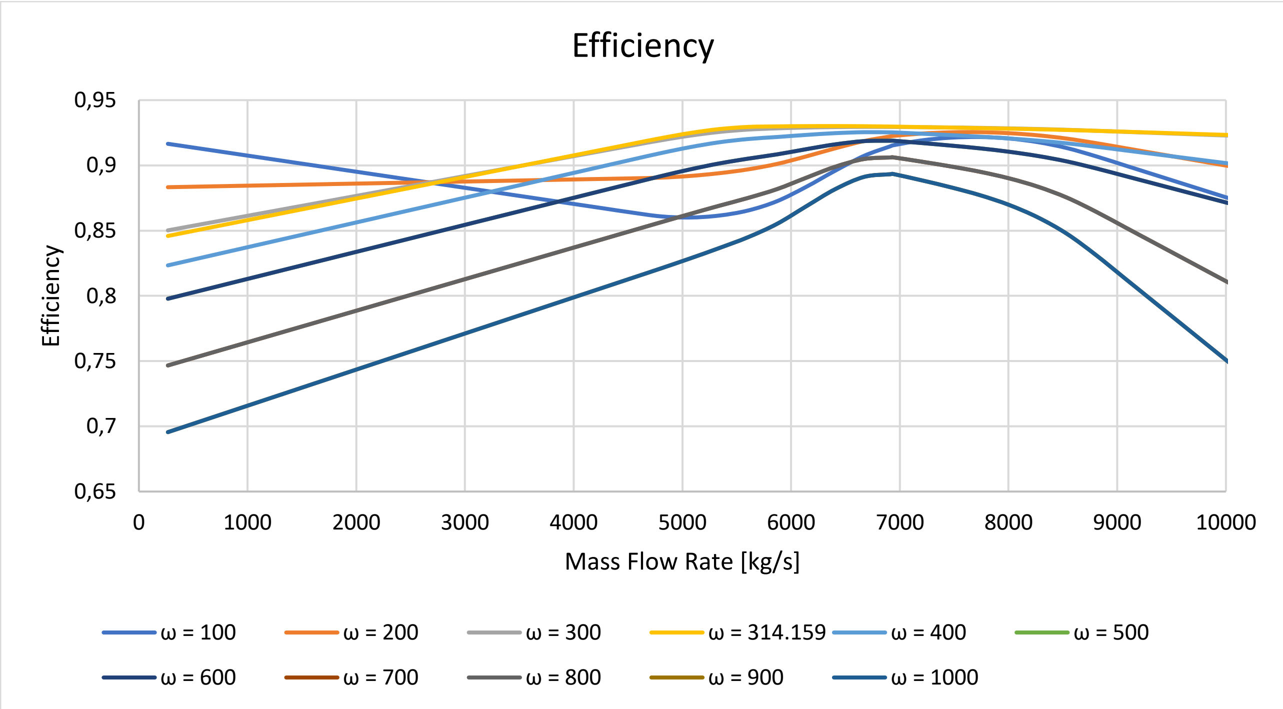

Figure B. 3 Second manipulation of turbine efficiency map

Appendix C: Turbomachinery parameters

The present section contains all the tables and parameters that have been relevant in the design of the turbomachinery models. Table C. 1 provides the flow number *Phic* and referred speed N_T formulations used in the ThermoPower compressor model.

Table C. 1 ThermoPower Compressor formulae. Tin and Pin are the inlet temperature [K] and pressure [Pa], Tdes,in the design inlet temperature [K], Ndes design angular velocity [rad/s], ω the angular speed [rad/s], w is the mass flow [kg/s]

ThermoPower Compressor Formulae
$\boldsymbol{Phic = w \cdot \frac{\sqrt{T_{in}}}{P_{in}}}$
$\boldsymbol{N_T = \frac{100\ \omega \cdot \sqrt{T_{des,in}}}{\sqrt{T_{in}} \cdot N_{des}}}$

Table C. 2 contains the compressor performance maps provided by Comillas University, as function of the relative mass flow rate and speed. Furthermore, Table C. 3 and Table C. 4 show the values of the extended performances tables that have been provided to the Modelica model, respectively the efficiency and pressure ratio tables.

Regarding the turbine model, in Table C. 5 and Table C. 6 are listed the values of the efficiency map before and after the manipulation, as function of mass flow rate and velocity.

Table C. 2 Compressor Performance Tables

Compressor Performance Tables			
n	**PR**	**Efficiency**	**a**
0.05	1.027578	0.7840576	0.1
0.06	1.027802	0.8198755	0.1
0.07	1.027191	0.8420848	0.1
0.08	1.02569	0.8455106	0.1
0.09	1.023697	0.8299693	0.1
0.1	1.021468	0.7981319	0.1
0.11	1.019142	0.7547925	0.1
0.12	1.016722	0.7000049	0.1
0.15	1.253448	0.7823251	0.3
0.18	1.255735	0.8181782	0.3
0.21	1.251223	0.8419853	0.3
0.24	1.237741	0.847165	0.3
0.27	1.219641	0.8338082	0.3
0.3	1.198879	0.8026195	0.3
0.33	1.177048	0.7592288	0.3
0.36	1.154252	0.7038655	0.3
0.25	1.725075	0.7771563	0.5
0.3	1.732656	0.8131808	0.5
0.35	1.7248	0.839196	0.5
0.4	1.687766	0.8469143	0.5
0.45	1.637199	0.8368302	0.5
0.5	1.577607	0.8078655	0.5
0.55	1.513364	0.7648447	0.5
0.6	1.445717	0.7089526	0.5
0.35	2.468191	0.7711604	0.7
0.42	2.485599	0.8072899	0.7
0.49	2.481056	0.835286	0.7
0.56	2.409431	0.845423	0.7
0.63	2.309953	0.8386093	0.7
0.7	2.191058	0.8132161	0.7
0.77	2.057242	0.7708491	0.7
0.84	1.914683	0.714607	0.7
0.45	3.507652	0.7652436	0.9
0.54	3.540358	0.801389	0.9
0.63	3.551579	0.8309139	0.9
0.72	3.434162	0.8430339	0.9
0.81	3.268801	0.8390316	0.9
0.9	3.069371	0.8172265	0.9
0.99	2.835638	0.7763267	0.9
1.08	2.606894	0.7252156	0.9
0.5	4.145606	0.762412	1
0.6	4.188212	0.7985381	1
0.7	4.209171	0.8284498	1
0.8	4.06857	0.8415909	1
0.9	3.863313	0.8387915	1
1	3.614009	0.8185741	1
1.1	3.347366	0.7824067	1
1.2	2.98184	0.717989	1
0.6	5.67081	0.7570705	1.2
0.72	5.737915	0.7931192	1.2
0.84	5.773908	0.8232309	1.2
0.96	5.5941	0.838393	1.2
1.08	5.320398	0.8391705	1.2
1.2	4.918386	0.8176807	1.2
1.32	4.46842	0.7791909	1.2

Table C. 3 Compressor efficiency table extended

Efficiency Table Extended							
				α			
v	**0.10000**	**0.30000**	**0.50000**	**0.70000**	**0.90000**	**1.00000**	**1.20000**
0.05000	0.78298	0.50350	0.44674	0.40271	0.37960	0.34969	0.35113
0.06000	0.82217	0.54194	0.46957	0.41980	0.39302	0.36243	0.36139
0.07000	0.84201	0.57792	0.49173	0.43656	0.40625	0.37500	0.37154
0.08000	0.84389	0.61146	0.51322	0.45298	0.41928	0.38740	0.38158
0.09000	0.82917	0.64261	0.53403	0.46906	0.43212	0.39964	0.39151
0.10000	0.79926	0.67140	0.55417	0.48480	0.44476	0.41171	0.40134
0.11000	0.75553	0.69786	0.57364	0.50021	0.45719	0.42362	0.41105
0.12000	0.69937	0.72202	0.59244	0.51527	0.46944	0.43535	0.42066
0.15000	0.47013	0.78110	0.64481	0.55846	0.50498	0.46957	0.44882
0.18000	0.17882	0.82076	0.69112	0.59861	0.53874	0.50229	0.47600
0.21000	0.00001	0.84195	0.73139	0.63573	0.57072	0.53350	0.50220
0.24000	0.00001	0.84557	0.76560	0.66982	0.60093	0.56322	0.52741
0.27000	0.00001	0.83257	0.79377	0.70087	0.62936	0.59144	0.55165
0.30000	0.00001	0.80387	0.81589	0.72889	0.65602	0.61816	0.57490
0.33000	0.00001	0.76038	0.83195	0.75388	0.68089	0.64338	0.59717
0.36000	0.00001	0.70305	0.84197	0.77583	0.70399	0.66710	0.61847
0.40000	0.00001	0.60667	0.84592	0.80038	0.73202	0.69640	0.64533
0.45000	0.00001	0.45724	0.83574	0.82349	0.76262	0.72927	0.67645
0.50000	0.00001	0.27963	0.80875	0.83818	0.78828	0.75798	0.70485
0.55000	0.00001	0.07813	0.76496	0.84443	0.80900	0.78252	0.73052
0.60000	0.00001	0.00001	0.70436	0.84226	0.82478	0.80290	0.75347
0.63000	0.00001	0.00001	0.65994	0.83692	0.83188	0.81312	0.76593
0.70000	0.00001	0.00001	0.53277	0.81265	0.84154	0.83116	0.79118
0.77000	0.00001	0.00001	0.37266	0.77187	0.84151	0.84103	0.81109
0.84000	0.00001	0.00001	0.17961	0.71457	0.83181	0.84274	0.82566
0.90000	0.00001	0.00001	0.00001	0.65232	0.81580	0.83771	0.83390
0.99000	0.00001	0.00001	0.00001	0.53619	0.77844	0.81892	0.83889
1.08000	0.00001	0.00001	0.00001	0.39276	0.72508	0.78664	0.83505
1.10000	0.00001	0.00001	0.00001	0.35718	0.71106	0.77763	0.83300
1.20000	0.00001	0.00001	0.00001	0.15906	0.62906	0.72260	0.81619
1.32000	0.00001	0.00001	0.00001	0.00001	0.50460	0.63458	0.78163

Table C. 4 Compressor pressure ratio table extended

Pressure Ratio Table Extended							
				α			
ν	**0.10000**	**0.30000**	**0.50000**	**0.70000**	**0.90000**	**1.00000**	**1.20000**
0.05000	1.02797	1.23476	1.56967	2.14941	2.86232	3.17441	3.73703
0.06000	1.02760	1.23903	1.58348	2.16888	2.89101	3.21129	3.79433
0.07000	1.02681	1.24282	1.59668	2.18778	2.91909	3.24750	3.85081
0.08000	1.02558	1.24616	1.60926	2.20610	2.94654	3.28302	3.90648
0.09000	1.02394	1.24903	1.62123	2.22384	2.97338	3.31787	3.96132
0.10000	1.02186	1.25144	1.63258	2.24099	2.99961	3.35204	4.01534
0.11000	1.01936	1.25338	1.64332	2.25757	3.02521	3.38554	4.06854
0.12000	1.01643	1.25486	1.65345	2.27356	3.05020	3.41835	4.12092
0.15000	1.00508	1.25652	1.68014	2.31806	3.12146	3.51271	4.27314
0.18000	1.00000	1.25400	1.70131	2.35733	3.18717	3.60097	4.41797
0.21000	1.00000	1.24731	1.71695	2.39138	3.24732	3.68312	4.55541
0.24000	1.00000	1.23645	1.72706	2.42020	3.30192	3.75916	4.68547
0.27000	1.00000	1.22142	1.73164	2.44379	3.35096	3.82909	4.80814
0.30000	1.00000	1.20221	1.73070	2.46216	3.39444	3.89292	4.92343
0.33000	1.00000	1.17883	1.72423	2.47530	3.43237	3.95063	5.03133
0.36000	1.00000	1.15128	1.71223	2.48321	3.46475	4.00224	5.13185
0.40000	1.00000	1.10805	1.68763	2.48563	3.49927	4.06154	5.25438
0.45000	1.00000	1.04358	1.64307	2.47559	3.52854	4.12041	5.38909
0.50000	1.00000	1.00000	1.58315	2.45103	3.54238	4.16230	5.50328
0.55000	1.00000	1.00000	1.50788	2.41195	3.54078	4.18723	5.59695
0.60000	1.00000	1.00000	1.41725	2.35835	3.52375	4.19518	5.67010
0.63000	1.00000	1.00000	1.35551	2.31922	3.50613	4.19181	5.70415
0.70000	1.00000	1.00000	1.18994	2.20760	3.44340	4.16020	5.75487
0.77000	1.00000	1.00000	1.00000	2.06752	3.35043	4.09532	5.76538
0.84000	1.00000	1.00000	1.00000	1.89898	3.22721	3.99719	5.73568
0.90000	1.00000	1.00000	1.00000	1.73187	3.09753	3.88660	5.67822
0.99000	1.00000	1.00000	1.00000	1.44201	2.86133	3.67491	5.53663
1.08000	1.00000	1.00000	1.00000	1.10511	2.57514	3.40825	5.32858
1.10000	1.00000	1.00000	1.00000	1.02385	2.50475	3.34152	5.27332
1.20000	1.00000	1.00000	1.00000	1.00000	2.11577	2.96718	4.94778
1.32000	1.00000	1.00000	1.00000	1.00000	1.56751	2.42837	4.44880

Table C. 5 Original turbine efficiency table

Original Turbine Efficiency Tables											
$\dot{m}$ [kg/s]	Ω [rad/s]										
	100	**200**	**300**	**314.159**	**400**	**500**	**600**	**700**	**800**	**900**	**1000**
200	0.89325	0.860834	0.828595	0.824416	0.802439	0.777523	0.777523	0.72769	0.72769	0.677858	0.677858
400	0.890039	0.861247	0.832556	0.828717	0.807376	0.782912	0.782912	0.733982	0.733982	0.685053	0.685053
600	0.886829	0.86166	0.836518	0.833018	0.812314	0.788301	0.788301	0.740274	0.740274	0.692248	0.692248
800	0.883618	0.862073	0.84048	0.837319	0.817251	0.79369	0.79369	0.746566	0.746566	0.699442	0.699442
1000	0.880407	0.862486	0.844442	0.841619	0.822189	0.799079	0.799079	0.752858	0.752858	0.706637	0.706637
1200	0.877196	0.862899	0.848403	0.84592	0.827126	0.804467	0.804467	0.75915	0.75915	0.713832	0.713832
1400	0.873986	0.863312	0.852365	0.850221	0.832064	0.809856	0.809856	0.765442	0.765442	0.721027	0.721027
1600	0.870775	0.863725	0.856327	0.854522	0.837001	0.815245	0.815245	0.771733	0.771733	0.728222	0.728222
1800	0.867564	0.864138	0.860288	0.858823	0.841939	0.820634	0.820634	0.778025	0.778025	0.735416	0.735416
2000	0.864353	0.864551	0.86425	0.863124	0.846876	0.826023	0.826023	0.784317	0.784317	0.742611	0.742611
2200	0.861143	0.864964	0.868212	0.867424	0.851814	0.831412	0.831412	0.790609	0.790609	0.749806	0.749806
2400	0.857932	0.865377	0.872173	0.871725	0.856751	0.836801	0.836801	0.796901	0.796901	0.757001	0.757001
2600	0.854721	0.86579	0.876135	0.876026	0.861689	0.84219	0.84219	0.803193	0.803193	0.764195	0.764195
2800	0.85151	0.866203	0.880097	0.880327	0.866627	0.847579	0.847579	0.809485	0.809485	0.77139	0.77139
3000	0.8483	0.866617	0.884059	0.884628	0.871564	0.852968	0.852968	0.815777	0.815777	0.778585	0.778585
3200	0.845089	0.86703	0.88802	0.888929	0.876502	0.858357	0.858357	0.822068	0.822068	0.78578	0.78578
3400	0.841878	0.867443	0.891982	0.893229	0.881439	0.863746	0.863746	0.82836	0.82836	0.792974	0.792974
3600	0.839038	0.867986	0.895879	0.897481	0.886317	0.869092	0.869092	0.834642	0.834642	0.800192	0.800192
3800	0.838197	0.869229	0.899334	0.90129	0.890741	0.874111	0.874111	0.84085	0.84085	0.807589	0.807589
4000	0.839628	0.871268	0.902083	0.904221	0.894352	0.878543	0.878543	0.846923	0.846923	0.815304	0.815304
4200	0.843421	0.874135	0.903888	0.905848	0.896812	0.882144	0.882144	0.852808	0.852808	0.823472	0.823472
4400	0.850369	0.878204	0.904796	0.906249	0.898325	0.885347	0.885347	0.859392	0.859392	0.833436	0.833436
4600	0.861006	0.883775	0.905395	0.906445	0.899877	0.889194	0.889194	0.867826	0.867826	0.846459	0.846459
4800	0.87308	0.88983	0.905747	0.906485	0.901193	0.892813	0.892813	0.876052	0.876052	0.859292	0.859292
5000	0.884237	0.895303	0.905883	0.906369	0.901937	0.895253	0.895253	0.881887	0.881887	0.86852	0.86852
5200	0.892122	0.899129	0.905836	0.906098	0.901773	0.895564	0.895564	0.883146	0.883146	0.870728	0.870728
5400	0.895823	0.90091	0.905663	0.90572	0.900764	0.893791	0.893791	0.879846	0.879846	0.865901	0.865901
5600	0.897849	0.901821	0.905436	0.90535	0.899713	0.891914	0.891914	0.876315	0.876315	0.860717	0.860717
5800	0.898322	0.901918	0.905142	0.904972	0.89857	0.889828	0.889828	0.872343	0.872343	0.854858	0.854858
6000	0.897203	0.901179	0.904766	0.904564	0.897235	0.887307	0.887307	0.867451	0.867451	0.847594	0.847594
6200	0.894451	0.899583	0.904289	0.904104	0.895607	0.884125	0.884125	0.861161	0.861161	0.838197	0.838197
6400	0.890028	0.897111	0.903696	0.903568	0.893588	0.880057	0.880057	0.852997	0.852997	0.825936	0.825936
6600	0.883901	0.893744	0.90297	0.902936	0.891079	0.874883	0.874883	0.842493	0.842493	0.810102	0.810102
6800	0.877063	0.890004	0.902185	0.902258	0.888343	0.869198	0.869198	0.830906	0.830906	0.792615	0.792615
6912	0.873233	0.887910	0.901745	0.901878	0.88681	0.866013	0.866013	0.824417	0.824417	0.782822	0.782822
7000	0.870225	0.886265	0.901401	0.90158	0.885608	0.863512	0.863512	0.819320	0.81932	0.775128	0.775128
7200	0.863387	0.882525	0.900616	0.900903	0.882873	0.857827	0.857827	0.807734	0.807734	0.757642	0.757642
7400	0.856549	0.878785	0.899831	0.900225	0.880138	0.852141	0.852141	0.796148	0.796148	0.740155	0.740155
7600	0.849711	0.875046	0.899047	0.899547	0.877402	0.846456	0.846456	0.784562	0.784562	0.722668	0.722668

Table C. 6 Manipulated of the turbine efficiency table

Modified Turbine Efficiency Table											
$\dot{m}$ [kg/s]	Ω [rad/s]										
	100	**200**	**300**	**314.159**	**400**	**500**	**600**	**700**	**800**	**900**	**1000**
266.8	0.916541	0.883280	0.850201	0.845913	0.823363	0.797797	0.797797	0.746664	0.746664	0.695533	0.695533
533.6	0.913247	0.883704	0.854265	0.850326	0.828428	0.803326	0.803326	0.753121	0.753121	0.702916	0.702916
800.5	0.909953	0.884128	0.858330	0.854739	0.833495	0.808856	0.808856	0.759577	0.759577	0.710298	0.710298
1067.3	0.906658	0.884552	0.862395	0.859152	0.838561	0.814385	0.814385	0.766033	0.766033	0.717680	0.717680
1334.1	0.903364	0.884975	0.866461	0.863564	0.843628	0.819915	0.819915	0.772489	0.772489	0.725063	0.725063
1600.9	0.900069	0.885399	0.870525	0.867977	0.848693	0.825443	0.825443	0.778945	0.778945	0.732445	0.732445
1867.8	0.896775	0.885823	0.874590	0.872390	0.853760	0.830973	0.830973	0.785401	0.785401	0.739828	0.739828
2134.6	0.893480	0.886247	0.878656	0.876804	0.858826	0.836502	0.836502	0.791856	0.791856	0.747210	0.747210
2401.4	0.890186	0.886670	0.882720	0.881217	0.863893	0.842032	0.842032	0.798312	0.798312	0.754592	0.754592
2668.2	0.886891	0.887094	0.886785	0.885630	0.868958	0.847562	0.847562	0.804768	0.804768	0.761975	0.761975
2935.1	0.883597	0.887518	0.890851	0.890042	0.874025	0.853091	0.853091	0.811224	0.811224	0.769357	0.769357
3201.9	0.880303	0.887942	0.894915	0.894455	0.879091	0.858621	0.858621	0.817680	0.817680	0.776740	0.776740
3468.7	0.877008	0.888365	0.898980	0.898868	0.884158	0.864150	0.864150	0.824136	0.824136	0.784121	0.784121
3735.5	0.873713	0.888789	0.903046	0.903282	0.889224	0.869680	0.869680	0.830592	0.830592	0.791504	0.791504
4002.4	0.870419	0.889214	0.907111	0.907695	0.894290	0.875209	0.875209	0.837048	0.837048	0.798887	0.798887
4269.2	0.867125	0.889638	0.911175	0.912108	0.899357	0.880739	0.880739	0.843503	0.843503	0.806269	0.806269
4536.0	0.863830	0.890062	0.915240	0.916520	0.904422	0.886268	0.886268	0.849959	0.849959	0.813651	0.813651
4802.8	0.860916	0.890619	0.919239	0.920883	0.909428	0.891754	0.891754	0.856405	0.856405	0.821057	0.821057
5069.7	0.860053	0.891894	0.922784	0.924791	0.913967	0.896903	0.896903	0.862775	0.862775	0.828647	0.828647
5336.5	0.861521	0.893986	0.925605	0.927799	0.917672	0.901451	0.901451	0.869006	0.869006	0.836563	0.836563
5603.3	0.865413	0.896928	0.927457	0.929468	0.920196	0.905146	0.905146	0.875045	0.875045	0.844944	0.844944
5870.1	0.872542	0.901103	0.928389	0.929879	0.921749	0.908432	0.908432	0.881801	0.881801	0.855168	0.855168
6137.0	0.883457	0.906819	0.929003	0.930081	0.923341	0.912380	0.912380	0.890455	0.890455	0.868530	0.868530
6403.8	0.895846	0.913032	0.929364	0.930122	0.924692	0.916093	0.916093	0.898895	0.898895	0.881698	0.881698
6670.6	0.907293	0.918648	0.929504	0.930003	0.925455	0.918597	0.918597	0.904882	0.904882	0.891167	0.891167
6912.0	0.914613	0.922199	0.929460	0.929751	0.925303	0.918885	0.918885	0.906051	0.906051	0.893216	0.893216
6937.4	0.915384	0.922574	0.929456	0.929724	0.925287	0.918916	0.918916	0.906174	0.906174	0.893432	0.893432
7204.3	0.919182	0.924401	0.929278	0.929337	0.924251	0.917097	0.917097	0.902788	0.902788	0.888479	0.888479
7471.1	0.921260	0.925336	0.929045	0.928957	0.923173	0.915171	0.915171	0.899165	0.899165	0.883160	0.883160
7737.9	0.921746	0.925435	0.928744	0.928569	0.922000	0.913030	0.913030	0.895089	0.895089	0.877148	0.877148
8004.7	0.920598	0.924677	0.928358	0.928150	0.920630	0.910444	0.910444	0.890070	0.890070	0.869695	0.869695
8271.6	0.917774	0.923040	0.927868	0.927678	0.918960	0.907179	0.907179	0.883616	0.883616	0.860053	0.860053
8538.4	0.913235	0.920503	0.927260	0.927129	0.916888	0.903004	0.903004	0.875239	0.875239	0.847472	0.847472
8805.2	0.906949	0.917048	0.926515	0.926480	0.914314	0.897696	0.897696	0.864461	0.864461	0.831225	0.831225
9072.0	0.899932	0.913211	0.925709	0.925784	0.911507	0.891862	0.891862	0.852572	0.852572	0.813282	0.813282
9221.5	0.896003	0.911062	0.925259	0.925395	0.909935	0.888595	0.888595	0.845915	0.845915	0.803234	0.803234
9338.9	0.892916	0.909374	0.924905	0.925089	0.908700	0.886028	0.886028	0.840684	0.840684	0.795339	0.795339
9605.7	0.885900	0.905537	0.924100	0.924394	0.905894	0.880195	0.880195	0.828796	0.828796	0.777397	0.777397
9872.5	0.878883	0.901699	0.923294	0.923698	0.903088	0.874361	0.874361	0.816908	0.816908	0.759455	0.759455
10139.3	0.871867	0.897863	0.922490	0.923003	0.900280	0.868527	0.868527	0.805019	0.805019	0.741512	0.741512

Appendix D: Heat exchangers parameters

This last appendix summarizes the heat exchangers configuration and parameters. Figure D. 1 shows the schemes of the HXs arrangements and connections, while Table D. 1 provides the technical details of their inner components.

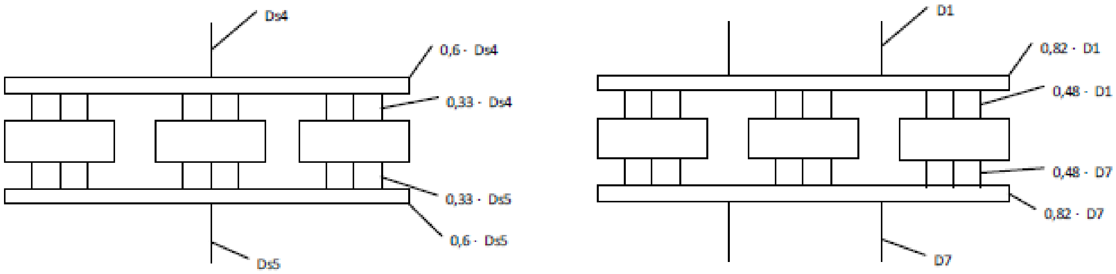

Figure AIII-2. Arrangement and connections of HTS.

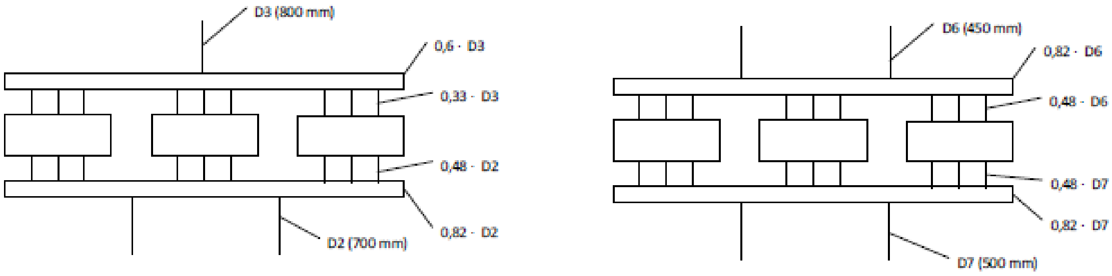

Figure AIII-3. Arrangement and connections of HTR.

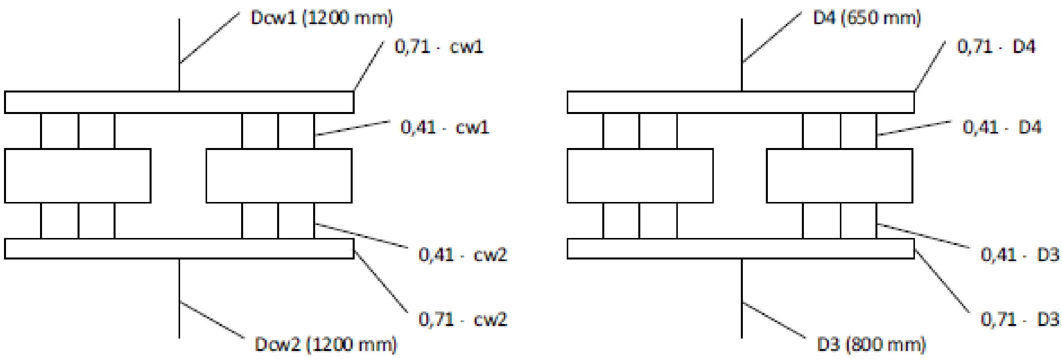

Fig AIII-4. Arrangement and connections of PC.

Figure D. 1 Heat exchangers arrangements and connections

Table D. 1 Heat exchanger connections and manifolds details

Set		Dh [m]	Length [m]	Number of elements	Volume [m3]
			HTR hot side		
Inlet	Inlet pipes	0.7	20	12	
	Inlet Manifold 1			6	11.17885732
	Pipes out Inlet Manifold 1	0.336	0.2	54	0.957617759
	Plenum HX1 in			6	15.552
			HX1		
Inter	Plenum HX1 out			6	15.552
	Pipes in Outlet Manifold 1	0.336	0.2	54	
	Outlet Manifold 1			6	11.17885732
	Connecting pipes	0.7	5	12	
	Inlet Manifold 2			6	11.17885732
	Pipes out Inlet Manifold 2	0.336	0.2	54	
	Plenum HX2 in			6	15.552
			HX2		
Outlet	Plenum HX2 out			6	15.552
	Pipes in Outlet Manifold 2	0.264	0.2	54	
	Outlet Manifold 2			6	7.817287832
	Outlet Pipe	0.8	10	6	
			HTR cold side		
Inlet	Inlet pipes	0.45	80	12	
	Inlet Manifold 1			6	4.619833891
	Pipes out Inlet Manifold 1	0.216	0.2	54	
	Plenum HX1 in			6	15.552
			HX1		
Inter	Plenum HX1 out			6	15.552
	Pipes in Outlet Manifold 1	0.24	0.2	54	
	Outlet Manifold 1			6	5.703498631
	Connecting pipes	0.5	5	12	
	Inlet Manifold 2			6	5.703498631
	Pipes out Inlet Manifold 2	0.24	0.2	54	
	Plenum HX2 in			6	15.552
			HX2		
Outlet	Plenum HX2 out			6	15.552
	Pipes in Outlet Manifold 2	0.24	0.2	54	
	Outlet Manifold 2			6	5.703498631
	Outlet Pipe	0.5	40	12	
			PC hot side		
Inlet	Inlet pipes	0.8	10	6	
	Inlet Manifold 1			6	1.824395739
	Pipes out Inlet Manifold 1	0.328	0.2	36	0.608373187
	Plenum HX1 in			12	10.368
			HX		
Outlet	Plenum HX2 out			12	10.368
	Pipes in Outlet Manifold 2	0.2665	0.2	36	
	Outlet Manifold 2			6	1.20438625
	Outlet Pipe	0.65	1	6	

Set		Dh [m]	Length [m]	Number of elements	Volume [m3]
			HTS		
Inlet	Inlet pipes	0.5	40	12	
	Inlet Manifold 1			6	5.703498631
	Pipes out Inlet Manifold 1	0.24	0.2	54	0.488580489
	Plenum HX1 in			6	15.552
			HX1		
Inter 1	Plenum HX1 out			6	15.552
	Pipes in Outlet Manifold 1	0.24	0.2	54	
	Outlet Manifold 1			6	5.703498631
	Connecting pipes	0.5	5	12	
	Inlet Manifold 2			6	5.703498631
	Pipes out Inlet Manifold 2	0.24	0.2	54	
	Plenum HX2 in			6	15.552
			HX2		
Inter 2	Plenum HX2 out			6	15.552
	Pipes in Outlet Manifold 2	0.24	0.2	54	
	Outlet Manifold 3			6	5.703498631
	Connecting pipes	0.5	5	12	
	Inlet Manifold 4			6	5.703498631
	Pipes out Inlet Manifold 2	0.24	0.2	54	
	Plenum HX3 in			6	15.552
			HX3		
Outlet	Plenum HX3 out			6	15.552
	Pipes in Outlet Manifold 3	0.264	0.2	54	
	Outlet Manifold 5			6	6.901233343
	Outlet Pipe	0.55	20	12	

Appendix E: Loop thermodynamic values

In this last appendix are collected the thermodynamic values of all the points in the loop, as indicated in plant scheme, Figure 12. Table E. 1 contains the reference values, while Table E. 2 and Table E. 3 the static values of the Modelica cases, respectively the Ideal and Real.

Table E. 4 and Table E. 5 show the system behaviour after the activation of the control system, nominally the water and molten salt flow control.

The last two tables are filled with the cycle thermodynamic values after the two partial load operation strategies; Table E. 6 refers to the TIT strategy, while Table E. 7 to the valve strategy.

Table E. 1 Comillas cycle thermodynamic values

	T [ºC]	P [bar]	h [kJ/kg]	s [kJ/kg K]	ρ [kg/m3]	μ [m2/s]
1	490	300	953.0	2.55766	198.3	1.891E-07
2	343.8	85.8	801.0	2.57542	74.61	3.933E-07
3	79.62	85.4	494.7	1.9267	176.2	1.162E-07
4	35	85	308.8	1.35049	612.1	7.496E-08
5	76.62	300.8	343.6	1.36243	760.7	8.661E-08
6	262.2	300.4	659.4	2.09956	315.6	1.075E-07
s1	284.7	1.6	168.1		1871	1.77E-06
s2	495	1	496.1		1717	7.14E-07

Table E. 2 Modelica ideal case static thermodynamic results

	T [ºC]	P [bar]	h [kJ/kg]	s [kJ/kg K]	ρ [kg/m3]	μ [m2/s]
1	488.0	309.0	949.8	2.5476	204.4	1.841E-07
2	338.4	85.6	795.4	2.5669	75.1	3.879E-07
3	86.7	85.6	496.5	1.9316	167.5	1.227E-07
4	35.2	85.1	310.5	1.3559	605.4	7.467E-08
5	84.6	309.6	358.8	1.4020	735.8	8.510E-08
6	262.1	309.5	657.7	2.0910	324.5	1.059E-07
Salt in	495	1.6	1123.1		1775.2	
Salt out	276.2	1.0	810.0		1914.3	
Water in	25	8.0	105.6		997.3	
Water out	35.4	7.0	148.9		994.1	

Table E. 3 Modelica real case static thermodynamic results

	T [ºC]	P [bar]	h [kJ/kg]	s [kJ/kg K]	ρ [kg/m3]	μ [m2/s]
1	489.7	310.3	951.8	2.5495	204.67	1.842E-07
2	341.8	87.5	799.0	2.5685	76.39	3.835E-07
3	86.4	85.8	495.8	1.9292	168.50	1.221E-07

4	35.6	85.0	314.8	1.3700	586.98	7.392E-08
5	84.2	314.2	357.4	1.3964	741.88	8.553E-08
6	264.6	313.1	660.6	2.0943	325.60	1.060E-07
Salt in	495	1.6	1123.1		1775.2	
Salt out	271.1	1.0	786.0		1917.2	
Water in	25	8.0	105.6		997.3	
Water out	35.6	7.0	149.6		994.1	

Table E. 4 Thermodynamic cycle values after the water PI activation

	T [ºC]	**P [bar]**	**h [kJ/kg]**	**s [kJ/kg K]**	**ρ [kg/m3]**	**μ [m2/s]**
1	491.6	302.1	954.9	2.5588	199.1	1.887E-07
2	346.4	87.4	804.2	2.5773	75.6	3.895E-07
3	81.1	85.7	487.8	1.9069	175.0	1.172E-07
4	35.0	85.0	308.8	1.3505	612.1	7.496E-08
5	78.8	306.1	347.4	1.3714	756.5	8.638E-08
6	266.0	304.8	663.8	2.1051	316.4	1.078E-07

Table E. 5 Thermodynamic cycle values after the molten salt PI activation

	T [ºC]	**P [bar]**	**h [kJ/kg]**	**s [kJ/kg K]**	**ρ [kg/m3]**	**μ [m2/s]**
1	490.0	302.2	952.8	2.5560	199.6	1.880E-07
2	344.9	87.4	802.6	2.5745	75.9	3.876E-07
3	81.1	85.7	487.8	1.9069	175.0	1.172E-07
4	35.0	85.0	308.8	1.3505	612.1	7.495E-08
5	78.8	306.2	347.4	1.3714	756.5	8.638E-08
6	264.8	304.9	662.2	2.1021	317.6	1.074E-07

Table E. 6 Thermodynamic cycle values with the TIT part-load operation

	T [ºC]	**P [bar]**	**h [kJ/kg]**	**s [kJ/kg K]**	**ρ [kg/m3]**	**μ [m2/s]**
1	397.5	302.1	835.8	2.3926	232.6	1.525E-07
2	262.1	87.2	708.0	2.4108	89.7	2.943E-07
3	80.6	85.7	487.0	1.9046	175.7	1.167E-07
4	35.0	85.0	308.8	1.3505	612.1	7.495E-08
5	78.8	305.5	347.3	1.3714	756.2	8.635E-08
6	199.4	304.2	568.3	1.9162	395.5	9.041E-08

Table E. 7 Thermodynamic cycle values after the valve part-load operation

	T [ºC]	**P [bar]**	**h [kJ/kg]**	**s [kJ/kg K]**	**ρ [kg/m3]**	**μ [m2/s]**
1	490.0	272.4	955.0	2.5794	181.3	2.038E-07
2	356.1	87.0	815.5	2.5961	74.0	4.028E-07
3	79.6	85.6	485.5	1.9005	176.7	1.159E-07
4	35.0	85.0	308.8	1.3505	612.1	7.495E-08
5	81.0	326.7	349.5	1.3696	766.1	8.726E-08
6	273.7	274.9	679.5	2.1525	280.8	1.166E-07

References

Alberto de la Calle, Jim Hinkley, Paul Scott, John Pye, 2018. SolarTherm: A New Modelica Library and Simulation Platform for Concentrating Solar Thermal Power Systems.

Al-Sulaiman, F.A., Atif, M., 2015. Performance comparison of different supercritical carbon dioxide Brayton cycles integrated with a solar power tower. Energy 82, 61–71. https://doi.org/10.1016/j.energy.2014.12.070

Andrea Baronci, Giuseppe Messina, Stephen J. McPhail, Angelo Moreno, 2015. Numerical investigation of a MCFC (Molten Carbonate Fuel Cell) system hybridized with a supercritical CO2 Brayton cycle and compared with a bottoming Organic Rankine Cycle. Elsevier, Energy 1063–1073.

Angelino, G., 1968. Carbon dioxide condensation cycles for power production. Journal of Engineering for Power-T. ASME 287–295. https://doi.org/10.1115/1.3609190

Ariu, V., 2014. Heat exchanger analysis for innovative molten salt fast reactor. ETH, Zurich.

ASME B31.1, 2007. Code for Pressure Piping, Power Piping.

AZoM, 2004. Stainless Steel Grade 316L Properties, Fabrication and Applications (UNS S31603).

Bahamonde Noriega, J.S., 2012. Design method for s-CO2 gas turbine power plants: Integration of thermodynamic analysis and components design for advanced applications. Delft University of Technology, The Netherlands.

Balje, O.E., 1981. Turbomachines: a guide to design selection and theory. Wiley, New York.

Benjamín Monge Brenes, 2014. Design of supercritical carbon dioxide centrifugal compressors. Grupo de maquinas y motores termico de Sevilla, Sevilla.

BP Statistical Review of World Energy, 2019. BP Statistical Review of World Energy.

California Energy Commission, 2015. System integration of containerized molten salt thermal energy storage in novel cascade layout.

Carstens, N.A., 2004. Control Strategies for Supercritical Carbon Dioxide Power Conversion Systems. MIT.

Casella, F., 2011. Introduction to the Dynamic Modelling of Thermo-Fluid Systems using Modelica.

Casella, F., Colonna, P., 2011. Development of a Modelica dynamic model of solar supercritical CO2 Brayton cycle power plants for control studies. Presented at the Supercritical CO2 Power Cycle Symposium, Boulder Colorado.

Casella, F., Richter, C., 2010. ExternalMedia: A Library for Easy Re-Use of External Fluid Property Code in Modelica ExternalMedia: A Library for Easy Re-Use of External Fluid Property Code in Modelica. Proc. 6th Int. Model. Conf.

Çengel, Y.A., Cimbala, J.M., 2006. Fluid mechanics: fundamentals and applications, McGraw-Hill series in mechanical engineering. McGraw-HillHigher Education, Boston.

Chai, L., Tassou, S.A., 2019. Numerical study of the thermohydraulic performance of printed circuit heat exchangers for supercritical CO2 Brayton cycle applications. Energy Procedia 161, 480–488. https://doi.org/10.1016/j.egypro.2019.02.066

Chu, W., Li, X., Ma, T., Chen, Y., Wang, Q., 2017. Experimental investigation on SCO2-water heat transfer characteristics in a printed circuit heat exchanger with straight channels. Int. J. Heat Mass Transf. 113, 184–194. https://doi.org/10.1016/j.ijheatmasstransfer.2017.05.059

Ehsanul Kabir, Pawan Kumar, Sandeep Kumar, Adedeji A. Adelodun, Ki-Hyun Kim, 2018. Solar energy: Potential and future prospects.

Elmqvist, H., 2014. Modelica Evolution - From My Perspective. Presented at the the 10th International Modelica Conference, March 10-12, 2014, Lund, Sweden, pp. 17–26. https://doi.org/10.3384/ecp1409617

Energy Technology Perspectives 2017,. . Organisation for Economic Co-operation and Development., S.l.
EUROfusion, 2019. EUROfusion [WWW Document]. Euro-Fusionorg. URL https://www.euro-fusion.org/index.php?id=1&L=930
European Commission, 2015. Paris Agreement [WWW Document]. Off. Website Eur. Union. URL https://ec.europa.eu/clima/policies/international/negotiations/paris_en
Fuller, R., Preuss, J., Noall, J., 2012. Turbomachinery for Supercritical CO2 Power Cycles, in: Volume 5: Manufacturing Materials and Metallurgy; Marine; Microturbines and Small Turbomachinery; Supercritical CO2 Power Cycles. Presented at the ASME Turbo Expo 2012: Turbine Technical Conference and Exposition, American Society of Mechanical Engineers, Copenhagen, Denmark, pp. 961–966. https://doi.org/10.1115/GT2012-68735
Fundamentals and applications of supercritical carbon dioxide (sco2) based power cycles, 1st edition. ed, 2017. . Elsevier, Waltham, MA.
Gnielinski, V., 1976. New Equations for Heat and Mass Transfer in Turbulent Pipe and Channel Flow. International Chemical Engineering 16.
Gonzalez Gonzalez, J., 2018. Modelling Axial Turbomachinery for Compressed Air Energy Storage. University of Waterloo, Ontario, Canada.
Hakkarainen, E., Sihvonen, T., Lappalainen, J., 2016. Dynamic modelling and simulation of CSP plant based on sCO2 closed Brayton cycle. https://doi.org/10.13140/RG.2.2.14006.70729
Halimi, B., Suh, K.Y., 2012. Computational analysis of supercritical CO2 Brayton cycle power conversion system for fusion reactor. Energy Convers. Manag. 63, 38–43. https://doi.org/10.1016/j.enconman.2012.01.028
IAEA, 2019. IAEA, Nuclear power and climate change. [WWW Document]. IAEA. URL https://www.iaea.org/topics/nuclear-power-and-climate-change
IAEA, 2018. CLIMATE CHANGE AND NUCLEAR POWER 2018. Wien.
Incropera, F.P., DeWitt, D.P., 2002. Fundamentals of heat and mass transfer, 5th ed. ed. J. Wiley, New York.
IRENA, 2019. Renewable power generation costs in 2018.
ITER, 2019. ADVANTAGES OF FUSION [WWW Document]. ITER.org. URL https://www.iter.org/sci/Fusion
Iverson, B.D., Conboy, T.M., Pasch, J.J., Kruizenga, A.M., 2013. Supercritical CO2 Brayton cycles for solar-thermal energy. Appl. Energy 111, 957–970. https://doi.org/10.1016/j.apenergy.2013.06.020
Linares, J.I., Arenas, E., Cantizano, A., Porras, J., Moratilla, B.Y., Carmona, M., Batet, L., 2018. Sizing of a recuperative supercritical CO2 Brayton cycle as power conversion system for DEMO fusion reactor based on Dual Coolant Lithium Lead blanket. Fusion Eng. Des. 134, 79–91. https://doi.org/10.1016/j.fusengdes.2018.06.026
Liu, Y., Wang, Y., Huang, D., 2019. Supercritical CO2 Brayton cycle: A state-of-the-art review. Energy 189, 115900. https://doi.org/10.1016/j.energy.2019.115900
Luu, M.T., Milani, D., McNaughton, R., Abbas, A., 2017. Dynamic modelling and start-up operation of a solar-assisted recompression supercritical CO 2 Brayton power cycle. Appl. Energy 199, 247–263. https://doi.org/10.1016/j.apenergy.2017.04.073
Ma, Z., Turchi, C.S., 2011. Advanced supercritical carbon dioxide power cycle configurations for use in concentrating solar power systems. Presented at the Supercritical CO2 Power Cycle Symposium Boulder, NREL, Colorado.
Modelica Association, 2017. Documents [WWW Document]. Model. Lang. Doc.
Neises, T., Turchi, C., 2014. Supercritical CO2 Power Cycles: Design Considerations for Concentrating Solar Power. Presented at the 4th International Symposium - Supercritical CO2 Power Cycles, EERE, Pittsburgh, Pennsylvania.

Osorio, J.D., Hovsapian, R., Ordonez, J.C., 2016. Dynamic analysis of concentrated solar supercritical CO2-based power generation closed-loop cycle. Appl. Therm. Eng. 93, 920–934. https://doi.org/10.1016/j.applthermaleng.2015.10.039

Reyes-Belmonte, M.A., Sebastián, A., Romero, M., González-Aguilar, J., 2016. Optimization of a recompression supercritical carbon dioxide cycle for an innovative central receiver solar power plant. Energy 112, 17–27. https://doi.org/10.1016/j.energy.2016.06.013

Singh, R., Kearney, M.P., Manzie, C., 2013a. Extremum-seeking control of a supercritical carbon-dioxide closed Brayton cycle in a direct-heated solar thermal power plant. Energy 60, 380–387. https://doi.org/10.1016/j.energy.2013.08.001

Singh, R., Miller, S.A., Rowlands, A.S., Jacobs, P.A., 2013b. Dynamic characteristics of a direct-heated supercritical carbon-dioxide Brayton cycle in a solar thermal power plant. Energy 50, 194–204. https://doi.org/10.1016/j.energy.2012.11.029

SNL, 2015. Supercritical CO2-Brayton Cycle [WWW Document]. Sandia Natl. Lab. Energy. URL https://energy.sandia.gov/programs/renewable-energy/supercritical-co2/

Southall, D., Dewson, S.J., 2010. Innovative Compact Heat Exchangers, in: ICAPP ‘10. San Diego, California.

Standards Norway, 2006. NORSOK STANDARD P-001. Process Design.

Steven, A., Wright, P., Pickard, P., Vernon, M.E., 2008. Initial status and test results from a supercritical CO2 Brayton cycle test loop. Presented at the International Congress on Advances in Nuclear Power Plants (ICAPP ’08), Anaheim, California.

Stocker, T.F., Qin Dahe, Gian-Kasper Plattner, 2013. Technical Summary.

TheWorldBank, 2019. Renewables share [WWW Document]. World Bank. URL https://data.worldbank.org/

Tiller, M., Company, F., Dearborn, U., Tummescheit, H., Hartford, U., Casella, F., Leva, A., December 3, 2. Modelica open library for power plant simulation: Design and experimental validation. Proc 3rd Model. Conf.

Ty Neises, NREL, 2013. A comparison of supercritical carbon dioxide power cycle configurations with an emphasis on CSP applications.

U.S. Energy Information Administration, 2019. International Energy Outlook 2019.

V. Dostal, M.J. Driscoll, P. Hejzlar, 2004. A Supercritical Carbon Dioxide Cycle for Next Generation Nuclear Reactors. MIT.

WorldNuclear, 2019. Nuclear Fusion Power [WWW Document]. World-Nucl. URL https://www.world-nuclear.org/information-library/current-and-future-generation/nuclear-fusion-power.aspx

Wu, P., Gao, C., Huang, Y., Zhang, D., Shan, J., 2020. Supercritical CO2 Brayton Cycle Design for Small Modular Reactor with a Thermodynamic Analysis Solver. Sci. Technol. Nucl. Install. 2020, 1–16. https://doi.org/10.1155/2020/5945718

Wu, P., Gao, C., Shan, J., 2018. Development and Verification of a Transient Analysis Tool for Reactor System Using Supercritical CO2 Brayton Cycle as Power Conversion System. Sci. Technol. Nucl. Install. 2018, 1–14. https://doi.org/10.1155/2018/6801736

Yang, Y., Guo, Q., Lin, J., Zhang, Y., Ye, K., Bian, B., Li, Z., 2017. Modeling and Simulating Supercritical CO2 Brayton Cycle in SMR Using Modelica, in: Volume 3: Nuclear Fuel and Material, Reactor Physics and Transport Theory; Innovative Nuclear Power Plant Design and New Technology Application. Presented at the 2017 25th International Conference on Nuclear Engineering, American Society of Mechanical Engineers, Shanghai, China, p. V003T13A009. https://doi.org/10.1115/ICONE25-66649